Nitride nanostructures for spintronic applications

Zur Erlangung des akademischen Grades eines
DOKTORS DER NATURWISSENSCHAFTEN
von der Fakultät für Physik des Karlsruher Instituts für Technologie

genehmigte

DISSERTATION

von

Dipl. Phys. Ralf Schuber
aus Lörrach

Tag der mündlichen Prüfung:	1. Juli, 2011
Referent:	Prof. Dr. H. Kalt
Korreferent:	Prof. Dr. Th. Schimmel

Parts of this work have already been published or accepted for publishing:

R. Schuber, M. M. C. Chou, P. Vincze, Th. Schimmel, D. M. Schaadt, "Growth of *A*-plane GaN growth on (010) $LiGaO_2$ by plasma-assisted molecular beam epitaxy", *Journal of Crystal Growth* **312** (2010) 1665-1669.

R. Schuber, M. M. C. Chou, D. M. Schaadt, "Growth of *M*-plane GaN on (100) $LiGaO_2$ by plasma-assisted molecular beam epitaxy", *Thin Solid Films* **518** (2010) 6773-6776.

R. Schuber, Y. L. Chen, C. H. Shih, T. H. Huang, P. Vincze, I. Lo, L. W. Chang, Th. Schimmel, M. M. C. Chou, D. M. Schaadt, "Growth of non-polar GaN on $LiGaO_2$ by plasma-assisted MBE", *Journal of Crystal Growth* **323** (2010) 76-79.

R. Schuber, M. M. C. Chou, P. Vincze, Th. Schimmel, D. M. Schaadt, "Growth of *M*- and *A*-plane GaN on $LiGaO_2$ by plasma-assisted MBE", accepted in *AIP Conference Proceedings* (2010).

C. H. Shih, T. H. Huang, R. Schuber, Y. L. Chen, L. W. Chang, I. Lo, M. M. C. Chou, D. M. Schaadt, "Microstructure of *M*- and *A*-plane GaN on $LiGaO_2$ grown by plasma-assisted MBE", *Nanoscale Research Letters* **6** (2011) 425.

R. Schuber, P. R. Ganz, F. Wilhelm, A. Rogalev, D. M. Schaadt, "Local electronic structure of Cu-doped GaN investigated by XANES and XLD", *Physical Review B* **84** (2011) 155206.

In addition, results were presented at the spring meetings of the Deutsche Physikalische Gesellschaft (DPG) and the following international conferences:

16th International Conference on Molecular Beam Epitaxy, Berlin, Germany 2010.

30th International Conference on the Physics of Semiconductors, Seoul, Korea 2010.

International Conference on Superlatttices, Nanostructures and Nanodevices, Peking, China 2010.

Euro MBE, L'alp d'Huez, France 2011.

List of Abbreviations

2DEG	two-**d**imensional **e**lectron **g**as
AES	**A**uger **e**lectron **s**pectroscopy
AHE	**a**nomalous **H**all **e**ffect
AFM	**a**tomic **f**orce **m**icroscopy
BEP	**b**eam **e**quivalent **p**ressure
BMP	**b**ound **m**agnetic **p**olaron
CTE	**c**oefficient of **t**hermal **e**xpansion
DMS	**d**ilute **m**agnetic **s**emiconductors
ELOG	**e**pitaxial **l**ayer **o**ver **g**rowth
EXAFS	**e**xtended **x**-ray **a**bsorption **f**ine **s**tructure
FET	**f**ield-**e**ffect **t**ransistor
FIB	**f**ocused **i**on **b**eam
FWHM	**f**ull **w**idth at **h**alf **m**aximum
HEMT	**h**igh **e**lectron **m**obility **t**ransistor
HVPE	**h**ydride **v**apor **p**hase **e**pitaxy
LAO	**L**i**A**l$\mathbf{O}_2$
LD	**l**aser **d**iode
LED	**l**ight **e**mitting **d**iode
LGO	**L**i**G**a$\mathbf{O}_2$
MBE	**m**olecular **b**eam **e**pitaxy
MCD	**m**agnetic **c**ircular **d**ichroism
MOCVD	**m**etal**o**rganic **c**hemical **v**apor **d**eposition
MOVPE	**m**etal**o**rganic **v**apor **p**hase **e**pitaxy
MQW	**m**ultiple **q**uantum **w**ell
PAMBE	**p**lasma **a**ssisted **m**olecular **b**eam **e**pitaxy
PID	**p**roportional **i**ntegral **d**erivative
QCSE	**Q**uantum **C**onfined **S**tark **E**ffect
QD	**q**uantum **d**ot
QW	**q**uantum **w**ell
RBS	**R**utherford **b**ack **s**cattering
RHEED	**r**eflection **h**igh **e**nergy **e**lectron **d**iffraction
RMBE	**r**eactive **m**olecular **b**eam **e**pitaxy
rms	**r**oot **m**ean **s**quare

SEM	**s**canning **e**lectron **m**icroscopy
SIMS	**s**econdary **i**on **m**ass **s**pectroscopy
SQUID	**s**uperconducting **q**uantum **i**nterference **d**evice
TCE	**T**ri**c**hloro**e**thylene
T_C	Curie temperature
TEM	**t**ransmission **e**lectron **m**icroscopy
TM	**t**ransition **m**etal
VSM	**v**ibrating **s**ample **m**agnetometer
XANES	**x**-ray **a**bsorption **n**ear **e**dge **s**tructure
XLD	**x**-ray **l**inear **d**ichroism
XRD	**x**-ray **d**iffraction
XMCD	**x**-ray **m**agnetic **c**ircular **d**ichroism

Contents

1 Introduction

The field of spintronics, i.e. the application of the electron's spin in addition to its charge for future superior device functionality, is nowadays of great interest both for research and commercial purposes [1]. Spintronics in metals is already widely used in computer storage devices [2]; recently the notion of bringing spintronics to devices based on semiconductor technology has triggered extensive investigations on a material class called dilute magnetic semiconductors (DMS). DMS are semiconductors doped with elements that change the host semiconductor material to exhibit magnetic properties. The prospect of being able to handle the charge carriers' spin for information transport has led to a large number of new device designs like the spin field-effect transistor (FET) and the spin light emitting diode (LED) [3, 4], promising to reveal new applications or an improvement of existing electrical devices.

Before the benefits of new spintronics applications can be exploited a number of issues have to be solved, like finding an appropriate material for efficient room temperature spin-injection and an appropriate semiconductor material with properties promising the desired device functionality. In order to contribute to the understanding and fabrication of efficient spintronic-related materials, this thesis aims to tackle two points. Firstly, the material system of group III-nitrides, especially gallium nitride (GaN) is investigated for being an adequate material system for the "active" region of a device. Secondly, the understanding of a prospective spin-aligner candidate is improved by answering the question where Cu is incorporated in Cu-doped GaN, a room temperature DMS.

GaN has become one of the most important semiconductors of our age [5]. Because of its magnificent optical and electrical properties it is now used in applications such as lighting (projectors, TVs, automobiles, displays, traffic lights and general lighting) [6, 7], lasers (game consoles and Blue-Ray players) [7], detectors [8, 9], and high power as well as high frequency power electronics [7]. Fig. 1.1 depicts a company's website advertising the multitude of applications of GaN in their business. The enormous applicability and the favorable properties of GaN could greatly support the success of spintronics devices, if these were based on GaN.

GaN is a direct band gap material with a band gap of about 3.5 eV. This corresponds to a wavelength near 355 nm which is on the violet side of visible light. One

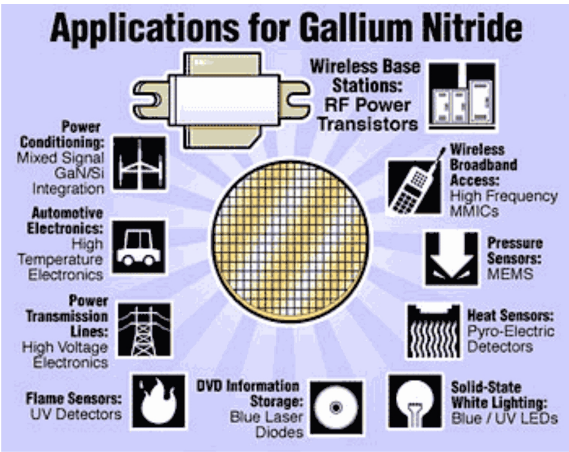

Figure 1.1: Examples of applications of GaN as a commercial product. The graphic is taken from the website of the Nitronex Corporation [10].

of the probably most quoted preferences of the nitride material system is the band gap range exhibited by AlN, GaN and InN, namely from the UV (6.2 eV for AlN) to the IR (0.7 eV for InN). This leads to the possibility of fabricating band gaps in the complete visible range by forming ternary or quaternary alloys of Al, Ga, In and N. Not only the optical properties are promising; the material also exhibits very high electron mobility which is essential for high-power, high-frequency electronic applications, like e.g. in high electron mobility transistors (HEMT) [11]. High electron mobility at room temperature is usually around 1500 cm^2/Vs in $Al_{0.25}Ga_{0.75}N/GaN$ heterostructures and have been shown to reach 75000 cm^2/Vs at 4.2 K with a sheet electron density of 1.53×10^{12} cm^{-2} for a two-dimensional electron gas (2DEG) in $Al_{0.05}Ga_{0.95}N/GaN$ [12]. Furthermore, the high chemical, thermal and mechanical stability of GaN is of benefit to many applications, making the material more worthwhile for investigation.

GaN is also a material which exhibits a polar axis along the [0001] c-direction. Due to the hexagonal crystal symmetry and a natural diversion of GaN from the perfect wurtzite structure, GaN shows spontaneous and piezoelectric polarization along this polar axis. This fact leads to the presence of polarization charges at interfaces and is especially critical when multi layered heterostructures are fabricated in c-direction. The polarization charges cause electric fields inside the structures leading to a distortion of the electronic band structure and the so called quantum confined Stark effect (QCSE) in structures of low dimensionality. The main consequences are a reduction of the oscillator strength due to a spatial separation of electrons and holes as well as a decrease in the energy of the radiative transition.

One approach to avoid the unwanted consequences of the QCSE is the growth of epitaxial layers with non-polar surfaces, such as the *M*- and *A*-planes, where the internal electric fields run perpendicular instead of parallel to the crystal growth direction. It has been experimentally demonstrated that in such a case GaN light emitting devices show higher efficiency [13] making growth on these crystal planes highly attractive.

Because non-polar GaN substrates for homoepitaxy are only available in very limited sizes and extremely expensive, alternative substrates for heteroepitaxy of non-polar GaN are needed. In the context of this thesis, a new plasma assisted molecular beam epitaxy (PAMBE) system especially aimed at the growth of nitride semiconductors was set up and brought to operation for growth of GaN. Using this machine, growth of non-polar GaN was investigated on two different substrates, namely $LiAlO_2$ and $LiGaO_2$. The growth parameters were optimized towards a flat surface morphology and high crystal quality of the resulting *M*- and *A*-plane GaN films.

For applications using the spin of charge carriers, their spins need to be correctly oriented and injected into the "active" material in an efficient way, i.e. without loss of the spin orientation. Therefore, an adequate spin-aligner has to be found. For spin injection into a semiconductor the most straight forward approach would be to use a DMS [14, 15]. One important desired property of a DMS for feasible spintronic device operation is ferromagnetism at room temperature. Many different DMS materials have been investigated in the past years; GaN, however, gained special attention due to the predicted possible room temperature ferromagnetism, when doped with magnetic elements [16]. Although Cu is a non-magnetic element, Wu et al. [17] theoretically predicted ferromagnetism above room temperature in Cu-doped GaN, which was later confirmed experimentally in a number of reports on Cu-doped GaN, e.g. [18–20].

The exact mechanism governing ferromagnetic behavior in Cu-doped GaN and DMS in general is still unclear. Clarification of the many, partly seemingly contradicting experimental results, is necessary for understanding the situation in this new class of materials. One very basic question to be answered in this context is the location of Cu in the GaN material, i.e. how and where Cu atoms are incorporated in the GaN crystal. This issue is addressed in this work with the help of x-ray absorption experiments, which were performed at the European Synchrotron Radiation Facility (ESRF). The results of the analysis of the experimental data are compared to calculations performed for Cu-doped GaN using a commercial software package (FDMNES [21]).

The outline of this thesis is as follows. The relevant parts of the field of spintronics to this work are discussed in chapter 2. Herein an introduction to the basic ideas of spintronics, the current status of DMS research and the role of the most important GaN DMS, including Cu-doped GaN are presented. The subsequent third chapter

gives an overview of important properties and peculiarities of the material of central interest, namely GaN. This includes a description of its crystal structure, the important role of internal electric fields and how they can be avoided in GaN. Details on how GaN can be fabricated in the laboratory and a description of the machine used for producing GaN samples in this work is provided in the concluding section 3.3.2.

Growth of non-polar GaN by PAMBE on (100) γ-$LiAlO_2$, (100) β-$LiGaO_2$ and (010) β-$LiGaO_2$ is described in chapter 4 accompanied by an analysis of the produced GaN films. Chapter 5 presents the experimental and theoretical investigations and results of identifying the placement of Cu in GaN during PAMBE growth of Cu-doped GaN.

2 A short introduction to spintronics

The aim of this chapter is to give the reader a brief introduction to the subject of spintronics and to build a bridge of this field to the use of group III-nitrides as a convenient and adequate material system for the basis of spintronic devices. In section 2.1 the very basic principles of spintronics are introduced and the field is narrowed down to spintronics in semiconductors and the important category of dilute magnetic semiconductors (DMS). The subsequent section 2.2 will outline the current status of work that has been done in this field. Concluding this chapter the specific advances and the role of nitrides in spintronics and specifically the introduction of Cu as a non-magnetic impurity making GaN ferromagnetic will be discussed in section 2.3.

2.1 The basic idea of spintronics

Spintronics is a term basically put together out of two parts: spin and electronics. Its meaning lies exactly in this connection, namely that not only the charge but also the spin of electrical charge carriers is used in transporting information. A great achievement in the field of spintronics was the discovery of the giant magnetoresistance (GMR) in magnetic layers of metals [2, 22]. The GMR effect nowadays used in everyday life (e.g. data storage in computer hard discs) was considered of such importance, that the Nobel Prize was awarded for its discovery in 2007. In this work, however, the usage of a different class of materials in spintronics shall be focused on: the class of semiconductors.

The discovery and research on semiconductors have made possible a huge number of devices and have revolutionized our technological world[1]. Especially the optical properties combined with the electric behavior of such materials are of great interest and have been applied in light emitting diodes, solar cells, laser diodes, quantum

[1]Interestingly, in the beginnings of semiconductor research the enormous impact of this field could not at all be anticipated. In this context, a famous statement of Wolfgang Pauli in a letter to his assistant at the time, Rudolf Peierls, in 1931 is cited, where he writes: "Über Halbleiter sollte man nicht arbeiten, das ist eine Schweinerei, wer weiss, ob es überhaupt Halbleiter gibt." which loosely translated means: "One should not work on semiconductors, that is a mess, who knows whether there are semiconductors at all." [23]

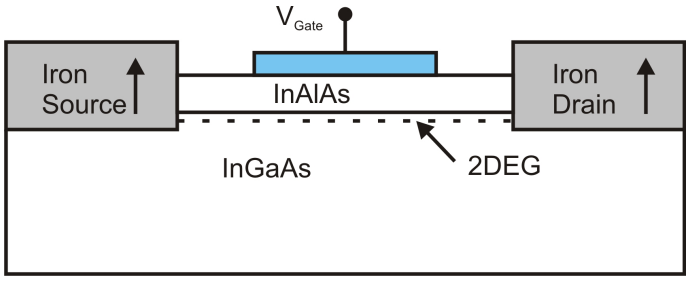

Figure 2.1: Schematic original design of a spin FET from [25]. In a DMS based spin FET the iron electrodes are replaced by a magnetic semiconductor, polarizing the electrons which are injected into the channel. The spin character of the charge carriers in the channel can be altered by a gate voltage to turn the current on or off.

cascade lasers, phototransistors, photomultipliers, charge-coupled imaging devices and optical fiber communication. The advantages of spin transport additionally to or instead of charge transport promises the improvement of existing devices for faster information processing at less power consumption [3], but also leads to new device concepts like spin FETs, spin LEDs, spin tunneling junctions and many more [3, 4, 24].

It was a novel design for a spin transistor using the spin of the carriers to modulate the electric current, proposed by Datta and Das [25] in 1990, that kicked off a new motivation for the search of adequate materials with properties suitable for semiconductor spintronic applications. The idea of Datta and Das described that spin polarized electrons, from a spin aligning source electrode, could be injected into a semiconductor channel and read out by a magnetically polarized drain electrode. Fig. 2.1 shows a schematic design of a spin FET. While the current is maximal when the magnetic moments of electrons and drain are aligned, the current is changed by influencing the electron spin in the channel by applying a gate voltage. The interaction of the electric field from the gate on the electrons' spins in the channel happens via the Rashba spin-orbit coupling [25, 26]. The resulting misalignment of the charge carriers' spin with respect to the magnetic orientation of the drain results in a shutdown of the current. The bias needed for a shutdown is predicted to be much lower than that required for a conventional charge controlled FET.

Now, the question to be answered for accomplishing spintronics in semiconductors, is: Which are the requirements for a material for such functional devices? In the case of a spin FET, the spin of the electrons must be aligned (need for room temperature ferromagnetic material with high spin polarization of the carriers), then efficiently injected into a material (low resistance at the interface), transported with the ability to control the spin (the spin must be carried by charge carriers with long coherence

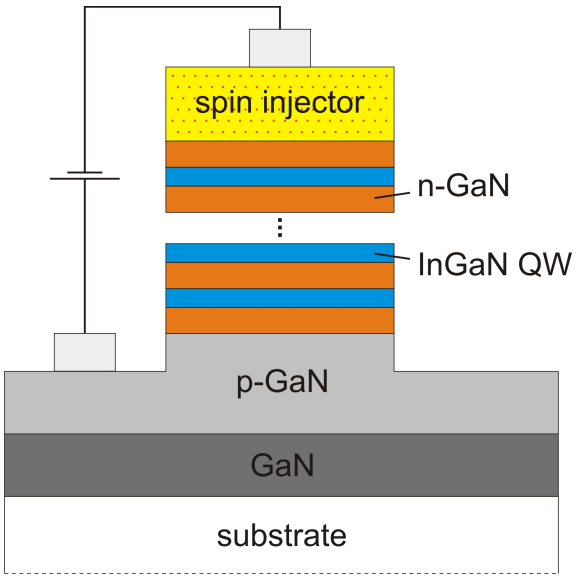

Figure 2.2: Schematic of a spin LED based on GaN. Efficient spin injection can be obtained by choosing a GaN based DMS for spin injector e.g. Cu-doped GaN.

time) and finally the spin as well as the current must be detected. The first steps, i.e. the spin alignment and injection into a semiconductor material, are necessary for many devices. In the case of a spin LED the last step of spin and current detection is replaced by the radiative recombination of electron hole pairs, yielding polarized photons. Efficient ways of providing for this are the use of heterostructures of semiconductors such as multiple quantum wells (MQW) or quantum dots (QD) (see Fig. 2.2). This work aims to tackle the question of an efficient spin-aligner and an appropriate material for spin carriage and radiative transition for the basis of devices like spin LEDs.

For the injection of spin-polarized carriers into a semiconductor a ferromagnetic metal could be used. The success of such a system was however suppressed, two of the reasons being the mismatch in conductivities between the magnet and the semiconductor and the relatively low electron spin polarization of the metallic ferromagnet [27]. Calculations have shown, that only about 0.1% of the current in a 2D electron gas contacted by two ferromagnetic metals are spin-polarized, while ferromagnetic semiconductors would overcome the problem of loss of spin-polarization due to the giant Zeeman splitting which would force the current carrying electrons to align their spins to the lower Zeeman level [15]. Hence, the approach of using magnetic semiconductors, promising greater success and being more practical, yielding a higher efficiency and lower resistance barrier, i.e. better conductivity, better Fermi

level matching and better production possibilities for cleaner surfaces is discussed in literature. Here, the diluted magnetic semiconductors (DMS) have received the most interest because of their easy implementation in the existing semiconductor technology and the prospect of using one basis material system for the whole device, where electronic transitions from one material component to the next would preserve their spin-polarization to a large extent.

Dilute magnetic semiconductors, initially called semimagnetic semiconductors [28], are semiconducting materials that are diluted with magnetic ions of transition metals (Sc, Ti, V, Cr, Mn, Fe, Co, Ni; the case of Cu is discussed in more detail in section 2.3) or rare earths (e.g. Eu, Gd, Er) substituting cations of the host material thus rendering the complete semiconductor ferromagnetic. Among different desirable properties for these materials one of the main points for prospective device application in the absence of an external magnetic field is the necessity for a high Curie temperature (T_C) in ferromagnetic DMS, namely at room temperature or above.

Spin injection from a DMS into a non-magnetic semiconductor has already been shown in a few material systems and is investigated extensively. A zero-magnetic field electrical spin injection in an all-GaAs based spin LED, using ferromagnetic GaMnAs as spin-aligner, has been reported by Ohno et al. [29], injecting spin polarized holes into the ferromagnetic structure. An early report on $Be_xMn_yZn_{1-x-y}Se$ as a spin-aligner to inject spin-polarized electrons into a GaAs/AlGaAs MQW LED structure has shown an injection efficiency of 90% [30]. ZnMnSe is known to exist in paramagnetic, spin glass or antiferromagnetic phases, depending on the Mn concentration and the temperature [31, 32] and spin injection experiments therefore need the presence of a high external magnetic field and low temperature. It has been reported that the electron conductivity is important for spin polarization in n-type ZnMnSe [33], which is why Cl doping to control the electron density is used frequently in ZnMnSe. The benefits of the ZnMnSe system, however, have been demonstrated by an almost perfect spin injection initialization into several different InAs/GaAs quantum dots (QD) simultaneously [34]. For QD ensembles, up to about 60% spin polarization has been achieved in InGaAs QDs [35] where $Zn_{0.95}Mn_{0.05}S_{0.1}Se_{0.9}$:Cl[2] was used as a spin-aligner; InGaAs QDs excited by short electrical pulses in the nanosecond range through the DMS $Zn_{0.95}Mn_{0.05}$Se:Cl show a spin-polarization degree of up to 41% [36]. Also, spin-injection through $Zn_{0.80}Mn_{0.20}$Se into CdS QDs has been reported by optical means which shows an injected spin polarization of 32% [37].

Although investigations on DMS already go back some 30 years, the interest in this field continues to persist and is enormous. To underline this statement the numbers

[2]The admixture of Sulfur intends to improve the matching of the lattice constants between ZnMnSe and GaAs for better epitaxial growth.

of citations on important papers is huge. Until today[3] for example, the Datta & Das paper [25] on the spin FET has been cited 2065 times (193 times in the year 2010); the paper of Dietl et al. [16] about the mean field Zener model for magnetic semiconductors (discussed below) was referenced 3678 times (438 times in 2010) and a short review by Ohno [38] on this topic 2492 times (213 times in 2010).

2.2 Current status on dilute magnetic semiconductors (DMS)

While in theory the question of the usefulness of magnetic semiconductors seems undoubtedly clear, the experimental realization of devices lags behind. This is considered to be a reason of finding the right material that can be altered in such a way, that the desired properties appear. Above all, overcoming the low Curie temperature of most material systems was considered a challenge. Besides experimental efforts to finding the best DMS which will be briefly summarized first in this section, an outline of theoretical models applied to predict the properties of appropriate materials, resulting in the persistent notion to improve our knowledge of the physics involved and pushing forward in the direction of spintronic devices, will follow.

Already in the late 1970's the idea of making a semiconductor magnetic engaged scientists in exchanging part of the metal atoms in a compound semiconductor with magnetic atoms. Big interest in these structures started to rise, when an anomalously large spin splitting was observed in magnetotransmission experiments on $Hg_{1-x}Mn_xTe$ [39], which was interpreted to origin from the exchange interaction between the free charge carriers and the localized d-electrons of the Mn ions. A large Faraday rotation and a Magnetic Circular Dichroism (MCD) signal measured in $Cd_{1-x}Mn_xTe$ [40] was attributed to the same mechanism and subsequently the field of DMS emerged.

These early examples of DMS, now sometimes termed "traditional" DMS [41], belong to the family of $A^{II}_{1-x}Mn_xB^{VI}$, where A^{II} and B^{VI} stand for Cd, Zn, Hg and S, Se, Te, respectively [28]. However, the low critical temperatures in these materials [42], making them impractical for spintronic devices led to a quick spread of the field to new material systems like $A^{II}_{1-x}Fe_xB^{VI}$ or $A^{II}_{1-x}Co_xB^{VI}$ [42, 43]. Rejuvenation in DMS research was the opening of a new material system in which ferromagnetism at relatively high temperatures was to be observed: the III-V semiconductors. A first report of MBE grown $In_{1-x}Mn_xAs$ on InAs and GaAs substrates showing ferromagnetism [44] was followed by many publications on III-V and II-VI materials,

[3]The citation numbers are taken from the ISI Web of Knowledge on the 12. April, 2011 using the Web of Science database with Conference Proceedings.

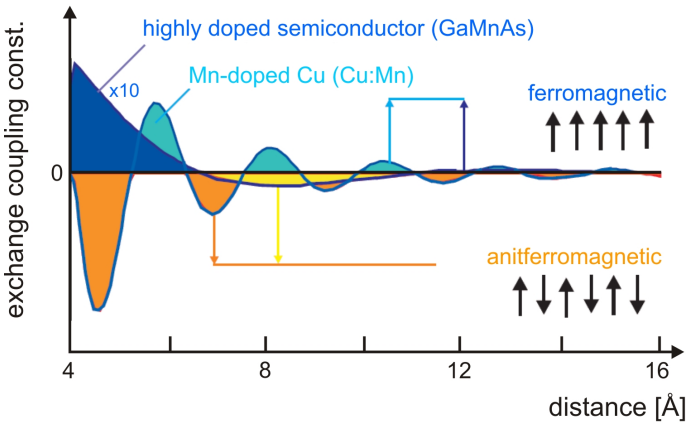

Figure 2.3: Illustration of the RKKY interaction in a semiconductor (GaMnAs) and a metal (Cu:Mn) adapted from [61]. The oscillatory behavior of the spin exchange constant is shown as a function of the distance of two Mn ions. The graph was calculated using an electron concentration of 8.5×10^{22} cm^{-3} in the case of Cu and a hole concentration in of 3.5×10^{20} cm^{-3} for GaMnAs. The graph shows that a long range ferromagnetic coupling is possible in the semiconductor material.

like GaMnAs [45], GaN, ZnO, ZnSe and a large number of review articles [3, 24, 46–52] describing the rapid growth of the field.

The need for high Curie temperatures (T_C) in DMS has kept the search for new materials active and indeed a big improvement could be made for example on the T_C reported for InMnAs and GaMnAs, which could be raised from initially below 10 K [53] and 110 K [38] to 343 K [54–56] and 185 K [57], respectively. For GaMnAs this was related to the progress in controlling crystal quality, namely reducing the number of unintentional charge and moment compensating defects through optimized growth and post-growth annealing procedures [58]. Among the highest T_C values reported for DMS are the ones for GaMnN (T_C=940 K [59]) and ZnCoO (T_C=790 K [60]), i.e. they are well above room temperature. However, it is still unclear what the driving forces behind the ferromagnetic behavior are. This leads us to a very important question in this field, the answer of which is essential for reliably controlling the magnetic properties in DMS: What mechanism makes a DMS work?

There have been many attempts to describe the mechanism responsible for ferromagnetism in semiconductors. To date, the situation is still not clear and no single theory exists to explain the origin and the large scatter of data of the magnetic properties of semiconductors. Three models of ferromagnetic mechanisms in DMS discussed in literature will be presented in the following.

The success of the mean field Zener model introduced by Dietl et al. [16] was founded on the ability to account for the experimentally observed Curie temperatures of $Ga_{1-x}Mn_xAs$[4] and $Zn_{1-x}Mn_xTe$. The scientists applied this model to a variety of DMS to predict their Curie temperature, as will be discussed in section 2.3. The basic idea of this model is that ferromagnetic interaction between localized spins of transition metal (TM) ions is mediated via holes introduced by shallow acceptor levels, provided by the Mn ions. The developed theory is based on the double-exchange (Zener model) [62, 63] and the Ruderman-Kittel-Kasuya-Yoshida (RKKY) [64–66] mechanism to explain the long range magnetic coupling of the moments. Double exchange is the term used to describe the ferromagnetic coupling between two differently charged transition metal ions (e.g. Mn^{3+} and Mn^{4+}) separated by an atom with a closed shell (e.g. Cl^- or O^{2-}). This is done by the transfer of an electron from one Mn ion to the central atom and a simultaneous transfer from the central atom to the next Mn ion, where the lowest energy of the system corresponds to a parallel alignment of the spins of the transition metal ions [63], hence a ferromagnetic coupling is established. The explanation of the long range coupling is then given by the RKKY interaction, where the spin orientation of free electrons is influenced by the local magnetization of the magnetic ions through the combined effect of coulomb- and spin dependent exchange-screening, originating from the Pauli principle. This so-called indirect super-exchange of magnetic moments is mediated by conduction carriers, which experience an oscillatory spin polarization, depending on the distance between the magnetic ions in the crystal. Fig. 2.3, where the exchange coupling constant is plotted as a function of the separation of Mn ions, demonstrates the long range ferromagnetic interaction in the semiconductor GaMnAs; but also shows that the coupling is much weaker than in a doped metal such as Cu:Mn. A major prerequisite to this kind of interaction is a large carrier concentration and a high doping concentration in semiconductors which is not necessarily the case in the DMS samples which have been fabricated. The observation of ferromagnetism in DMS with rather low doping concentration therefore demanded for the development of alternative models.

One such model, also accounting for ferromagnetism in low doped p- and n-type DMS, was put forward by Coey et al. [67], explaining that ferromagnetic coupling is mediated by electrons from shallow donor states, which create a spin-split impurity band when surpassing a donor defect concentration threshold and couple to the 3d moments of TM to form bound magnetic polarons (BMP). These polarons themselves couple to each other leading to a ferromagnetic interaction between the magnetic ions and when the polaron percolation threshold is reached the whole sample becomes ferromagnetic. An illustration of this mechanism is seen in Fig. 2.4. The authors state that the Curie temperature depends on both the magnetic impurity and the donor concentration in the material. This model is also supported by

[4]Measured $T_C = 110$ K, calculated $T_C = 120$ K.

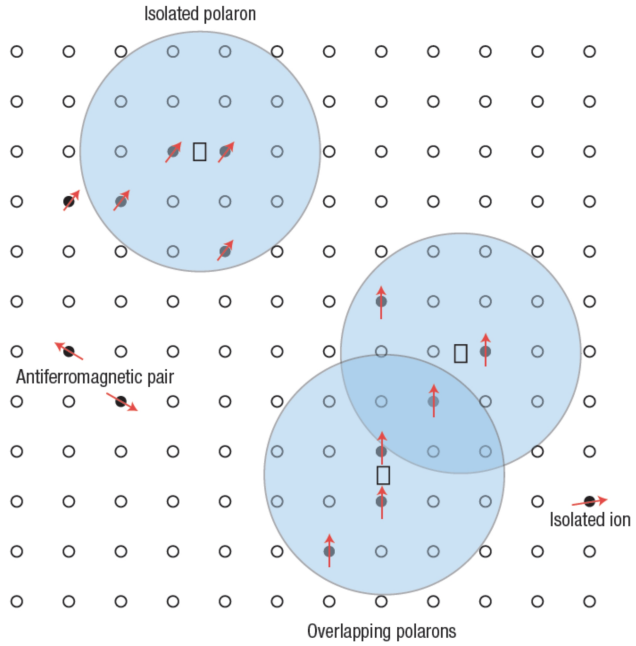

Figure 2.4: Representation of magnetic polarons. Small gray circles represent cation sites. Anion sites are not shown; anion vacancies are indicated by squares. Black circles stand for impurity (dopant) atoms. A donor electron in its hydrogenic orbit (large blue circles) couples antiparallel to impurities with a 3d shell that is half-full or more than half-full. From [67].

experimental results, e.g. [60], where charge carrier mediated magnetic coupling is ruled out and the predicted T_C by this theory lies in the vicinity of the measured one[5].

Another model of ferromagnetism in III-V materials was proposed by Litvinov et al. [68], who assume a contribution to the indirect exchange interaction by polarization of the valence band electrons via virtual electron excitation from magnetic impurity acceptor states to the valence band. This model explains the origin of ferromagnetic behavior for high and low carrier concentration by use of a percolation approach (like in the case of BMPs [67]) rather than a mean field theory (like in the case of the mean field Zener model [16]).

Despite the persistent efforts to clarify the picture of ferromagnetism in DMS also on the experimental side and to give input to the parameters used in the models, rather puzzling results are obtained. For example, none of the two opposing models relying

[5]The predicted T_C in this study was 822 K while the experiment gave $T_C \sim 790$ K.

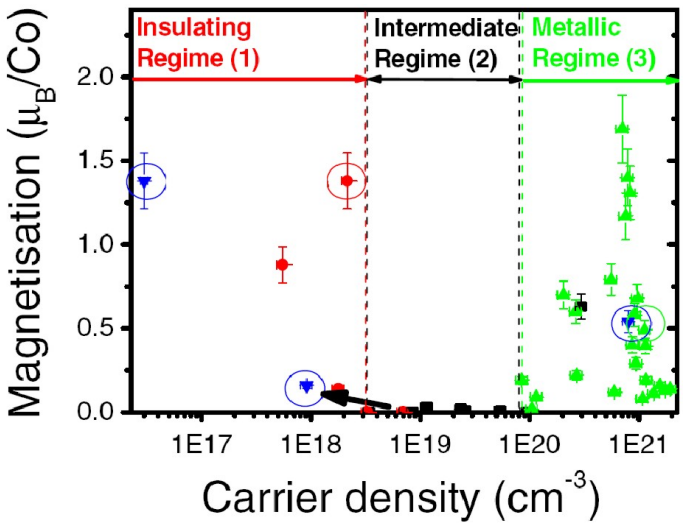

Figure 2.5: Room temperature magnetization for ZnO films with 5% Co and varying Al doping, as a function of the mobile carrier density. The graph is adapted from [75].

on carrier mediated interaction or a percolation mechanism can experimentally be evidenced. While some reports see no correlation between carrier concentration and ferromagnetic behavior in DMS [69–71], leading to the conclusion that free carrier mediated mechanisms do not apply, other publications show an increase of ferromagnetism with increasing free carrier concentration [72–74], indicating the opposite conclusion. Interestingly, a combination of both mechanisms in TM-doped ZnO was suggested by Behan et al. [75], saying that the carrier mediated exchange can account for ferromagnetism in samples with high free-carrier concentration, while the BMP model can be applied for samples with low free-carrier concentration. The observed paramagnetic behavior in the intermediate concentration is explained by the destruction of polaron coupling by hopping of free carriers. Fig. 2.5 illustrates this behavior in Behan et al.'s [75] data of the sample magnetization as a function of the free carrier concentration.

In addition, a more and more emerging influence of ferromagnetic behavior in DMS was attributed to the role of structural defects in semiconductors, both theoretically [76, 77] and experimentally [19, 70, 71, 78–80]. However, exact mechanisms still remain unclear. A discussion of defects related to ferromagnetism in Mn-, Gd- and Cu-doped GaN is presented in the following section.

Table 2.1: Calculated Curie temperatures of zinc-blende (except where noted otherwise) p-type semiconductors containing 5% Mn and 3.5×10^{20} holes per cm^3 [16]. GaN is the candidate with the highest expected T_C.

Semiconductor	**Curie temperature [K]**
Si	120
Ge	72
AlP	212
AlAs	121
GaN (zinc-blende)	426
GaN (wurtzite)	400
GaP	101
GaAs	107
GaSb	42
InP	62
InAs	44
ZnO (wurtzite)	315
ZnSe	44
ZnTe	31

2.3 The role of nitrides in spintronics

Group III-Nitrides are a group of semiconductors with a multitude of beneficial properties. These include high chemical, thermal and mechanical stability, the fact that none of the components are toxic and at least one of the components is readily available, owing to the high abundance of nitrogen on our planet. The wide tuning ability of their direct band gap between 0.7 eV for InN over 3.4 eV for GaN up to 6.2 eV for AlN make these nitrides a very attractive material for optical devices and have therefore been subject to great interest both for research and for commercial purposes.

In spite of the advantageous properties of nitrides, they were not among the first semiconductors to be attempted to be made ferromagnetic. An increased interest in this material however came about when Dietl et al. [16] set up their theoretical model of ferromagnetism in DMS based on the Zener model [62, 63] and calculated Curie temperatures that could be achieved in various semiconductors (see Table 2.1). Their extraordinary results indicated the highest T_C of all the considered materials and ferromagnetism for GaN above room temperature! In their paper they show that the mean field Zener model, usually applied to describe ferromagnetism in transition metals, is able to explain the experimental Curie temperatures of GaMnAs and ZnMnTe, and applied this model to the different DMS listed in Table 2.1.

Of course the picture is not as easy as it seems, for, although production possibilities for high quality GaN have greatly improved over the years, the prerequisites for room temperature ferromagnetism are not easily matched. If ferromagnetic coupling is indeed mediated by free charge carriers, as the mean field Zener model of Dietl et al. suggests, one of the main difficulties for GaN DMS may lie in the achievement of the necessary high hole concentration and mobility. GaN is known to be intrinsically n-type [81], mostly due to Ga vacancies [5, pp.929], and overcoming the difficulty of efficiently making GaN p-type is sometimes even seen as "the Holy Grail" in GaN device production [82].

Another critical aspect for spintronic devices is the electron spin relaxation time in the spin transport material. Motivated by theoretically predicted long spin life times in bulk GaN to be in the micro second range [83], which was consistent with the expectation of long spin relaxation times in a material with weak spin-orbit interaction and a wide band gap [84], GaN seemed to fulfill very promising properties for a spin transport material. Experimental investigations using spin-dependent pump and probe reflectance measurement however showed a very fast spin relaxation in bulk GaN [85] (470 fs at 150 K and 250 fs at 225 K) and also bulk InGaN [86], where no polarization of the electrons could be observed, limited by a time resolution (350 fs) of the setup.

A first report of time resolved photoluminescence measurements on an InGaN multiple quantum well (MQW) structure by Julier et al. [87] states a relatively long spin relaxation time of $\sim$100 ps at 10 K, while subsequent analyses of different InGaN/GaN MQW structures for spin LED application reported on very much shorter spin relaxation times measured by circularly polarized pump-probe spectroscopy [84, 86, 88–90], i.e. 200 ps at 200 K and 70 ps at 295 K [91], for other samples even 450 fs at 5 K [84]. These fast relaxation times are believed to result from considerable biaxial strain at the heterostructure interfaces leading to large piezoelectric fields in wurtzite GaN grown along the c-axis, distorting the QW potential. The thereby breaking of the confining symmetry of the quantum well leads to a large Rashba spin-orbit splitting [90] causing a mixing of the spin states in the conduction band and hence fast spin relaxation.

Substantially longer spin-relaxation times are expected [4] for structures lacking the above described internal electric fields, as in for example cubic symmetry lattices. However, the cubic symmetric crystal structure of GaN is only a meta stable phase and cannot easily be obtained in high phase purity. Another way to avoid the electronic band bending caused by the internal electric fields is to tilt the polar axis of the wurtzite material in such a way, that it lies parallel to the growth plane rather than in growth direction. This can be achieved by growth on the so-called M- and A-planes of GaN, as will be described in more detail in chapter 3.2.

A very interesting observation in this context was made by Nagahara et al. [91, 92] who (in addition to a short spin life time in low In (7.1%) content MQW samples) measured long-lived (220 ± 40 ps) and temperature independent electron spin states in high In fraction (10.6%) samples. This result was attributed to the formation of In quantum dots (QD) as a consequence of the compositional fluctuations in the InGaN QWs, meaning that an In phase separation led to In QDs imbedded in the MQW structure. Due to the confining properties of QDs causing a discrete density of states and the lack of a continuum of states available for spin relaxation, the scattering processes in QDs are suppressed and a longer spin life time is expected compared to QW structures [93]. Further, as discussed in section 3.2 the effects of internal electric fields in nitrides are less pronounced in smaller structures, as is demonstrated by investigations of samples with different QW thicknesses, e.g. in [94, 95].

Fueled by the prospects of an all-GaN based spintronic device and the predicted room temperature ferromagnetism, a lot of research was directed into GaN-based DMS. The majority of work, done in this field, investigated ferromagnetism in Mn-doped GaN, but other doping materials such as Cr, Fe, Co, Gd and Cu were also considered. In the following a short account of research results will be given for the exemplary cases of Mn, Gd and Cu doped GaN. Indeed, high Curie temperatures were found for different doping concentrations for samples produced either by direct incorporation of the dopant during a growth process like MBE or ion implanted samples, where the dopants were introduced into a bulk sample.

2.3.1 Mn-doped GaN

For MBE grown GaN:Mn samples a very large scatter of Curie temperatures was found ranging from 10-25 K[6] [96] to "T_C higher than room temperature[7]" [97] up to 940 K [59]. The highest reported T_C of 940 K was estimated[8] by Sonoda et al. [59] for their, probably n-type, $Ga_{0.91}Mn_{0.09}N$ sample. Similarly, Dhar et al. [98] found ferromagnetism in 13.7%[9] Mn-doped GaN up to ∼750 K, but see an antiferromagnetic behavior in a homogeneous 7.6% Mn-doped GaN sample, ascribed to a Mn-Mn interaction in the insulating GaMnN sample.

[6] Sample with 7% Mn fraction, measured by Auger Electron Spectroscopy (AES) depth profiling, and a homogeneous incorporation of Mn, relying on XRD measurements.

[7] For samples investigated by Superconducting Quantum Interference Device (SQUID) with Mn content 3-9% (measured by AES). No Mn related clusters were found by XRD or XTEM.

[8] The temperature limit of the SQUID setup, used to measure the magnetization of the sample was 750 K.

[9] Measured by Secondary Ion Mass Spectroscopy (SIMS).

The huge range in T_C of MBE grown GaMnN can possibly be traced back to the presence of nano scale Mn-clusters inside some of the GaN samples. There is however a controversy to this matter, namely while Dhar et al. ascribe the ferromagnetic behavior at the highest temperatures to the formation of miniscule Mn-rich clusters formed during the MBE growth that are too small to be detected in X-ray Diffraction (XRD), Sonoda et al. deny the existence of Mn clusters relying on XRD [59], Rutherford Back Scattering (RBS) and Extended X-ray Absorption Fine Structure (EXAFS) [99] measurements. While Dhar et al. mention that MnGa phases can reach Curie temperatures greater than 600° ($T_C = 748$ K reported for $Mn_{66.7}Ga_{33.3}$ [100]) and that the nitride compound Mn_4N is ferrimagnetic [101] up to $T_C = 738$ K [102], the Sonoda collaboration claims that the high T_C value of 940 K cannot be explained by such clusters. To further investigate and clarify the facts in this discussion Ando et al. [103] investigated one of Sonoda et al.'s samples, namely sample B of ref. [59][10] with 6.8% Mn content, which also showed ferromagnetism at a temperature higher than room temperature [103], by Magnetic Circular Dichroism (MCD). The sample only showed a paramagnetic behavior and it is concluded, that the observed ferromagnetic behavior must be assigned to an unidentified material, also in the film, but undetectable by XRD. The discussion clearly shows the need for a big diversity of experimental methods to tackle the intricate question of what is going on in these materials.

Common to all the above mentioned reports is a discussion about Mn clusters giving rise to the high Curie temperatures. Almost all groups state that such second-phase inclusions could not be found by XRD or sometimes even by TEM. However, as stated in [98], [103], [104] and [51] the size of Mn clusters can be too small to be detected by these methods. Further, the magnetic characterization of the samples was mainly performed by SQUID, the Vibrating Sample Magnetometer (VSM) or using the Anomalous Hall Effect (AHE). These are all methods probing the total magnetization in the sample, as opposed to element specific methods, where clustering effects can be differentiated.

Groups using other production methods for Mn-doped GaN find Curie temperatures of 250 K [105] and 300 K [106][11] for ion implanted samples and 228-370 K [107] for MOCVD grown GaN samples with post growth doping by solid state diffusion from a Mn source. It is stated in these reports (e.g. [107]) that the magnetic behavior depends strongly on the growth conditions, post-growth procedures and, as can be seen by the spread of experimental data, they also depend on the fabrication method. Especially the effect of post-growth annealing at different temperatures influences the magnetic properties of the sample severely and raises the question of Mn clustering again as can be seen in the example of Baik et al. [104] who found

[10] Unfortunately this is not sample A (9% Mn), which showed the high Curie temperature of 940 K.

[11] In this case Mn ions were implanted in p-type cubic GaN.

ferromagnetic behavior in their Mn implanted GaN samples only after annealing at 800°C. By the use of Synchrotron Radiation Photoemission Spectroscopy (SRPES) the magnetic behavior was attributed to the formation of Ga-Mn bonds, probably a Mn_3Ga phase, which could not even be observed in Synchrotron XRD. By equivalent means they found annealing at 900°C to reduce the magnetic behavior due to the formation of Mn-N compounds, such as Mn_3N_2 and $Mn_6N_{2.58}$, which couple antiferromagnetically [102], hence reducing the magnetic moment.

It has been proposed that ferromagnetic properties can be influenced by the formation of vacancy or vacancy complex defects [76, 77] that are altered during annealing. The existence of such complex defects has experimentally been verified in a positron annihilation study of vacancy type defects in Mn-doped GaN grown by MOCVD [108] where a new kind of defect, identified as a V_N-Mn_{Ga} complex, was found. At this stage, it is however unclear to what extent these defects play a role in the ferromagnetic behavior of Mn-doped GaN. The question about defect related ferromagnetism is also treated e.g. in ZnO based DMS [109]. In this work, however, we shall stay with the nitrides and discuss this issue in Gd- and Cu-doped GaN in the following two sections.

Many questions concerning the mechanisms and microscopic origins of ferromagnetism in these new material systems continue to drive research further and have led to different methods of investigation and the development of new ideas for an explanation of the experimental data as also the next example of Gd-doped GaN will show.

2.3.2 Gd-doped GaN

As investigations dig deeper into the understanding of the values for the differing Curie temperatures, the understanding of mechanisms for ferromagnetism in these systems is continuously improved. To illustrate this, the case of Gd-doped GaN shall be briefly sketched in the following.

In 2005 Dhar et al. [69] reported an enormous magnetic moment of up to 4000 μB per Gd atom in Gd-doped GaN samples grown by reactive molecular beam epitaxy (RMBE). The magnetic investigation of the samples in this work was done by SQUID for temperatures up to 360 K where all samples still showed a magnetic hysteresis curve, meaning that the Curie temperature lies above the maximum measured value of 360 K. Possible clusters like GdN or Gd could only account for T_C values up to 60 K [110] and 293 K [111], respectively. This material system was then investigated by an element specific investigation method, namely X-ray Magnetic Circular Dichroism (XMCD) [112], by Ney et al. [113] to probe the ferromagnetism in Gd-doped GaN. They found only a very weak magnetic polarization of Gd atoms,

which could not explain the huge magnetic moment reported earlier. Further, they identified very small Gd clusters already in a 0.05% Gd-doped GaN sample, which could give rise to the detected XMCD signal. However, this cannot account for the observed magnetic data above 360 K by SQUID. Hence, it was stated that there must be other mechanisms involved in leading to the ferromagnetic behavior. Indeed, the notion that defects could play an important role in the mechanism of ferromagnetism in this material was expressed by Dhar et al. in the conclusion of another study [78] where they found that the effective magnetic moment per Gd ions was increased by an order of magnitude when Gd ions were implanted into GaN rather than incorporated during epitaxial growth. Since implantation methods increase the density of defects in a crystal, the measured drastic increase of magnetic moment per TM atom, in the as-implanted samples, was assumed to be defect related.

This kind of uncertainty of where the ferromagnetism really comes from has led to a somewhat skeptical view on the reports of new DMS with room temperature ferromagnetism, and the call for more experimental evidence probing different aspects of the magnetic interactions inside the material has risen to clarify the origin of the ferromagnetic behavior.

Here we find a somewhat similar situation as in the case of Mn-doped GaN, where some component of the material, other than the simple interaction of the substitutional doped magnetic ions, is needed for the explanation of the magnetic data. One could slightly be reminded of the search for dark matter in the universe, of which we can see the effects and consequences, but when asking what dark matter is, we only have unconfirmed theories or can experimentally exclude some of them, but a clear experimental indication of what it actually is, is still missing.

In the following final part of this chapter concerned with Cu-doped GaN, further possibilities of ferromagnetic behavior in nitrides will be described. It will be possible to exclude one major source of confusion and difficulty, namely the formation of magnetic clusters due to the dopant, which is already one of the main motivations for using Cu-doping in DMS.

2.3.3 Cu-doped GaN

Cu is not a magnetic element and may at first not seem to fulfill the DMS criteria, however, when implanted on Ga substitutional sites in GaN it becomes a magnetic impurity owing to its Cu 2^+ state. It has hence been considered as a dopant for GaN DMS. Investigations are simplified because of the lack of disturbances in the formation of magnetic clusters. Neither Cu-Cu clusters, nor Cu-Ga or Cu-N compounds have been seen to exhibit ferromagnetism, providing a very promising approach for answering the question of the origin of ferromagnetism in DMS materials.

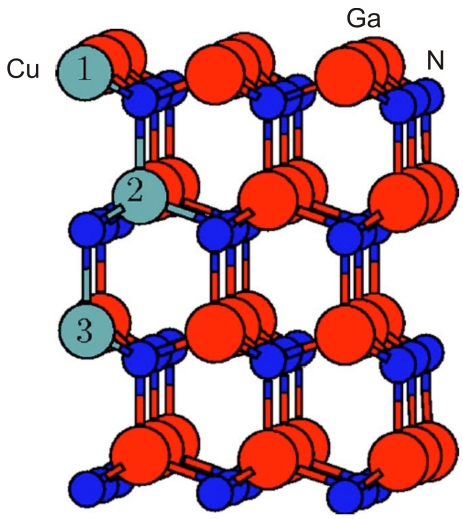

Figure 2.6: GaN supercell with 72 atoms used in the calculations of Rosa et al. [114] for 5.6% Cu concentration. Positions 1 and 2 of the Cu atoms indicate the "close" and positions 1 and 3 the "far" configuration of Cu incorporation. The schematic is taken from [114].

First interest in Cu-doped GaN as a DMS was initiated by a theoretical study of Wu et al. [17], where first principles Density Functional Theory (DFT) calculations showed 100% spin polarization of the conduction carriers and an expected Curie temperature of 350 K. These properties were seen to be the result of strong p-d hybridization between the Cu 3d and the N 2p states, leading to a spin polarization of the N anions, themselves coupling to other dopants and hence providing for an indirect magnetic coupling among the dopants.

One year later, Rosa and Ahuja [114] revealed in DFT calculations, that Cu-doped GaN does not show robust ferromagnetism and is therefore not suitable as a spin-aligner in spintronic applications. These, at first sight, rather contradicting theoretical results demonstrated the need for experimental data on Cu-doped GaN. In fact, the predictions of [17] and [114] do not contradict each other. Rosa and Ahuja explain that Wu et al.'s results are reproduced in good agreement when choosing a larger separation between two Cu atoms in the GaN supercell ("far" configuration), but the energetically more favorable "close" configuration of two Cu atoms in GaN lead to a significant decrease of the magnetic moments on both the Cu and the N atoms. Fig. 2.6 illustrates the meaning of "far" and "close" configuration. Further, it is stated that the influence of defects in the crystal (which was not investigated) could contribute to an enhancement or reduction of the magnetic moments.

Another report, using ab-initio calculations based on DFT, on Cu-doped GaN, supporting the thesis of a strong p-d hybridization in more detail as a consequence of the crystal field splitting, which a Cu ion experiences in the tetrahedral environment of GaN was published by Lee et al. [115]. The authors evaluate the prospects of GaN:Cu and GaN:Mn as suitable DMS for spintronic purposes and conclude that, because of a more delocalized character of the carriers in Cu-doped GaN resulting essentially from the smaller difference of electronegativities between Cu and N as compared to Mn and N, there is a long range valence band splitting leading to a long range magnetic interaction between the dopants in GaN:Cu, while the valence band splitting in GaN:Mn and its magnetic moment is rather concentrated at the transition element. These findings lead the authors to the statement that GaN:Cu fulfills the criteria of a successful DMS material and is even more promising than GaN:Mn.

Indeed, above room temperature, ferromagnetism was found in numerous investigations [18–20, 80, 116, 117] of GaN:Cu. As an example, Figure 2.7 shows the persistence of a measured magnetic moment up to 400 K, i.e. well above room temperature, in a sample grown by plasma assisted molecular beam epitaxy. The first experimental evidence for ferromagnetism in Cu-doped GaN, however, came from a study where Cu was implanted into a GaN bulk crystal [116]. After annealing, the samples showed room temperature ferromagnetism. However, no ferromagnetic behavior was observed in samples which were not annealed or annealed at a too high temperature (leading to clustering of Cu). The study does not explain the origin of the observed ferromagnetism, but states that, since annealing affects the damage recovery after implantation, damage in the samples or secondary phases (Cu clusters) do not contribute to the observed ferromagnetism at room temperature. It is interesting to note, that in the case of GaMnN and GaGdN clustering of the dopants forms magnetic impurities, leading to an ambiguous origin of the magnetic signals, the clustering of Cu ions, on the other hand, seems to diminish the ferromagnetic behavior of the samples.

Shortly after this report, Seong et al. [18] published a paper on room temperature ferromagnetism observed in Cu-doped GaN nanowires. The authors explain that their nanowires are defect free and defects can hence not be the origin of the magnetic behavior. Further they state that Cu atoms take part in the wurtzite GaN lattice, suggesting a substitutional site occupation of Cu atoms. With XMCD measurements at the L-edge of Cu a magnetic moment could be measured at the Cu ions, proving the participating role of Cu to the observation of ferromagnetism in the nanowires.

Up to this point the situation seemed to be very encouraging. Experimental results were consistent, room temperature ferromagnetism had been established and no disturbing effects from clusters could be observed. However, the sound world of explaining ferromagnetic behavior in Cu-doped GaN was found to be more com-

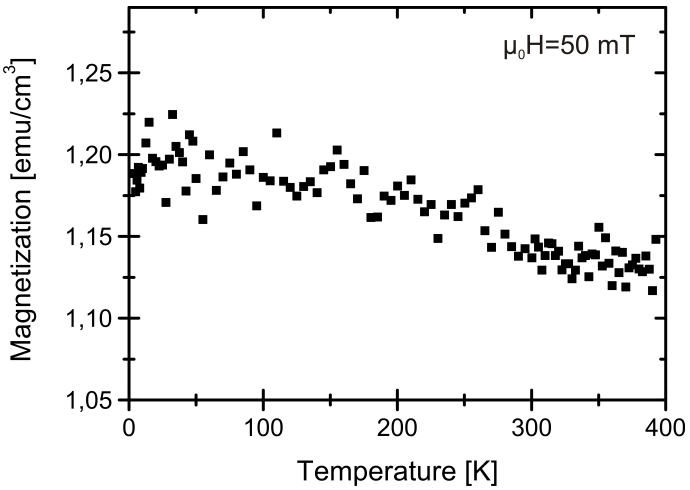

Figure 2.7: SQUID measurements of the magnetization as a function of temperature of a Cu-doped GaN sample, showing ferromagnetic behavior well above room temperature. Graph taken form [117].

plicated and discussions about the magnetic origin arose, e.g. by Yang et al. [19] claiming that the origin of ferromagnetism in these systems could not be explained by the p-d hybridization of Cu and N atoms [17], due to the low dopant and carrier concentrations present in their samples, which could therefore not account for the long range interaction necessary for the ferromagnetic behavior. Yang et al. had seen Ga vacancy related signals in their PL spectra and instead argue, that the observed magnetic moments are probably a result of defect related structures, such as Ga vacancies (V_{Ga}) or Cu-N vacancy (Cu_{Ga} - V_N) complexes, which could provide for the long range ferromagnetic interaction [76] and have even been proposed to solely account for ferromagnetic behavior in undoped GaN [77]. These arguments were supported by the findings of Madhu et al. [118] who communicated in an article that undoped GaN nanoparticles exhibit room temperature ferromagnetism. The authors ascribe the ferromagnetic behavior of the pure GaN particles to defects at the surface, stating that ferromagnetism and defect density decrease when particle sizes increase. It is argued that the formation energy of Ga vacancies may be dramatically different for nano size particles than for bulk GaN and hence ferromagnetism has not yet been observed in undoped bulk GaN.

Like in theoretical studies, seeming contradictions have risen in the experimental findings. Some studies exclude defect related ferromagnetism while others strongly point towards it. Although the understanding of the actual mechanisms at work is still incomplete, the nature of a possible answer to the questions is already sketched. While not going into details about ZnO, but just acknowledging the similarities (e.g.

crystal structure, band gap) to GaN, studies on ZnO based DMS hint strongly to the presence of a multitude of mechanisms and origins of ferromagnetism in DMS [75, 109].

Other studies of Cu-doped GaN by Sun et al. [80, 119, 120] investigating Cu implantation in non-polar *A*-plane GaN grown on *R*-plane sapphire with subsequent annealing found ferromagnetic behavior up to a temperature of 380 K [120]. They studied the influence of the implantation dose and annealing of the samples and point out that Cu mostly occupies interstitial sites in as-implanted samples but changes to Ga substitutional sites after annealing. In addition, the defects in the lattice are influenced by the annealing step; the common assumption is a damage recovery. Because no ferromagnetic behavior was found in any of the as-grown or as-implanted samples in these studies [120] nor has there been any report about undoped bulk GaN being ferromagnetic, it is concluded that *only* defects cannot be responsible for the observed magnetism. However, the authors also claim the same argument as Yang et al. [19], namely that the doping concentration in the samples is too low to explain the ferromagnetism by the p-d hybridization model [17] and hence plead for an explanation where Cu-defect interaction or defect mediated interaction between the Cu ions should be considered.

An interesting aspect of the work of Sun et al. [120], which strongly relates to the topic of this thesis, is the comparison of the magnetic behavior of Cu implanted non-polar *A*-plane GaN to polar *C*-plane GaN, finding that the non-polar sample yields a four times higher saturation and remanent magnetization than the polar one. This is speculatively attributed to the observation of a higher substitution incorporation efficiency of Cu in the non-polar GaN sample.

Recently, an investigation of vacancy type defects in Cu-doped GaN [121] gave insights to the annealing effects in the material. Samples were produced by in-diffusion of Cu from the surface into a bulk GaN wafer at 873 K and were expected to be oversaturated with Cu when quenched to room temperature after 96 h. A series of samples, produced in this way, was annealed at different temperatures up to 850 K and investigated by vacancy type defect sensitive positron annihilation experiments. The researchers found, that vacancy-type defects are clearly introduced into the lattice when annealing up to a temperature of 550 K, while at higher temperatures the results indicate two possibilities, namely a healing of the defects or an enlargement of the vacancies into large vacancy clusters. The observed effects were related to the out-diffusion of Cu from the samples.

In order to get to the bottom of the questions on this topic it is of great importance to clarify the most basic properties of the samples involved. One of these fundamental properties is the question of how and where Cu atoms are incorporated in the host GaN matrix. This shall be discussed in detail on a series of MBE grown GaN:Cu samples in chapter 5.

3 Properties and fabrication of GaN

To investigate GaN as a prospective DMS material it is important to first get an understanding of the GaN host material and its related benefits and issues. The following chapter gives an overview of key properties and parameters of GaN relevant for the present study, as well as an introduction into its fabrication process and the related difficulties. Starting with the most basic characteristics of GaN crystals the focus will continue on the important internal electric fields in GaN in section 3.2, their consequences and how they can be circumvented. Moving on to the manufacturing of GaN and some of its challenges (section 3.3), the important topic of substrates for GaN epitaxy will also be discussed in section 3.3.1. Finalizing this chapter will be a short description of the method of molecular beam epitaxy, the material deposition method used in this work.

3.1 Basic parameters and crystal structure of GaN

There are two phases of GaN with different crystal structures. One of them is the meta stable cubic zinc-blende phase. This work, however, concentrates on the stable hexagonal wurtzite phase and all properties discussed in the following concern GaN in this later crystal structure. The space group symmetry of wurtzitic GaN is C_{6v}^4−$P6_3mc$ (#186) or using the Pearson symbol hP4. The unit cell consists of two N and two Ga atoms; each of the atoms experiences a tetrahedral bond configuration with four of the other atom species (see Fig. 3.1 (a)). For the description of hexagonal symmetric crystals, four coordinates (a_1, a_2, a_3 and c) are most conveniently used and crystal planes are described by the Bravais-Miller indices consisting of four digits (hkil), where h, k and l are the Miller-indices and $-i = h + k$. In Fig. 3.1 (b) the most important planes are shown with their Bravais-Miller indices and the name for the family of equivalent planes, e.g. *M*-plane for all $\{1\bar{1}00\}$ planes.

There is a distinct difference between the two directions [0001] and $[000\bar{1}]$ of the GaN *C*-plane. The crystal surface with direction [0001] is also termed Ga-polarity or (+c) and constitutes the state where the three bonds of Ga to N building the base of the tetragon are facing downward toward the substrate. The case is just turned around for N-polarity or (-c), $[000\bar{1}]$, which is when the three bonds of the N atoms face the substrate. Note, that it does not matter whether the top surface

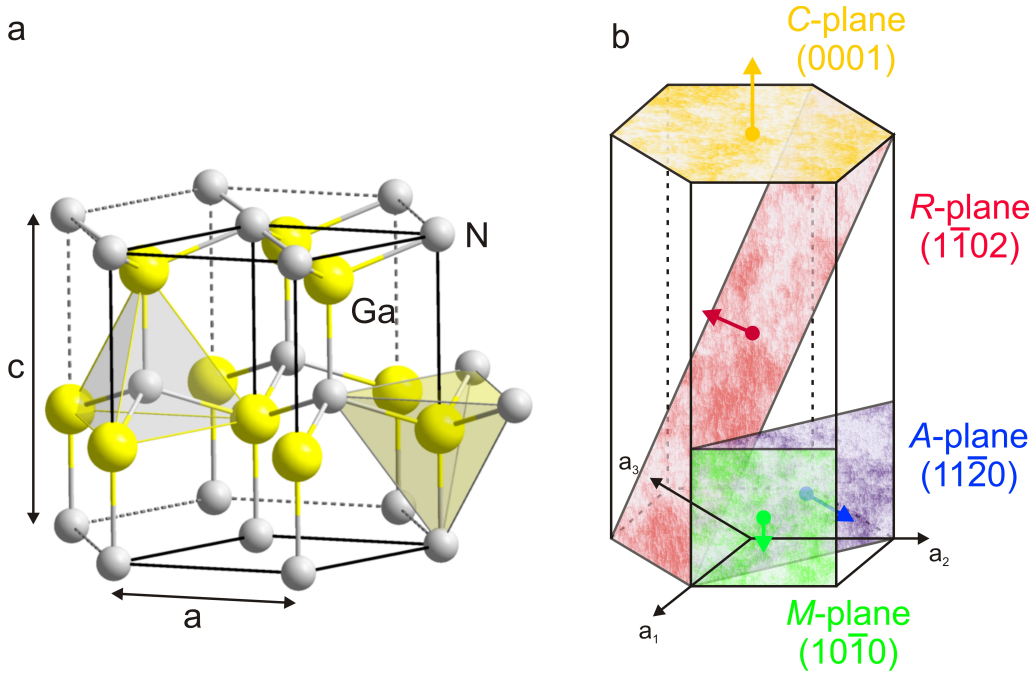

Figure 3.1: (a) Schematic of the GaN wurtzite crystal structure, from [122]. The black solid lines outline the unit cell; the tetrahedral symmetry is indicated by the grey pyramids and the lattice constants a and c are also shown. (b) Hexagonal crystal structure of GaN showing the most discussed planes and their labels.

of the material is terminated by N or Ga atoms; rather the symmetry of bonds in the crystal is changed. Effects of the different polarities, such as higher thermal stability and higher incorporation rates of dopants, but a rougher and poorer quality of films grown in N-polarity have been observed [123]. In current research, efforts are undertaken to expand the smooth film growth regime to N-polarity in order to exploit its benefits. This is also discussed in the context of p-type doping in section 3.3.

Due to the partly ionic bonding nature between N and Ga, the wurtzite structure of GaN is polar in the c-direction [0001], i.e. it has a single polar axis perpendicular to the C-plane (0001). Nitrogen exhibits a higher electronegativity than gallium and thus causes a slight deviation of the GaN crystal structure from the ideal wurtzite structure. The consequences of this fact is discussed in detail in the next section (3.2).

The lattice constants and coefficients of thermal expansion (CTE) are important parameters to be considered for epitaxial growth of GaN. While a large lattice mismatch between GaN and the substrate causes stress and strain into the film or even may lead to a non-epitaxial deposition. A mismatch of the CTE may be responsible for additional strain or induce cracking of the epitaxial film when cooling down the sample from growth temperature to room temperature. Their values along with other parameter information on GaN are given in Table 3.1.

GaN is optically very interesting due to its direct band gap of E_g=3.437 eV [131] at room temperature (290 K) or E_g=3.503 eV [126] at low temperature (1.6 K). This corresponds to a wavelength of λ=361.7 nm and 353.9 nm, respectively, which lies in the near ultra violet region. Hence GaN belongs to the family of wide bad gap semiconductors and is considered as a convenient material for blue and green LED and laser diode (LD) applications.

3.2 Internal fields in GaN

One of the big issues in nitride semiconductors are the polarization effects that are inherently present in their wurtzite structure and evoke the presence of electric fields inside the semiconductor [132, 133]. The origin of the polarization of GaN can be divided into two parts, namely the spontaneous- and the piezoelectric polarization. While the piezoelectric polarization comes about due to strain and stress in the crystal structure, especially at heterostructure interfaces, leading to a distortion of the crystal symmetry and therefore yielding a net polarization, the spontaneous polarization is always present and results from the natural deviation of the nitrides' crystal structure from the perfect wurtzite symmetry. As a result wurtzite GaN accommodates a polar axis running along the [0001] c-axis.

Table 3.1: Properties of GaN at 300 K.

Parameter	Value	Reference
Space group	$P6_3mc$	
Lattice constants at (25°C) [Å]		
a	3.1890(3)	[124]
c	5.1864(2)	
linear thermal expansion coefficients at high T≈ 600 − 1000 K [1/K]		
a	$6.20 \pm 0.4 \times 10^{-6}$	[125]
c	$5.70 \pm 0.5 \times 10^{-6}$	
Band gap [eV]		
at 1.6 K	3.503	[126]
at 290 K	3.437	
Molar mass [g/mol]	83.7267	[5]
Density [g/cm^3]	6.15	[127]
Melting point at 1 atm [K]	2550	calculated [128]
Debye temperature (T=12-1025 K) [K]		
∥a	868 ± 20	[125]
∥c	898 ± 24	
Electron affinity [eV]	4.1	[127]
Young's modulus of elasticity [GaP]	210 ± 23	[129]
Elastic constants [GPa]		
C_{11}	390 ± 15	[130]
C_{33}	398 ± 20	
C_{44}	105 ± 10	
C_{66}	123 ± 10	
C_{12}	145 ± 20	
C_{13}	106 ± 20	

For device applications like an LED, it is necessary to build a heterostructure of different materials on top of one another in MQW or QD structures. In such structures grown along the c-direction, i.e. parallel to the polar axis of the wurtzite crystal, the polarization causes charges to build up at the interfaces, which give rise to internal electric fields as indicated in Fig. 3.2 (a), and resulting in the so-called Quantum Confined Stark Effect (QCSE). The effect of the internal electric field on the electronic band structure causes the electronic bands in the semiconductor to deviate from the flat band structure, which would be the case in absence of electric fields. The electronic band bending in a GaN/InGaN/GaN structure, as can be seen in Fig. 3.2 (b), causes the electrons and holes to spatially separate in the QW or QD leading to a reduced wave function overlap and hence to a lower radiative

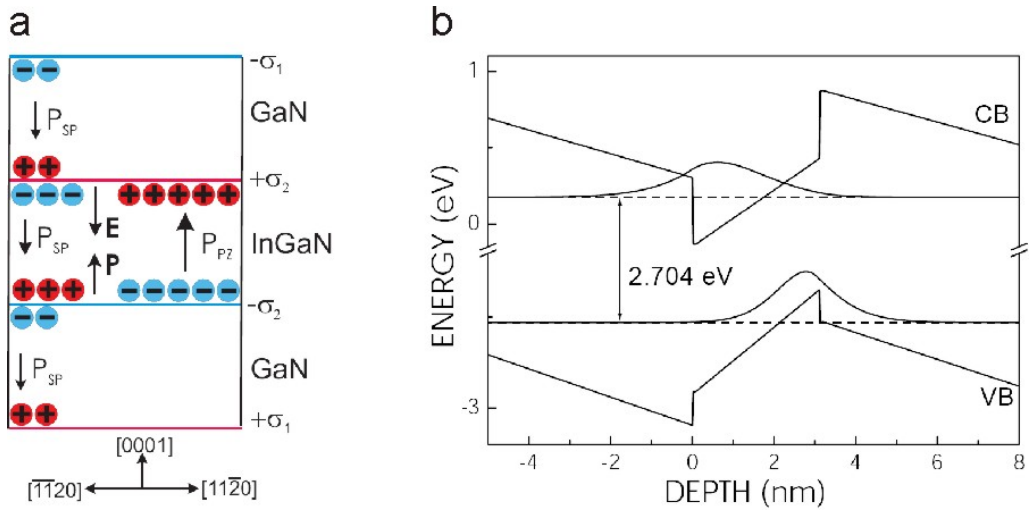

Figure 3.2: (a) Schematic indication of the influence of electrical polarization in a GaN/InGaN/GaN MQW structure grown on polar (0001) GaN. The total polarization change of the individual layers leads to the accumulation of charges at the interfaces, evoking internal electrostatic fields. P_{SP} and P_{PZ} denote spontaneous and piezoelectric polarization, respectively. σ_1 and σ_2 stand for the different stress at the interfaces. (b) Calculated band profile for a 10-period (3 nm $In_{0.15}Ga_{0.85}N$)/(7 nm GaN) MQW indicating the electron-hole wave functions. CB and VB are the conduction band and valence band, respectively. Figure adapted from [135].

transition probability. Owing to the prolonged radiative transition life time, non radiative de-excitation channels gain more importance and the probability of carriers captured by non radiative centers is increased. A further consequence of the band distortion is a red shift in the transition energy compared to flat bands, as can easily be deduced from graph 3.2 (b). The QCSE is also seen to depend on the quantum well thickness where a reduction of the radiative transition probability and a red shift with increasing QW thickness is observed [94, 95, 133, 134].

Ways to circumvent the effects of internal electric fields that are built up at heterostructure interfaces in nitrides have been proposed. One way is to make use of the cubic zinc-blende structure of nitrides, where the polarization effects cancel out due to the underlying crystal symmetry[1]. In this approach however GaN samples of the thermodynamically less stable zinc-blende phase often show fractions with

[1]In zinc-blende structure four symmetry equivalent polar axis along the ⟨111⟩ directions cancel each others' polarization contributions.

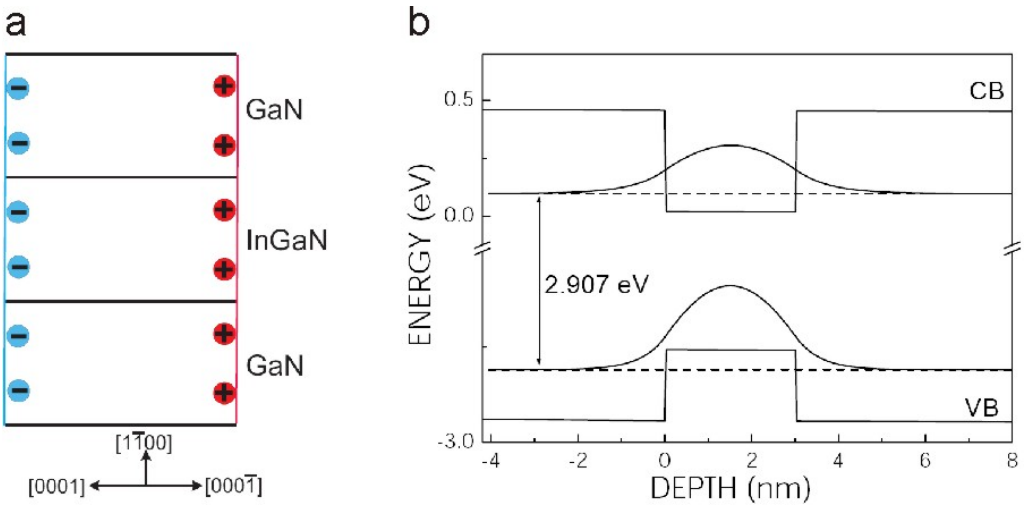

Figure 3.3: (a) Schematic indication of the influence of electrical polarization in a GaN/InGaN/GaN MQW structure grown on non-polar (1$\bar{1}$00) GaN. No internal electrostatic fields are present along the growth direction. (b) Calculated band profile for a 10-period (3 nm $In_{0.15}Ga_{0.85}N$)/(7 nm GaN) MQW indicating the electron-hole wavefunctions. CB and VB are the conduction band and valence band, respectively. Figure adapted from [135].

wurtzite symmetry [136, 137]. A different ansatz, which is the one that this thesis is based on, is to grow wurtzite GaN in a direction deviating from the [0001] direction also referred to as semi-polar or non-polar faces. Crystal directions perpendicular to the c-axis, like the $\langle 1\bar{1}00\rangle$ or $\langle 11\bar{2}0\rangle$ directions, resulting in M- or A-plane GaN, respectively, are termed non-polar, while any other inclinations of the crystal c-axis to the substrate are called semi-polar. Semi-polar growth of GaN reduces the electric fields in growth direction, whereas in non-polar structures, the intrinsic spontaneous polarization of the crystal lies parallel to the film surface and no electric fields are built up that distort the electronic band structure. Further, the piezoelectric polarization vanishes [138] for growth directions tilted 90° from the c-axis, resulting in flat bands at the interfaces of QWs. This situation is depicted for an M-plane GaN/InGaN/GaN structure in Fig. 3.3, equivalent to Fig. 3.2 for C-plane GaN.

Indeed, the effects of the QCSE could experimentally be observed when comparing structures grown on polar and non-polar planes. In GaN/AlGaN MQW structures grown on 6H-SiC (0001) and γ-$LiAlO_2$ (100), resulting in GaN (0001) and GaN (1$\bar{1}$00), respectively, Waltereit et al. [13, 139] demonstrated that the transition energy was significantly blue shifted (by $\sim$ 120 meV) and that the radiative lifetime is roughly ten times shorter for the non-polar sample. In another study Craven et

al. [95] investigated the PL dependence on the quantum well width of non-polar and polar GaN/AlGaN MQWs and saw a significant red shift with increasing well width. Even though the non-polar sample showed a higher dislocation density, it proved to yield enhanced recombination efficiency as compared to the C-plane MQW structure. All these results are in very good agreement to what is expected theoretically from the influence of the QCSE.

3.3 Fabrication of GaN

Gallium nitride has been under investigation for many years, but has gained specifically large interest during the past 20 years mainly fueled by its commercial application prospects [140]. It was synthesized for the first time in 1932 [141] by passing ammonia over hot gallium and was referred to as "gallic nitride". The first chemical vapor deposition on a hexagonal sapphire substrate, to produce a large epitaxial layer of GaN was performed in 1969 by Maruska and Tietjen [81]. As the fabrication processes became more and more advanced the purity levels and crystal quality increased. However, the density of defects was still much larger than in other comparable semiconductor compounds like ZnSe and not much hope was given to this material. A major contribution to the success of GaN, showing the possibility of efficient GaN based LED devices, was made by Shuji Nakamura who developed bright blue [142] and green light emitting diodes and presented the first blue semiconductor laser based on GaN [140].

For the synthesis of GaN many deposition techniques have been applied, the most frequent ones now being hydride vapor phase epitaxy (HVPE), metalorganic vapor phase epitaxy (MOVPE), metalorganic chemical vapor deposition (MOCVD) and molecular beam epitaxy (MBE). The necessity of high N vapor pressures to assure the stoichiometric ratio for GaN growth, because of the low solubility of N in Ga, for a long time limited the quality and availability of bulk GaN. Clearly, the substrate for an epitaxial process is of fundamental importance to the success of high quality epitaxial layers (see section 3.3.1). The lack of bulk GaN substrates is therefore one of the main reasons for the difficulties in obtaining high quality GaN material and necessitated the use and investigation of alternative substrates for heteroepitaxial growth of GaN. A number of substrates have been tried and have been evaluated for growth of GaN (further details are given in section 3.3.1).

Note, that depending on the crystal orientation of GaN that is aimed to be grown; only specific crystal planes of different materials can be considered for epitaxial growth. The development of C-plane GaN has earlier roots than the non-polar or semi-polar orientations of GaN, due to its simpler production possibility, rising from the fact that C-plane GaN is the fastest growth direction and hence is the

crystal phase easiest obtainable, but also impacted by the availability and quality of hexagonal sapphire substrates for its growth.

Recently, triggered by the great demand, GaN templates and bulk substrates have become commercially available[2]. However, the price of these substrates for homoepitaxy is still approximately 100 times higher than for a substrate for heteroepitaxy. For example, a one sided epi-ready polished M-plane GaN substrate of 9×13 mm and thickness 350 ± 100 μm is sold for 2553 €[3], whereas a one sided epi-ready substrate of 10×10 mm and 0.5 mm thickness for M-plane GaN heteroepitaxy such as (100) $LiAlO_2$ costs 26.5 €[4].

Furthermore, larger wafer sizes (e.g. round 2 inch wafers) are only available for C-plane GaN. The reason being that other oriented GaN substrates are cut from C-plane oriented GaN and very thick GaN crystals are difficult to produce. Therefore, heteroepitaxy of GaN is still widely used and investigated and will exclusively be considered in this work.

Of course there are also other issues to be dealt with in the production of GaN, especially looking toward device realization. This is for example p-type doping of GaN, where Mg or Zn have been considered to provide acceptor levels. The incorporation of acceptor atoms is not the main obstacle, the difficulty arises from the low hole concentration and the large resistivity in p-type material. One problem towards low-resistivity p-type doping using Mg is the acceptor-compensation of holes by e.g. atomic hydrogen [144, 145]. This is especially critical if NH_3 is used in the growth of GaN as N supply (as is the case in e.g. MOCVD or ammonia-MBE also called RMBE). The usage of plasma-assisted MBE, which was used in the studies of this work, being a deposition method performed in an ultra high vacuum environment, has the advantage of lowering this effect to a minimum. Another difficulty, however, is the large activation energies of the dopants in GaN (the activation energies are even higher in AlN). The Mg related acceptor levels in GaN lie at $\sim$ 125 meV$-$170 meV [146–151] above the valance band, whereas for Zn the activation energy is even higher, being around 370 meV [152]. Still, there are ideas and concepts to overcome these issues such as modulation doping [153] or polarization-induced hole doping [154].

The idea of using N-polarity in C-plane GaN, as opposed to Ga-polarity, for a better incorporation of dopants has raised interest to overcome certain problems. For example, the above mentioned polarization-induced hole doping needs N-polarity GaN

[2]Examples of companies selling free standing bulk GaN are in Asia: Sumitomo, Nichia, Sony, Hitachi-cable and Mitsubishi Chemical; in Europe: LumiLOG, TopGaN and Ammono; in the US market mostly non- or semi-polar GaN is focused on by Kyma, Inlustra Technologies and Oxford Instruments (TDI) [143].

[3]Price inquiry on the 18. April 2011 at Ammono.

[4]Price inquiry on the 3. May 2010 at Crystec.

and the dissociation temperature is increased for N-polar InGaN [155]. However, crystal quality of such layers is inferior to the Ga-polarity grown films [123], due to a reduced adatom mobility on the N terminated face. Further, it has been shown that impurities, i.e. also dopants, are incorporated in higher abundance in semi- and non-polar films [120, 156].

While research is pushing limits on many frontiers, this work focuses on the task of finding promising substrates for a defect poor growth of GaN with a smooth surface. In the following section only the substrates used for non-polar GaN growth will be discussed. The short review of substrates will be followed by a description of the MBE process to grow GaN with special focus of the MBE machine used in this work.

3.3.1 Choice of substrate

For epitaxial growth processes the choice of a convenient and adequate substrate is a crucial task. The substrate influences properties of the epitaxial film such as defect densities, roughness of the film, ability of wetting, i.e. nucleation properties, but is also important with respect to further processing of the grown material. This means, that aspects such as conductivity, transparency or chemical, thermal and mechanical stability have to be considered. Therefore, a thorough investigation of the substrate is mandatory and a prerequisite to successful epitaxial growth of any given material.

A very important aspect with regard to the possibility of epitaxial growth and a desired low defect density of the grown film is a matching of the lattice constants and the coefficients of thermal expansion between the film and the substrate. Generally the lattice mismatch between the substrate and the growth material is considered as the main indicator of the feasibility of epitaxial growth. As a rule of thumb a low lattice mismatch should lead to little strain whereas a large lattice mismatch increases the induced strain and hence preferentially leads to misfit dislocations at the substrate - epitaxial layer interface. This in turn may lead to elongated defects in the crystal and to poor crystal quality. Hereby a differentiation has to be made between compressive and tensile strain. It has been stated that tensile strain leads to a cracking of the crystal while compressive strain is more likely to be relieved in crystal defects [5]. A cracking upon cooling of the sample from the growth temperature to room temperature may also be induced by a large mismatch of the coefficient of thermal expansion (CTE) of the substrate and the epitaxial layer.

The choice of a substrate is not merely dependent on its physical and chemical properties but also, as has been mentioned above, relies on the attainability of such material. Due to the high price and low abundance of GaN substrates for growth

of non-polar GaN, a lot of effort is invested in search of an adequate substrate for heteroepitaxy. Table 3.2 shows a compilation of selected substrates that have been considered for the epitaxial growth of non-polar GaN.

While extensive studies of substrates for C-plane GaN growth exist [157], the search for substrates for A- or M-plane GaN growth has only been triggered roughly 10 years ago by the publication of Waltereit et al. [139] where the authors experimentally showed the beneficial effects of avoiding the QCSE (see section 3.2) using M-plane GaN grown on γ-$LiAlO_2$. In the following only substrates for the growth of non-polar GaN shall be considered.

Non-native substrates usually lead to a considerable amount of extended defects, such as threading dislocations, stacking faults or inversion domain boundaries in the grown crystal. These defects produce scattering as well as non-radiative recombination centers, usually in form of states inside the bad gap thereby lowering the quantum efficiency. Evidently a reduction of defects is wanted and a lot of research is aimed at exactly this point.

The biggest drawback of non-polar GaN is the still much larger defect densities, compared to C-plane GaN [158]. Foremost the frequently occurring stacking faults, lying in the C-plane, pose a prominent defect in the non-polar film orientation [158, 159]. Various substrates and techniques have been investigated to reduce the defect density in the films, an important one being Epitaxial Lateral Over Growth (ELOG)[5]. This technique, allowing a significant reduction of the threading dislocation density from usually $10^8 - 10^{10}\text{cm}^{-2}$ to levels of 10^6cm^{-2} [5], however requires additional steps in the production process like patterning, making it more complex and expensive. In this study the ELOG technique was not applied, we therefore concentrate of the direct growth of GaN films.

Non-polar GaN growth has previously been attempted on substrates like R-plane sapphire [160, 161], SiC [162, 163] and γ-$LiAlO_2$ [164, 165]. Also GaN M-plane substrates have been considered in a few studies [166, 167], despite the extremely high cost and limited wafer sizes available. Some important aspects in the growth of non-polar GaN are to obtain phase purity, flat surfaces and a reduction of the defect density. Previous to this study non-polar GaN has not been reported on LGO. Due to the low lattice mismatch of the non-polar GaN planes to the appropriate LGO surfaces (see Table 3.2) low defect densities are expected. The investigation of MBE growth of GaN on LGO will be discussed in chapter 4.

[5]For the technique of epitaxial lateral overgrowth the acronyms ELO and LEO are also common.

Table 3.2: Substrates for the heteroepitaxial growth of non-polar GaN. In the table the abbreviation 'X'-GaN stands for the 'X'-plane of GaN and similarly for the other materials.

Substrate	**Crystal symmetry**	**Lattice constants** [Å]	**Epitaxial relationship to GaN**	**In-plane direction** GaN ∥ Substrate	**Lattice mismatch to GaN** [%]	**CTE** $[10^{-6}\,\mathrm{K}^{-1}]$
α-Al_2O_3	Hexagonal	$a = 4.7589$ [168]	A-GaN on R-Al_2O_3	$[1\bar{1}00] \parallel [11\bar{2}0]$	-1.85	$\alpha_a = 7.3$ [168]
	$R\bar{3}c$	$c = 12.991$		$[0001] \parallel [1\bar{1}01]$	1.19	$\alpha_c = 8.5$
			C-GaN on C-Al_2O_3	$[11\bar{2}0] \parallel [1\bar{1}00]$	16.07	
				$[10\bar{1}0] \parallel [11\bar{2}0]$		
γ-$LiAlO_2$	Tetragonal	$a = 5.1687$ [169]	M-GaN on (100) γ-$LiAlO_2$	$[1\bar{1}00] \parallel [010]$	1.76	$\alpha_a = 15$ [170]
	$P4_12_12$	$c = 6.2679$		$[0001] \parallel [001]$	0.34	$\alpha_c = 7.1$
			C-GaN on (100) γ-$LiAlO_2$	$[1\bar{1}00] \parallel [010]$	∼1.76	
β-$LiGaO_2$	Orthorhombic	$a = 5.402$ [171]	M-GaN on (100) β-$LiGaO_2$	$[11\bar{2}0] \parallel [010]$	0.09	$\alpha_a = 10.1$ [172]
	$Pna2_1$	$b = 6.372$		$[0001] \parallel [001]$	3.58	$\alpha_b = 21.1$
		$c = 5.007$	A-GaN on (010) β-$LiGaO_2$	$[1\bar{1}00] \parallel [100]$	2.25	$\alpha_c = 13.6$
				$[0001] \parallel [001]$	3.58	
			C-GaN on (001) β-$LiGaO_2$		∼0.19 [173]	
6H-SiC	Hexagonal	$a = 3.0806$ [168]	M-GaN on M-SiC	$[11\bar{2}0] \parallel [11\bar{2}0]$	3.52	$\alpha_a = 4.46$ [168]
	$P6_3mc$	$c = 15.1173$		$[0001] \parallel [0001]$	2.92	$\alpha_c = 4.16$
			A-GaN on A-SiC	$[1\bar{1}00] \parallel [1\bar{1}00]$	-10.35	
				$[0001] \parallel [0001]$	2.92	
			C-GaN on C-SiC	$[11\bar{2}0] \parallel [11\bar{2}0]$	3.52	

3.3.2 Molecular beam epitaxy and the system used in this work

The samples used in this work were all grown by Plasma-Assisted Molecular Beam Epitaxy (PAMBE). Hereby a generated flux of material (the molecular beam) is used to deposit atoms or molecules to form an over layer (epitaxy) on a substrate in a controlled fashion. When two or more fluxes of different materials are provided, they can react at the substrate and form a compound. The material is usually supplied through evaporation by heating a crucible in which the high purity material is placed. Gaseous elements on the other hand need not be evaporated but can be let into the growth chamber through a flow control unit. However, because the gaseous elements form strong binding molecules, like O_2 and N_2, it is purposeful to activate them with some energy, so they can more readily dissociate and take part in new compound formation, having reached the surface of the substrate. In plasma-assisted MBE this activation is done by creating a plasma of the desired gas inside a so-called plasma cell. Here, the molecules are excited before they are released into the growth chamber and directed at the substrate.

One of the requirements of a MBE process is the condition of an Ultra High Vacuum (UHV). For one, this is necessary to provide for the long mean free path of material from the material sources to the substrate and to minimize the incorporation of other elements in the sample from the surrounding. The incorporation of such defects is often referred to as unintentional doping. MBE is seen as a material deposition technique of samples with low impurity levels and a good control over composition and doping of the structure by simply blocking the material fluxes by rapid shutter operation. Intrinsic properties of the MBE process compared with other epitaxial methods like MOCVD or HVPE are the on average slower growth rate and the possibility of growing at lower temperatures. A lower growth rate is useful for producing very thin layers of material and allows for a precise control of structures. Low temperatures are of value when growing crystals which are instable at high temperatures, such as InAs and InN, when thermally driven diffusion of atoms from or into the surrounding layers is undesired, or when using substrates which are thermally unstable at high temperatures.

Because of the use of UHV conditions it is also possible to apply *in-situ* analysis such as Reflection High Energy Electron Diffraction (RHEED) in MBE, which is often stated as one of the big advantages over e.g. MOCVD. For RHEED, electrons with an energy of approximately 20 keV are diffracted at the sample surface under a small angle of incidence, e.g. 5°. The diffraction pattern is displayed on a fluorescent screen, where information of the crystal quality, growth mode and surface reconstructions can be extracted [174]. While growth of e.g. GaAs is usually conducted in As rich conditions, i.e. limited by the supply of Ga, nitride growth needs slightly Ga rich conditions, meaning an excess of Ga, usually in form of about two mono layers of liquid Ga floating on the sample surface [175], to produce flat

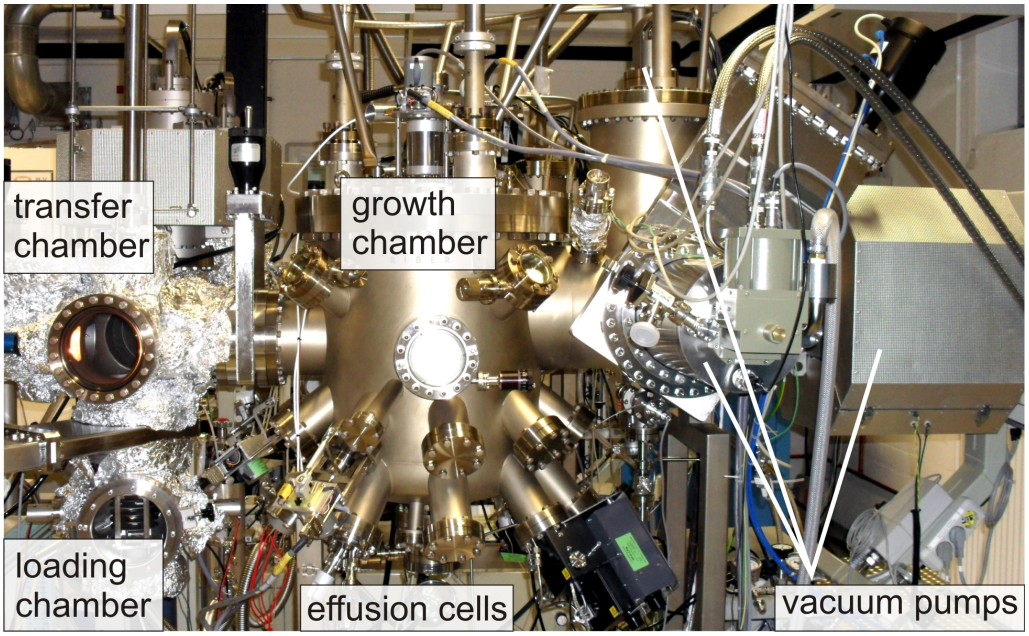

Figure 3.4: Picture of the MBE machine used in this experimental study.

and smooth surfaces. This situation explains why RHEED oscillations cannot be observed in nitride (as opposed to arsenide) growth for the determination of growth rates. RHEED oscillations are intensity variations of the diffracted electron RHEED beam as a function of the formation of new atomic layers on the sample surface. Nevertheless, in nitride growth, RHEED diffraction patterns are of great help when evaluating the surface roughness, the crystal direction and lattice constants and the approximate Ga coverage of the sample.

Description of the MBE system used in this work The specific MBE chamber used in this work is a RIBER Compact 21T MBE machine situated in the clean room of the Center for Functional Nanostructures at the Karlsruhe Institute of Technology. It is part of an MBE cluster of 2 systems connected by a tunnel; one mainly dedicated to the growth of III-V arsenides, the other one assigned to the growth of nitride semiconductors. The following description will only consider the latter of the two systems. Fig. 3.4 shows a photograph of the MBE system used in this study.

My work on this MBE machine started with building up the "nitride" system. This included installation of the components described below, like e.g. the effusion and plasma cells, transfer rods, mass spectrometer, RHEED setup, loading chamber, cryogenic vacuum pump and the electrical rack with all the surveillance and con-

trol units like for instance the temperature and shutter controls for the cells and substrate. After all necessary components had been attached to the system, the required stable vacuum attained, the cells filled with material, the Proportional-Integral-Derivative (PID) control values of the temperature controllers adjusted, the MBE control software[6] installed and a complete bake-out of the system performed, the experimental setup was ready for first growth runs and commissioning experiments were conducted. The well known substrate of γ-$LiAlO_2$ for non-polar GaN growth [13] was chosen for growth condition and parameter optimization, which will be shortly sketched in chapter 4 before presenting the results on the new substrate $LiGaO_2$. Before reverting to the actual growth of nitrides, in the following last part of this chapter, the MBE system dedicated to III-nitride growth will be described.

The main body of the MBE machine consists of three chambers: a loading chamber, a growth chamber and a transfer chamber to avoid direct contact between the loading chamber (often subject to air exposure) and the growth chamber. The three chambers are connected via vacuum tight shutters.

The loading chamber represents the system's connection to the surrounding environment. It is subject to frequent exposure to air when samples are taken out or new substrates are introduced into the vacuum. When opening the loading chamber, the cavity is constantly flooded with pure nitrogen to lessen contamination from air. The chamber is pumped by a turbo molecular pump connected to a scroll fore pump. The pressure is measured by a compact full range pressure gauge, consisting of a Pirani and cold cathode ionization gauge. This chamber is also used as a first desiccation and outgasing station for newly introduced material. For this purpose 2 baking lamps are installed and controlled via a PID controller, connected to a thermocouple in the vacuum and a power supply, for smooth temperature control inside the chamber. The pressure generally reaches approx. 10^9 mbar after the outgasing step (usually performed at 130 °C for 60 min).

The transfer chamber is pumped by a Ti ion getter and Ti sublimation pump leading to a pressure of about 10^{11} mbar, as measured by an ionization pressure gauge. Two transfer rods magnetically and almost frictionless supported are attached to this chamber, to provide for the horizontal and vertical manipulation of the samples from one chamber to the next. For the transport of samples, only one shutter at a time is opened to avoid direct contact between the loading and growth volumes.

The growth chamber is pumped by basically four vacuum pumps including a Ti ion getter pump, a Ti sublimation pump, a He cryogenic pump operating between 12 K and 14 K and a liquid nitrogen cryopanel surrounding the entire epitaxy volume. A constant cooling of the cryopanel shield is assured by a liquid nitrogen (LN2) bath located above the chamber, supplying the MBE machine constantly with LN2

[6]Customized written program by Dr. Daniel Schaadt.

via vacuum isolated pipes. The average background pressure in the growth chamber, measured by an ionization gauge of the Bayard-Alpert type, is approximately 10^{-10} mbar. A mass spectrometer (Pfeiffer Vacuum Prisma 80, QMS 200) is inserted in the chamber for vacuum analysis and leakage detection. *In-situ* growth analysis is performed by RHEED measurements using the electron gun and fluorescent screen installed in the system. A camera is installed in front of the RHEED screen to view and document diffraction patterns of samples.

The sources attached to the MBE system contain In, Al, Ga, Cu, Si, N_2 and Mg or Zn. Their spatial order in the chamber can be seen in the schematic drawing in Fig. 3.5. The solid sources are placed in PBN crucibles mounted in standard effusion cells equipped with thermocouple elements. For temperature monitoring and control the cells are connected to PID controllers (Eurotherm 2408) which in turn give the appropriate signals to the power supplies of each cell. Each of these cells is equipped by its own shutter to block the molecular beam from the cell. The N_2 supply is managed via a gas flow control unit positioned in front of a water cooled Oxford HD25 RF radio frequency plasma source. Deflection plates operating at a voltage of 600 V are fixed at the output of the plasma cell to divert highly energetic ions generated in the plasma. This is done to prevent the energetic ions from reaching the sample surface thereby risking damaging it.

Substrate sizes of up to 2 inch circular wafers can be processed in this MBE system. The substrate is placed on a Molybdenum holder which, when introduced to the growth chamber is placed in a substrate manipulator with the sample surface oriented downward. The substrate manipulator can be continuously rotated to provide for a uniform deposition of the material and heated up to a maximum temperature of 1000 °C; the heating is also managed via a PID controller. In order to simultaneously cut off or start a growth process involving several sources, a shutter is installed directly below the substrate manipulator.

A way to get an idea of the amount of material provided for sample growth is to measure the Beam Equivalent Pressure (BEP) of the molecular or atomic beams coming from the source. This measurement is done by an ionization gauge which is placed just underneath the substrate shutter by a manipulator arm when measuring. During growth, this gauge is retracted to a position inside one of the flanges. The pressure indicated by the gauge is a measure for the amount of provided flux of the specific material. It can be used to reproduce growth conditions more reliably. Another measure for the reestablishment of earlier growth conditions is the cell temperature. However, depending on the material content of the cell, the flux may vary at a constant cell temperature.

Electronic units in the system are connected to a computer for supervision and control of the growth parameters, such as pressure monitoring, vacuum analysis, camera for the RHEED observation and temperature and shutter control of the

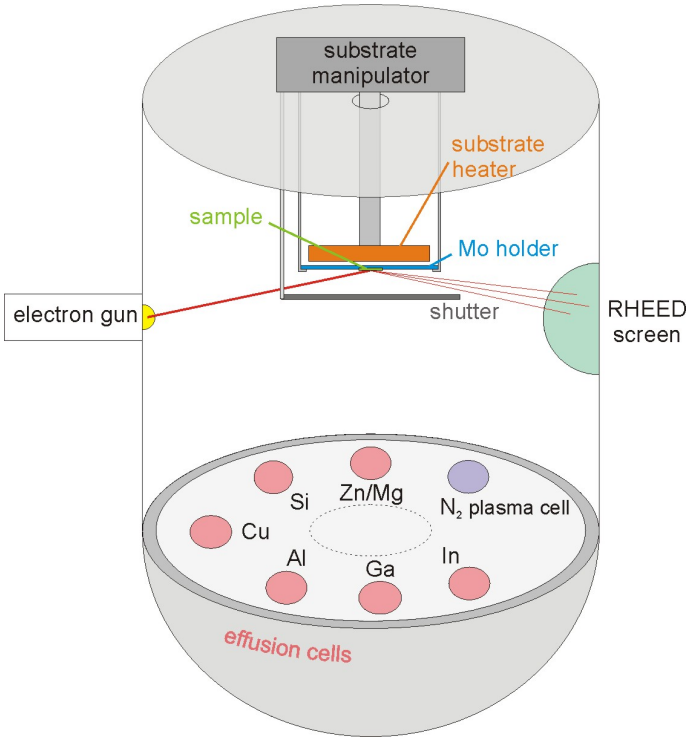

Figure 3.5: Schematic of the arrangement inside the growth chamber of the MBE used in this work. For reasons of clarity, the vacuum pumps, BEP pressure gauge, mass spectrometer as well as the flanges and windows were omitted.

cells and the substrate heater. The system is attached to an emergency power grid backed up with a number of uninterruptible power supply (UPS) units.

4 Non-polar GaN films

Non-polar GaN is used as a description referring to the absence of electric fields running along the growth direction of the material. This directs a way to avoid the Quantum Confined Stark Effect and all its associated constraints, as described in section 3.2. The current chapter is dedicated to the investigation of the growth of non-polar GaN films on different substrates and substrate orientations by plasma-assisted molecular beam epitaxy. These are (100) γ-$LiAlO_2$, (100) β-$LiGaO_2$ and (010) β-$LiGaO_2$. In the first part of this chapter (sec. 4.1), in order to commission the newly built MBE system, the results of growth on γ-$LiAlO_2$, a substrate known to yield M-plane GaN [176], are displayed. Subsequently, GaN growth and growth results on the new substrate β-$LiGaO_2$ are presented (sec. 4.2).

4.1 Growth of M-plane GaN on (100) γ-$LiAlO_2$

To find appropriate growth conditions and parameters for GaN growth, M-plane GaN was grown on (100) γ-$LiAlO_2$ (LAO) in the newly installed MBE system. The aim was to obtain flat surface morphology of GaN layers with good crystal quality. A short characterization of the substrate in the next section (4.1.1) will be followed by the description of growth parameter optimization (section 4.1.2).

4.1.1 Properties of the substrate γ-$LiAlO_2$

Interestingly, the first study of GaN growth on (100) LAO resulted in polar C-plane GaN films [177]. Later, however, it was shown that, if the growth parameters were tuned, M-plane GaN films could be grown on (100) LAO [164, 176, 178–180]. The crystal structure of LAO was determined to be $P4_12_12$ with lattice constants $a = 5.1687$ and $c = 6.2679$ [169]. The LAO crystal is completely transparent in the wavelength range between 200 nm and 4 μm, its melting point is around 1700 °C and it can be grown by the Czochralski technique [170], i.e. large crystals can be pulled out of a melt using a seed crystal [181]. Despite its relatively high melting point the crystal has been reported to decompose already at temperatures above 900 °C [182]. The fact that LAO is etched by a number of acids [183] has been

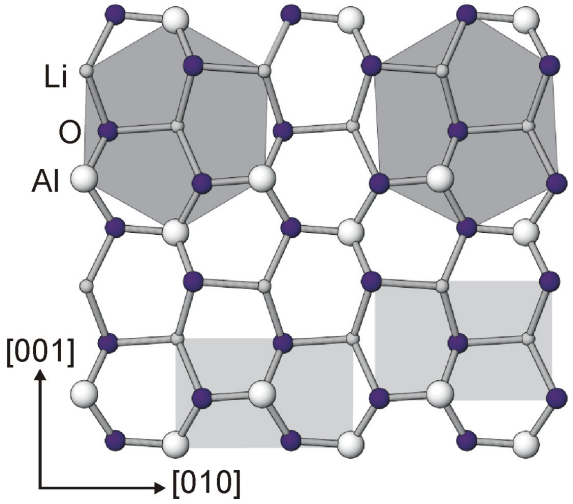

Figure 4.1: Ball and stick model of the (100) $LiAlO_2$ substrate surface. The shaded areas indicate possible nucleation sites for C- and M-plane GaN. From [135].

used to obtain a free standing GaN substrate by GaN growth on (100) LAO and subsequent removal of the LAO by etching [166]. The (100) face of LAO exhibits a certain polarity, i.e. two different qualities of GaN have been found to grow on this substrate [164]. This is discussed in detail in [135, 164].

The lattice match of GaN and LAO make both C- and M-plane GaN growth possible on (100) LAO (see Table 3.2) as illustrated in Fig. 4.1 where the (100) LAO surface and possible sites for C- and M-plane GaN growth are depicted schematically. The simultaneous growth of M- and C-plane GaN on (100) LAO has also been observed in the present study and poses an issue when aiming at high purity of a single GaN phase [184–186].

4.1.2 Growth parameter optimization for M-plane GaN growth on (100) γ-$LiAlO_2$

For epitaxial growth of nitrides there are a manifold of growth conditions that influence the crystal quality of the epitaxial layer. Some examples are the substrate temperature, the provided metal to nitrogen ratio, the growth time, the nitrogen plasma power, the substrate morphology, pre-growth treatment of the substrate, like annealing, nitridation[1] and wet-chemical cleaning or etching.

[1]Nitridation is a term used to describe the exposure of the substrate to activated nitrogen at elevated temperatures. This procedure is widely used for nitride growth on sapphire substrates [187, 188].

In the following, the tuning of one of these parameters, namely the influence of the substrate temperature, will be exemplified. Thereafter, some samples grown at optimized growth conditions will be presented.

Prior to growth, the LAO substrates were typically cleaned by subsequently dipping the substrates into Trichloroethylene (TCE), Acetone and Methanol for one minute and rinsed for ten seconds with deionized water. Thereafter they were blow dried with nitrogen, attached to a Si wafer with indium, placed into a molybdenum holder and introduced into the MBE machine. The Si wafer's function is to enhance the heat absorption of the substrate heater during growth; Indium is used to provide for a homogeneous temperature coupling. Once injected into the MBE system, the substrates were outgased at 130 °C for 60 min and then transferred into the growth chamber.

Influence of the substrate growth temperature To see the impact of the substrate temperature on the surface morphology of the GaN layers, the substrate temperature was tuned from 600 °C to 800 °C, thereby leaving all other parameters constant. All temperature values given for the substrate temperature in this work correspond to the thermocouple reading of the thermoelement attached to the substrate heater. The actual temperature of the sample is therefore lower by approximately 30 °C to 50 °C [2]. Fig. 4.3 displays a series of samples which were grown with a constant N_2 flux of 0.3 sccm at a plasma forward power of 450 W and a gallium cell temperature of 930 °C[3] for 20 min. After growth, the samples were left at 900 °C for 5 min to evaporate remnant Ga from the surface.

As can be seen on the Scanning Electron Microscopy (SEM) images in Fig. 4.3, a mixture of columnar hexagonal C-plane crystals and M-plane islands are visible at a low substrate temperature whereas the surface morphology develops into a higher purity M-plane film around temperatures between 625 °C and 700 °C. This development of morphology change probably results from a higher surface mobility and longer mean free length of path of adatoms on the sample, before getting incorporated into the film at higher temperatures, hence leading to a more uniform material distribution. At high temperatures (Fig. 4.3 (d) and (e)) however, other effects come to play. This can be a faster evaporation rate of atoms from the sample surface leading to a changed Ga/N ratio, resulting in a change of the growth conditions from

[2] An internal calibration can be attained by observing the 7×7 surface reconstruction in RHEED patterns of a (111) Si substrate, which appears around 1100 ± 15 K [189], i.e. at ∼827 °C.

[3] The Ga cell has two filaments for heating the Ga filled crucible, which can be controlled separately, one at the base of the cell (body) and one closer to the crucible exit (tip). In this study the temperature difference between body and tip was always 50 °C. In this thesis only the higher tip temperature value will be given.

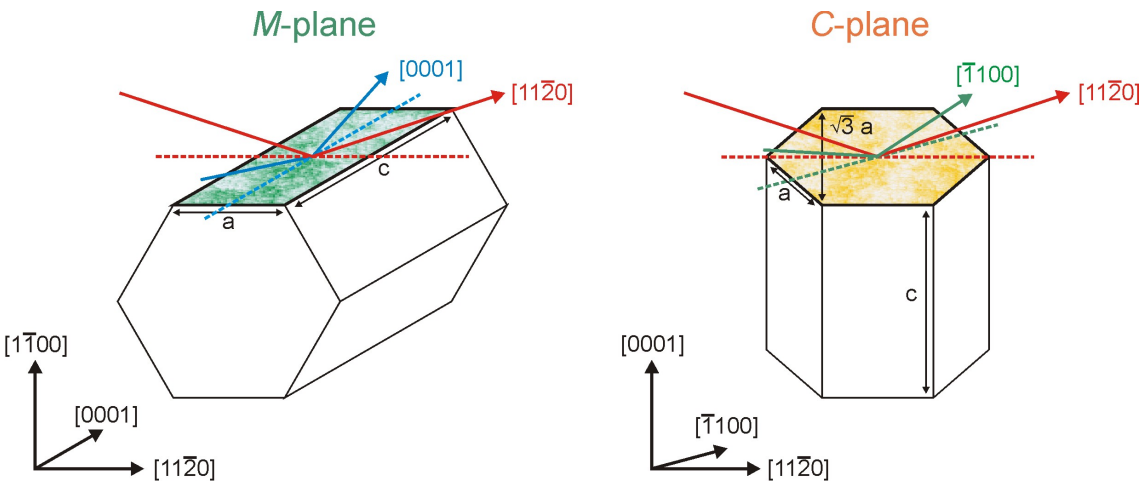

Figure 4.2: Schematic illustration of the main RHEED azimuths that can be seen in *M*- and *C*-plane GaN. RHEED measurements are sensitive to the reciprocal value of the lattice spacing perpendicular to the electron beam direction.

gallium to nitrogen rich. At a substrate temperature T_{Sub} = 750 °C *M*-plane islands appear again surrounded with *C*-plane oriented GaN. The high amount of *C*-plane GaN grown at substrate temperatures can be seen in the RHEED pictures, which show the typical two [1$\bar{1}$00] and [11$\bar{2}$0] azimuths observed on *C*-plane GaN. To illustrate the RHEED observations, Fig. 4.2 shows the main azimuths that can be seen on *M*- and *C*-plane GaN schematically. The spacing of the streaks on the RHEED screen is proportional to the reciprocal value of the lattice constants of the crystal perpendicular to the RHEED beam direction. Note that the [11$\bar{2}$0] azimuth corresponds to different distances, depending on the crystal growth direction. The *M*-plane GaN vanishes completely at T_{Sub} = 800 °C and the RHEED pattern shows clear and bright diffraction off a *C*-plane GaN surface.

The lower SEM pictures in Fig. 4.3 (b) and (c) show an admixture of the *C*-plane orientation in form of small hexagonal crystal shapes, which preferentially nucleate at cracks or inhomogeneties in the film. By fine tuning the growth parameters it is aimed to completely get rid of these *C*-plane inclusions. Indeed, none of such *C*-plane crystallites can be seen in the samples shown in Fig. 4.3 (d) and (e). Moreover, the *M*-plane layers in Fig. 4.3 (b), (c) and (e) show cracks in the layer surface, which are possibly due to the suboptimal Ga/N ratio at this substrate temperature and the short growth time used in this sample series[4]. The rough circular areas that can be seen throughout the SEM images of Fig. 4.3 are so-called footprints

[4]Film quality has been observed to be influenced by the GaN layer thickness [165], i.e. the growth time.

Table 4.1: Table of rms roughness determined by AFM for M-plane GaN samples (seen in Fig. 4.3 (b)-(e)) grown on γ-$LiAlO_2$ at different substrate temperatures. The flattest surface morphology is achieved for $T_{Sub} = 675$ °C.

Growth temperature [°C]	**rms for an area of** 10×10 μ**m**^{2} **[nm]**	**rms for an area of** 5×5 μ**m**^{2} **[nm]**
625	10.9	8.0
650	8.6	6.1
675	5.3	3.5
700	8.6	7.1

of Ga droplets present on the sample surface during growth. A reduction of these features is wanted, however, somewhat difficult to achieve. However, the roughness is significantly improved in the case of $T_{Sub} = 675$ °C (Fig. 4.3 (d)) compared to the samples grown at other temperatures. This is also reflected in the root mean square (rms) roughness values obtained by Atomic Force Microscopy (AFM) for an area of 10×10 μm^2 listed in Table 4.1.

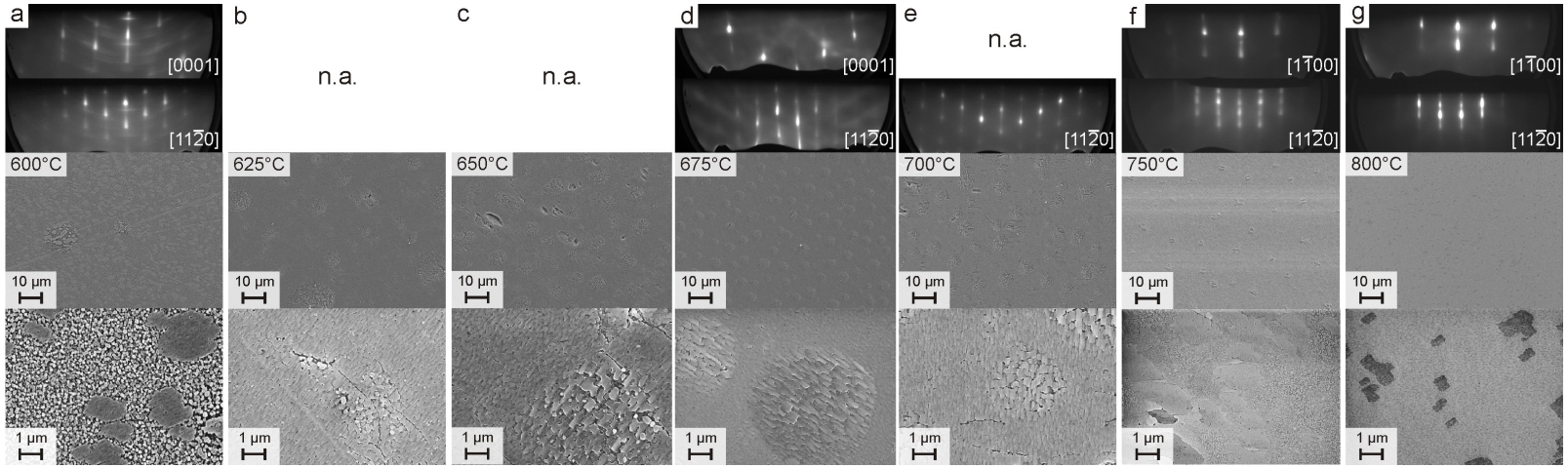

Figure 4.3: SEM and RHEED images of various samples grown at different substrate temperatures of 600 °C (a), 625 °C (b), 650 °C (c), 675 °C (d), 700 °C (e), 750 °C (f) and 800 °C (g). A growth window for M-plane GaN can be seen for temperatures around 625 °C to 700 °C while at lower and higher temperatures the C-plane fraction of GaN is large. The film orientation can be inferred from the RHEED pictures.

GaN samples grown on (100) γ-$LiAlO_2$ using optimized growth conditions By tuning the various growth parameters smooth M- and C-plane GaN samples were grown on (100) LAO. The results can be seen in Fig. 4.4 and Fig. 4.5. A narrow rocking curve full width at half maximum (FWHM) states a high crystal quality with a narrow distribution of tilt to the main crystal orientation. Streaky RHEED patterns are an indication of a flat surface and can be seen in both the M- and C-plane GaN films.

The M-plane GaN sample of Fig. 4.4 was grown at a substrate temperature of 725 °C for 120 min, resulting in a thickness of roughly 200 nm (measured by SEM). The Ga cell temperature was $T_{Ga} = 931°C$ and the nitrogen plasma cell operated at 450 W with a nitrogen flux of 0.3 sccm resulting in a BEP Ga/N ratio of approx. 5.7.

The typical slate like morphology of the M-plane orientation is shown in the SEM image of Fig. 4.4. The surface is essentially closed and shows no cracks or C-plane inclusions. In the lower magnification SEM image, on the left side, Ga droplets are visible on the surface. Two RHEED azimuths at the top of Fig. 4.4 display the reciprocal lattice spacing of the a_{Ga} (left) and c_{Ga} (right). From the streakiness of the patterns a flat surface is expected; the [0001] azimuth, however, shows discontinuities in the streaks, which points toward a three dimensional modulation of the surface, i.e. the presence of droplets.

X-ray diffraction (XRD) performed on the sample confirms the high M-plane phase purity of the sample as the $\omega-2\theta$ scan (left side in Fig. 4.4) only displays the presence of the $(1\bar{1}00)$ GaN and (200) LAO oriented planes at $\omega = 16.14°$ and $\omega = 17.34°$, respectively, and no indication of the (0002) GaN reflection usually found near $\omega = 17.28°$ can be seen. The right XRD scan in Fig. 4.4 depicts a rocking curve scan across the $(1\bar{1}00)$ GaN reflection and reveals a FWHM of about 817 arcsec, which is a good value; comparable to or smaller than results reported in literature for M-plane GaN growth on LAO [139, 164, 165, 190–192].

RHEED, SEM and XRD data of a C-plane GaN sample is depicted in Fig. 4.5. By growing at a nominal substrate temperature of 725 °C for 60 min a 90 nm (measured by SEM) thick GaN film was obtained. In this case the substrate was mounted onto the Si wafer in a different way compared to the M-plane sample described above, so that a better thermal coupling of the Si to the substrate and hence a higher substrate temperature can be assumed. The other growth parameters were left unchanged, so that $T_{Ga} = 931°C$, the nitrogen plasma cell was operated at 450 W with a nitrogen flux of 0.3 sccm.

From the RHEED pictures, displayed at the top of Fig. 4.5, the dominant crystal orientation can already be deduced, as the distances between the visible streaks correspond to the reciprocal values of a_{Ga} for the $[1\bar{1}00]$ and $\sqrt{3}a_{Ga}$ for the $[11\bar{2}0]$ azimuth. The diffraction patterns are streaky and hence indicate a flat surface

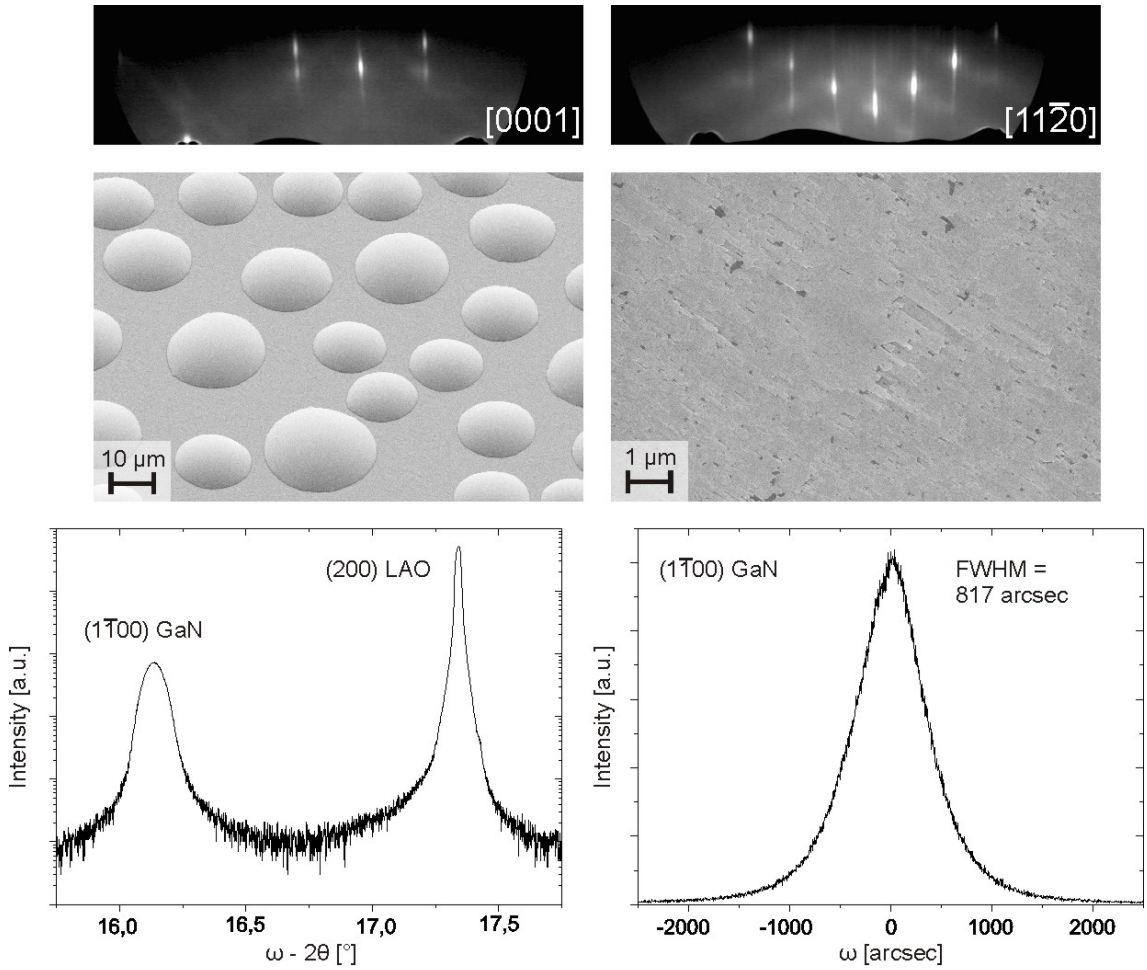

Figure 4.4: This figure displays RHEED, SEM and XRD results obtained for a 200 nm thick M-plane GaN film grown on (100) LAO. The top two pictures display streaky electron diffraction patterns of the M-plane GaN surface in two directions, [0001] and [11$\bar{2}$0], indicating a smooth surface. The SEM images, taken at two different magnifications show the typical M-plane surface modulation and the presence of Ga droplets on the film. The lower two graphs, displaying XRD results, show the high phase purity in the $\omega - 2\theta$ scan (left) by a strong (1$\bar{1}$00) GaN and no reflection of the (0002) GaN plane and a low FWHM value of 817 arcsec; a good value for M-plane GaN growth on (100) LAO.

morphology. This observation can again be made in the SEM pictures in Fig. 4.5 where, in contrast to the M-plane film, hexagonally shaped crystallites can be seen in areas where the GaN film is not fully coalesced. The size of the Ga droplets present on the sample surface and visible in the lower magnified SEM image is smaller than on the M-plane GaN, supporting the conclusion of a higher substrate temperature in this case.

The x-ray diffraction measurements, depicted at the bottom of Fig. 4.5 clearly confirm the dominating C-plane orientation of the GaN film. Three peaks are visible in the $\omega - 2\theta$ scan which, from the left to the right, are identified to origin from the $(1\bar{1}00)$ GaN, (0002) GaN and (200) LAO planes. Although the existence of M-plane GaN is proven in film by this measurement, it is only present to a very small fraction as can be concluded from the intensity ratios of the attributed C-plane and M-plane peaks, which is 4000/100, meaning an admixture of roughly 2.5% of$M$-plane GaN in the otherwise C-plane oriented film. The inset in the left XRD graph shows an $\omega - 2\theta$ scan performed with a triple crystal analyzer to achieve a higher resolution at the cost of a lower intensity. The scan shows the clearly separated double peak of the (0002) GaN and (200) LAO planes at $\omega = 17.25°$ and $\omega = 17.34°$, respectively. The right part of XRD data in Fig. 4.5 depicts the rocking curve of the (0002) GaN peak taken in the triple crystal analyzer configuration and exhibits a FWHM of 1946 arcsec. This is a rather large value for C-plane GaN indicating fair crystalline quality of the film. Using other growth methods, like MOVPE and HVPE, where much thicker GaN films are grown (on the order of 200 μm), reported (0002) GaN FWHM rocking curve values in literature are 2200 arcsec [193], 1400 arcsec [194], 1270 arcsec [195] and with thorough growth optimization <400 arcsec [196]. However, C-plane GaN growth on (100) LAO by MBE has only been reported once giving a FWHM of the (0002) GaN reflection of 2700 arcsec [177] which is significantly higher than the one shown in Fig. 4.5.

4.1.3 Summary of GaN grown on γ-$LiAlO_2$

Observation of very high phase purity, a smooth surface and low FWHM values of M-plane GaN films on LAO were accompanied by the presence of Ga droplets. If evaporated or etched, these Ga droplets leave a rougher surface behind than the adjacent film that was not covered by Ga. It was difficult to obtain high phase purity, high crystal quality and a smooth surface without Ga droplets.

The results obtained for M-plane GaN on LAO are similar to previously reported investigations. The surface morphology and FWHM values of the XRD rocking curves are comparable to reports in literature.

For high quality GaN C-plane epitaxial layers grown heteroepitaxially, substrates like for example (001) $LiGaO_2$ and mainly hexagonal sapphire substrates are used.

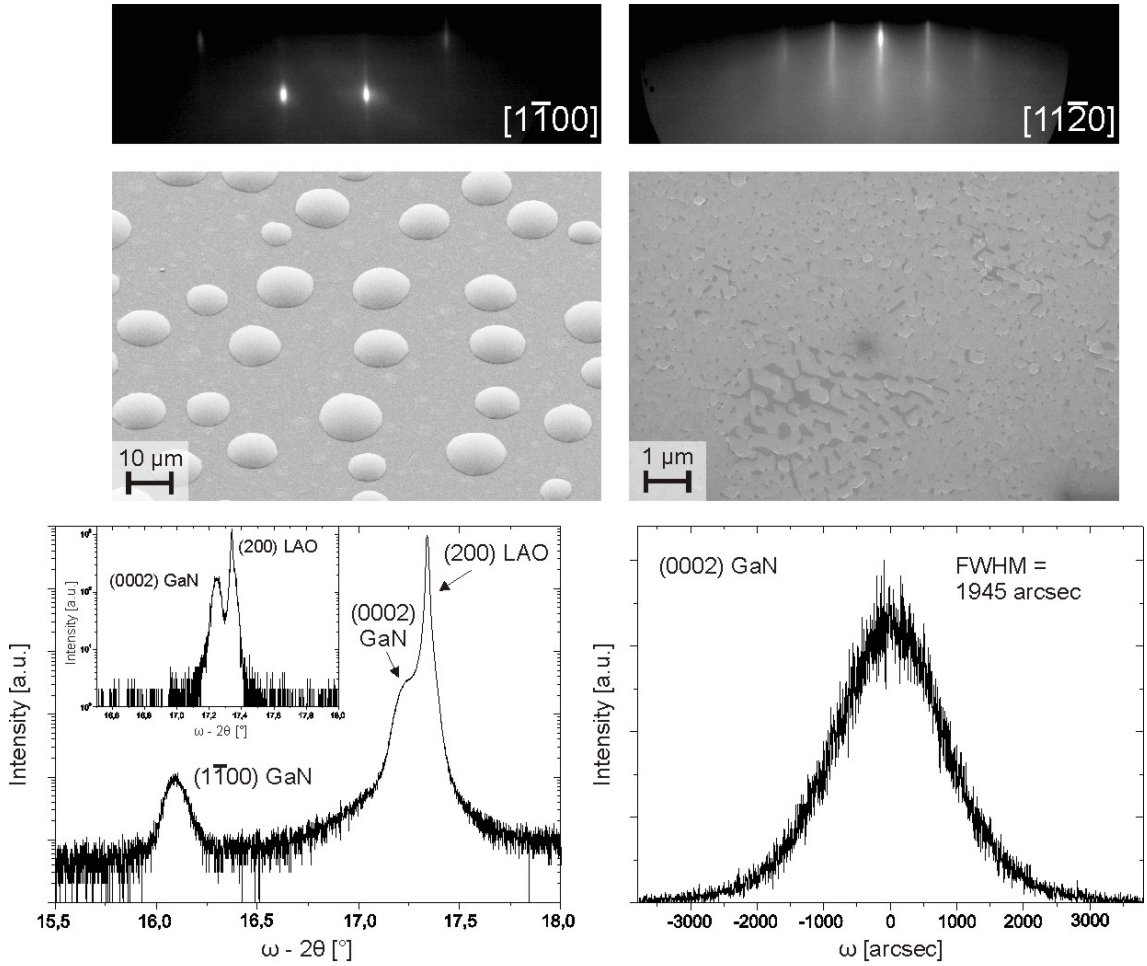

Figure 4.5: The RHEED, SEM and XRD results obtained for a 90 nm thick *C*-plane GaN film grown on (100) LAO. The top two RHEED pictures show streaky *C*-plane azimuths of GaN, indicating a smooth surface. SEM images of two different magnifications show hexagonal *C*-plane structures and the presence of Ga droplets on the film. The XRD graphs in the lower part of the figure show the presence of both *C*- and *M*-plane GaN in the sample. However, the *M*-plane fraction amounts to only about 2.5%. The rocking curve of the (0002) GaN reflection, shown in the lower right part, has a FWHM of 1946 arcsec.

Rocking curve FWHM values of the (0002) GaN reflection on (001) $LiGaO_2$ are reported around 100-300 arcsec [193, 197], the best value being 41.7 arcsec [193], and for GaN grown on sapphire below 100 arcsec, e.g. 51 arcsec in [198]. However, C-plane GaN on (100) LAO has only been reported few times [177, 193, 195, 196] and the crystal quality achieved in this study is close to the majority of the reported ones and better than the GaN films also synthesized by MBE.

After the influences of a number of growth parameters on the behavior of GaN growth in the newly commissioned MBE machine had been investigated and growth of GaN had been established and understood on LAO, growth of GaN on the new substrate LGO could proceed. This is described in detail in the next chapter.

4.2 Growth of non-polar GaN on β-$LiGaO_2$

The process of sample preparation, growth and characterization of non-polar GaN films on LGO is described in this section. It starts off with important properties of the substrate used in this study (sec. 4.2.1). Thereafter, a brief report on the fabrication of the substrates (sec. 4.2.2) is given, followed by a description of the growth procedures leading to non-polar GaN thin films on (100) $LiGaO_2$ and (010) $LiGaO_2$ with a presentation of their characterization results in sections 4.2.3 and 4.2.4, respectively.

4.2.1 Properties of the substrate β-$LiGaO_2$

Large wafer sizes of the $LiGaO_2$ substrate can be achieved by the Czochralski growth method [199]. The structure of $LiGaO_2$ was determined as orthorhombic, space group $Pna2_1$ (#33), with lattice parameters $a = 5.402$ Å$, b = 6.372$ Å$, c = 5.007$ Å [171]. While the (001) face shows hexagonal atomic arrangement, the (100) and (010) faces are atomically ordered in a rectangular fashion. Examination of the possible epitaxial relationships of GaN on LGO leads to the conclusion that closely lattice matched relations between LGO and GaN are found for M-plane GaN on (100) LGO[5], A-plane GaN on (010) LGO [6] and C-plane on (001) LGO[7] [173, 200]. This makes LGO a unique substrate for growth of the three prominent GaN crystal orientations [0001],$[1\bar{1}00]$ and $[11\bar{2}0]$, depending on the LGO surface orientation.

Because of the low lattice mismatch between LGO and GaN, this substrate received attention and was investigated for the heteroepitaxy of GaN, as an alternative to

[5]lattice mismatch $[010]_{LGO}\|[11\bar{2}0]_{GaN}$: 0.07% and $[001]_{LGO}\|[0001]_{GaN}$: 3.58%

[6]lattice mismatch $[100]_{LGO}\|[1\bar{1}00]_{GaN}$: 2.22% and [001] $_{LGO}\|[0001]_{GaN}$: 3.58%

[7]average lattice mismatch 0.9%

Table 4.2: The average linear coefficients of thermal expansion of $LiGaO_2$. After [157].

Reference	**Temperature range** [K]	$\alpha_{[100]}$ [$\times 10^{-6}$ K]	$\alpha_{[010]}$ [$\times 10^{-6}$ K]	$\alpha_{[001]}$ [$\times 10^{-6}$ K]
Nanamatsu et al. [215]	293 - 473	6	9	7
Neumann et al. [216]	293 - 1113	n.a.	n.a.	n.a.
	293 - 473	12.6	15.7	7.5
Ishii et al. [217]	293 - 1073	1.7	11.0	4.0
Rawn and Chaudhuri [172]	293 - 1423	10.1 ± 0.2	21.1 ± 0.3	13.6 ± 0.2
	293 - 473	7.0 ± 0.3	15.6 ± 0.4	10.7 ± 0.1

sapphire[8], already in the second half of the 1990's by MOCVD [201, 202], MBE [200, 203–208], MOVPE [209, 210], HVPE [211], PLD [212, 213] and by reaction with ammonia at elevated temperature [214]. However, all of these studies were conducted on (001) LGO aiming to improve the crystal quality of *C*-plane GaN. Before this present study, there has been no report about GaN growth on either of the other orientations of LGO. The growth of *M*-plane GaN on (100) LGO and *A*-plane GaN on (010) LGO by PAMBE will be shown in section 4.2.3 and 4.2.4, respectively.

The melting point of $LiGaO_2$ lies approximately at 1570 °C -1585 °C [5, 157, 215] making it in principle suitable for growth at high temperature. However, it has been reported that the substrate surface deteriorates when heated to temperatures above 800 °C [200] and secondary phases appear at temperatures around 1173 °C [172]. There is an uncertainty on the data on LGO's coefficients of thermal expansion reported in literature, yet all the data show a large anisotropy of the thermal expansion. This may pose some difficulty in growth of thick crack free layers on top of LGO. Table 4.2 gives a compilation of results obtained by different groups determining the average linear CTE of LGO. In addition it was found that the CTE depend quite strongly on the temperature [172, 216] and a comparison of the linear CTE is only approximately legitimate in the lower temperature range. In section 4.2.3 the thermally induced strain into the GaN film is evaluated.

LGO is hydrolytic, i.e. it dissolves in water, and is easily etched by solutions with different pH [5, 157]. Doolittle et al. [218] showed, that an entire LGO substrate could be etched away in less than 5 min in a base solution leaving the GaN layer unharmed. This led to the demonstration of removing the substrate and transferring the GaN film onto a GaAs substrate. The complete removal of the substrate could also be used to attain free standing GaN, which would be a great benefit for various

[8] lattice mismatch hexagonal sapphire to *C*-plane GaN: ∼13.9% [157]

applications. However, there is also a downside to the chemical instability of LGO, because polishing the substrate is difficult, leading to the necessity of finding an adequate substrate pretreatment for smooth surfaces.

The band gap of LGO is at 5.6 eV [203], corresponding to a wavelength of ∼221 nm. It is transparent approximately from its band gap up to 6 μm [5], meaning the material of LGO is transparent in the whole optical and a large fraction of the infrared spectrum of electromagnetic waves. This fact requires some thought of how to heat the substrate to a specific temperature for growth.

4.2.2 Growth of β-$LiGaO_2$

The LGO bulk crystal was grown at the National Sun Yat-sen University in Taiwan then cut and polished by a commercial vendor. The crystal growth was carried out in a Czochralski pulling furnace. The starting raw materials (Li_2CO_3 and Ga_2O_3 powders with a purity of at least 99.99%) were mixed mechanically according to 99.99% stoichiometric ratio. After placing the raw materials in an iridium crucible covered with an iridium lid to reduce the temperature gradient, the crucible was heated to approximately 1650 °C to melt the raw materials. During growth, nitrogen gas was continuously supplied to prevent the oxidation of the Ir crucible. The seed had a (001) c-axis orientation. A rotation rate of 10-20 rpm was used to control the growth conditions. Because of the high vapor pressure of the LGO melt, a high crystal pulling rate of 2-4 mm/h was applied in order to avoid loss of the melt. Due to difficulties in obtaining transmission electron microscopy images on these types of substrates, owing to the rapid destruction of LGO under highly energetic electron irradiation, only limited structural information has been obtained so far. The crystal of which the substrates used in this work were cut from showed a small inclusion at the bottom of the crystal. No twin boundaries were found and a dislocation density of about 10^4∼10^5 cm^{-3} was estimated [219].

The substrates were cut in two different orientations. One set had a surface orientation of (100) while another set was cut parallel to (010). In the following the growth of M-plane GaN on (100) LGO (section 4.2.3) and A-plane GaN growth on (010) LGO (section 4.2.4) will be presented. Each of these sections is divided in two parts; the first part is concerned with the actual growth of the films and the second part with the characterization of the GaN films that have been grown.

4.2.3 Growth of M-plane GaN on (100) β-$LiGaO_2$

Figure 4.6 shows a ball and stick model of the (100) LGO surface with its unit cell as a dotted rectangle. The gray rectangles display possible nucleation sites for M-plane

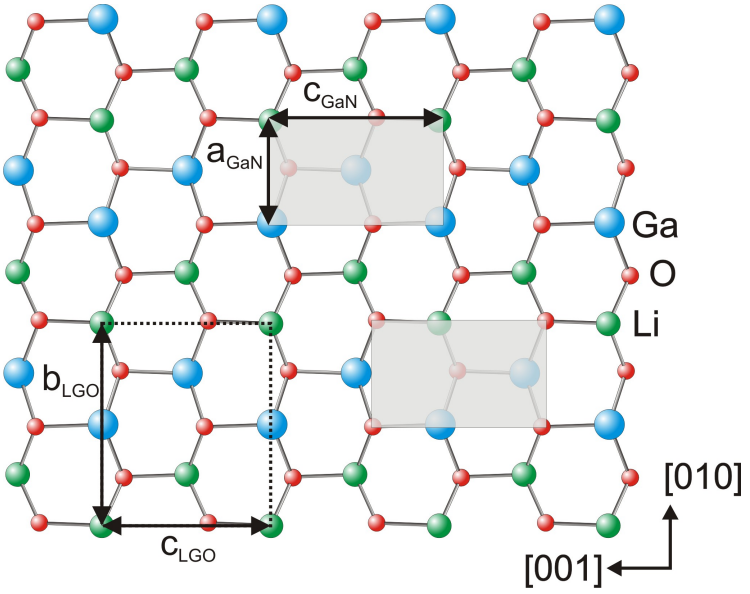

Figure 4.6: Ball and stick model of the (100) LGO surface. The dotted rectangle signals the size of the LGO unit cell, while the rectangles with continuous lines indicate possible nucleation sites for $(1\bar{1}00)$ GaN.

GaN growth. The lattice mismatch for the relationship $[010]_{\mathrm{LGO}} \parallel [11\bar{2}0]_{\mathrm{GaN}}$ and $[001]_{\mathrm{LGO}} \parallel [0001]_{\mathrm{GaN}}$ is only 0.07% and 3.58%, respectively. Growth on the (100) plane of LGO also benefits from the lack of a metal–non-metal polarity, which is an issue that has to be taken into account when growing on (001) LGO.

Due to transparency of the substrate in the visible and near infrared wavelength range the substrate was mounted onto a Si wafer using a thin layer of In to provide a homogeneous thermal coupling. The substrates, inserted into molybdenum holders, were first outgased for 60 min at 130 °C in the load lock chamber and thereafter transferred into the growth chamber. Activated nitrogen was supplied by the radio frequency plasma cell operated at a steady gas flow of 0.3 sccm and 450 W forward power. A growth rate of roughly 100 nm/h was used. Growth was monitored *in-situ* using RHEED. To prevent damage to the sample, care was taken to not irradiate the sample for too long with the electron beam.

Initial growth showed almost complete peeling off of the epitaxial film from the substrate. This may have a number of reasons such as damage caused to the substrate by its irradiation with highly energetic electrons from RHEED measurements. Moreover, an enhanced misfit of the anisotropic CTE between LGO and GaN at high temperature could facilitate the lift-off of the epitaxial film from its substrate. The exact direction dependent amount of stress caused by this mechanism is difficult to calculate as there is a large scatter of experimental data on the determination of the

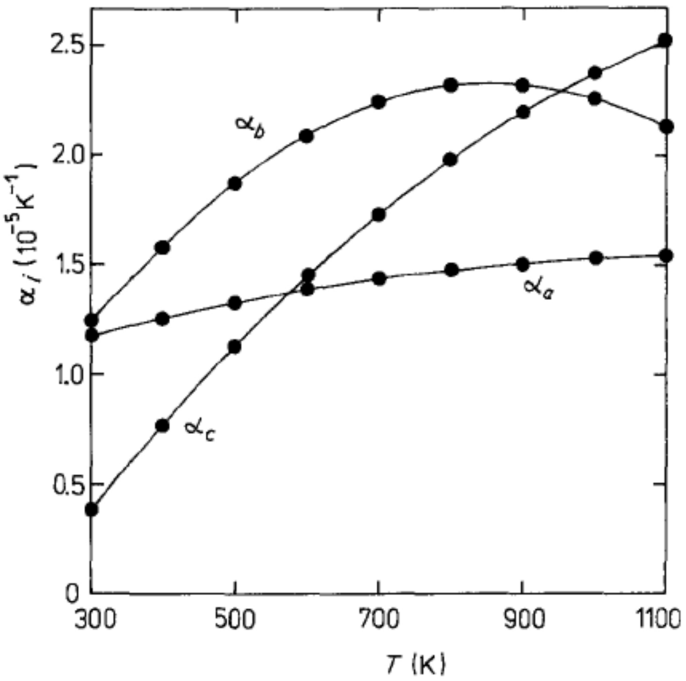

Figure 4.7: Non-linear behavior of the three coefficients of thermal expansion of $LiGaO_2$ in the temperature range between 293 K and 1100 K. Graph taken from [216].

CTE for LGO [172, 215–217]. However, from the data reported it is apparent, that there is a strong anisotropy in the LGO values for the CTE. In addition, the CTE in a temperature range of 700 K are not constant and as pointed out by Neumann et al. [216] each of the 3 different CTE in LGO shows a different non-linear behavior in the temperature range between 293 K and 1100 K. This is seen in the graph of Fig. 4.7, where the CTE of the three crystal directions a, b, and c are depicted in dependence of the temperature. Therefore the calculation of the stress caused using the CTE is inexact.

Rather, a direct comparison of the lattice parameters near the growth temperature GT = 700 °C and at room temperature (RT) is more reliable using data presented by Rawn and Chaudhuri [172] and Neumann et al. [216]. Here the resulting lattice mismatch near GT is subject only to small variations. The lattice parameters of GaN were calculated by the CTE given in [125] for high temperatures. The difference in lattice mismatch between GT and RT for GaN_a on $LGO_{b/2}$ then lies at 0.93% to 1.18% and for GaN_c on LGO_c at 0.50% to 0.61%. In both the $[11\bar{2}0]$ GaN and the [0001] GaN direction the stress induced from the LGO lattice onto the GaN lattice when cooling down is compressive. Since more stress is caused in the *a*-direction than in the *c*-direction of GaN, a cracking of the GaN film is expected

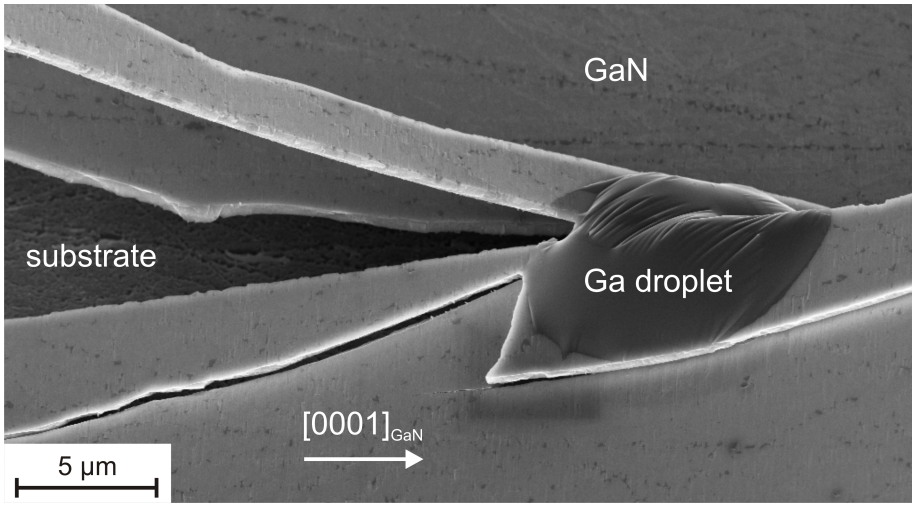

Figure 4.8: SEM image demonstrating the cracking in [0001] direction and lifting off of an M-plane GaN film on (100) LGO. The picture was taken with a 45° tilt towards the substrate surface.

along the c-direction. The cracks in c-direction are confirmed by SEM pictures (see Fig. 4.8) where the orientation of the film is inferred from previous reports of M-plane growth on different substrates, e.g. [166, 176, 220, 221], and experiences with M-plane GaN. From the relatively small change in lattice mismatch caused by thermal expansion it is unlikely that this mechanism is solely responsible for the peeling off of the epitaxial film from the substrate. However, a contribution of the anisotropic thermal expansion of GaN to this phenomenon can be expected.

A procedure for growth of M-plane GaN on LGO was found. However, due to the limited availability of substrates the growth conditions were not thoroughly optimized. The GaN film had cracks at the edges when taken out of the growth chamber, probably caused by a too high temperature in the area of contact between the substrate and the Mo holder. However, the center of the film remained stable and did not lift-off or show cracks. Prior to GaN deposition the substrate was annealed at 800 °C for 60 min. Thereafter, growth of GaN commenced at slightly Ga rich conditions at a substrate temperature of 700 °C. The temperatures given correspond to the thermocouple readings.

The sample was characterized *ex-situ* by XRD in a Bruker AXS D8 Discover diffractometer. A ceramic x-ray tube of type KFL Cu 2K was used to generate the characteristic $Cu_{K_{\alpha_1}}$ line. Scanning electron microscopy was performed on a LEO 1530 system at an operating voltage of 10 keV. AFM images were taken with a SiN tip in contact mode with an Autoprobe CP head from Park Scientific Instruments calibrated with a commercial calibration sample.

Characterization of GaN grown on (100) $LiGaO_2$ Observation of the RHEED patterns of the LGO substrate before and after annealing showed a remarkable improvement of the surface. In Fig. 4.9 two azimuths serve to illustrate the development of the reflection patterns. While the top two pictures, (a) and (b), show the reflection patterns of the substrate in [010] and [001] direction before annealing, part (c) and (d) display the situation after 1 hour annealing at 800°C for the same directions respectively. Because of the weak reflection signal from the substrate before annealing it was impossible to find the exact [010] and [001] azimuths. The pictures given in (a) and (b) therefore only roughly correspond to these directions. The two lowest pictures, (e) and (f), in this figure show RHEED images of the sample after growth, taken at the same angles as (c) and (d), respectively. They show streaky images of M-plane GaN along the $[11\bar{2}0]$ and [0001] directions, where the spacing of the streaks correspond to the c and a lattice constant respectively. Comparing the two RHEED images of LGO after annealing with the two lower pictures of GaN, the epitaxial relationship is demonstrated in accordance with Fig. 4.6. In other words, from the spacings of the RHEED streaks in Fig. 4.9 a high degree of lattice match of M-plane GaN on (100) LGO is evident for a_{GaN} on $b_{\mathrm{LGO}}/2$ and c_{GaN} on c_{LGO}. From the streakiness of the RHEED images, the film is expected to be flat and smooth. A spotty RHEED pattern would be an indication of a rough surface or even three dimentional growth (like found when growing quantum dots).

Surface scratches on the sample before and after growth are visible in optical microscope images (Fig. 4.10). These scratches most probably originate from mechanical polishing of the substrate. Fig. 4.11 shows the surface morphology of the GaN layer by means of SEM (a) and AFM (b). The epitaxial film has a thickness of 390 nm as measured by SEM. The slate-like surface modulation is typical for M-plane GaN. No indication of C-plane GaN could be observed at any point when performing microscopy on the film. The surface scratches from the substrate are visible as line discontinuities in the M-plane GaN film in both images. Despite these scratches, a small rms roughness of 2.9 nm is found in an area of 10×10 μm^2. Part (c) of Fig. 4.11 shows the depth profile of the line indicated in (b) over a range of 10 μm. A peak to valley roughness below 5 nm in regions without scratches and surface height variations up to 25 nm at the location of scratches is displayed. It is expected that the surface roughness will improve when polishing procedures and growth conditions are optimized, thereby also increasing the GaN film quality tremendously.

To examine the crystal orientation, quality and strain state of the epitaxial GaN film, x-ray diffraction scans were performed. Fig. 4.12 (a) shows an $\omega-2\theta$ scan in the range $\omega = 13° - 38°$ where the $(1\bar{1}00)$ GaN, (100) LGO and $(2\bar{2}00)$ GaN, (200) LGO peaks can be seen. This scan was performed in a double crystal configuration with a resolution of 0.005°. No other major peak is observed in the spectrum. Only an extremely small hint of a peak around $\omega = 17.16°$ with a maximum of 7 counts could be noticed, which may be attributed to a very small fraction of C-plane

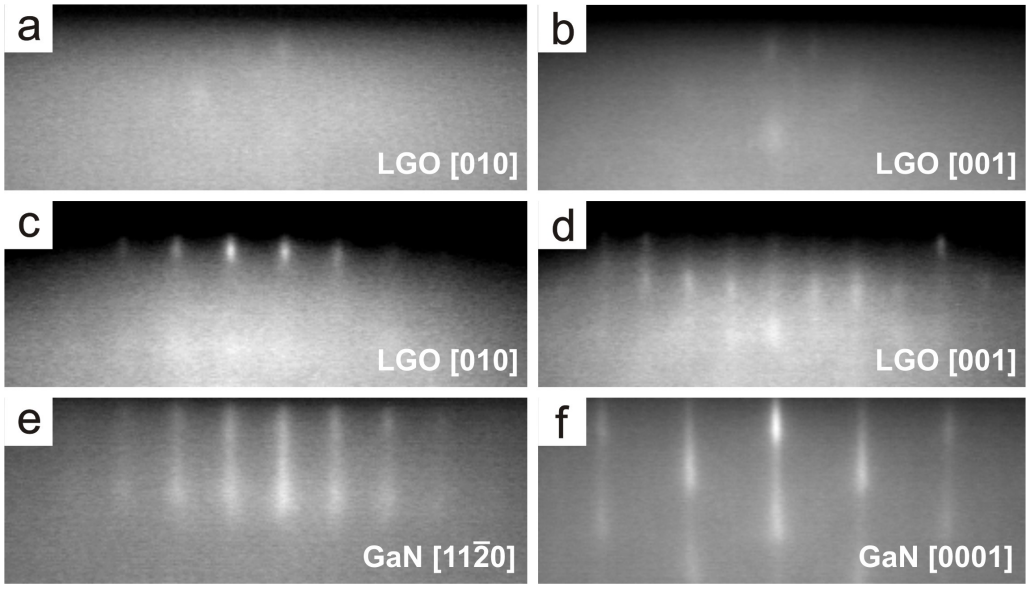

Figure 4.9: (a) and (b): RHEED images of two LGO azimuths, separated by 90° before annealing the substrate. The same azimuths of LGO after annealing, shown in (c) and (d), are much more pronounced, which indicates a clean surface. The two corresponding M-plane GaN directions, namely [11$\bar{2}$0] and [0001], after growth can be seen in (e) and (f). A streaky pattern is observed due to a flat surface of the film. The spacing of the streaks in [11$\bar{2}$0] direction gives the c_{GaN} lattice constant whereas the a_{GaN} lattice constant is given by the separation of streaks in [0001] direction.

GaN. However, this signal is far too weak for further analysis and with respect to the (1$\bar{1}$00) GaN peak with a maximum intensity of ∼900 counts it is safe to state a very high phase purity of M-plane GaN. Part (b) in Fig. 4.12 shows a more detailed measurement of the (1$\bar{1}$00) GaN and (200) LGO peaks with a resolution of 0.001° using a triple crystal analyzer. The strain state can be estimated from this measurement using the relative shift of the (1$\bar{1}$00) GaN peak with respect to the (200) LGO peak. Disregarding twist or tilt inside the GaN crystal, the GaN film is relaxed to roughly 80% compared to the maximal possible transverse deformation caused by the lattice misfit between LGO and GaN in the basal plane.

To determine the film quality, the rocking curve of the (1$\bar{1}$00) GaN peak was measured. The result is given in part (c) of Fig. 4.12 where a FWHM with a large value of ∼2500 arcsec is found. Although growth conditions were not optimized we expected a much lower value for the FWHM considering the quality of the sample surface from SEM and AFM data. The large FWHM value is probably mainly either due to irregularities propagated into the film from scratches on the substrate

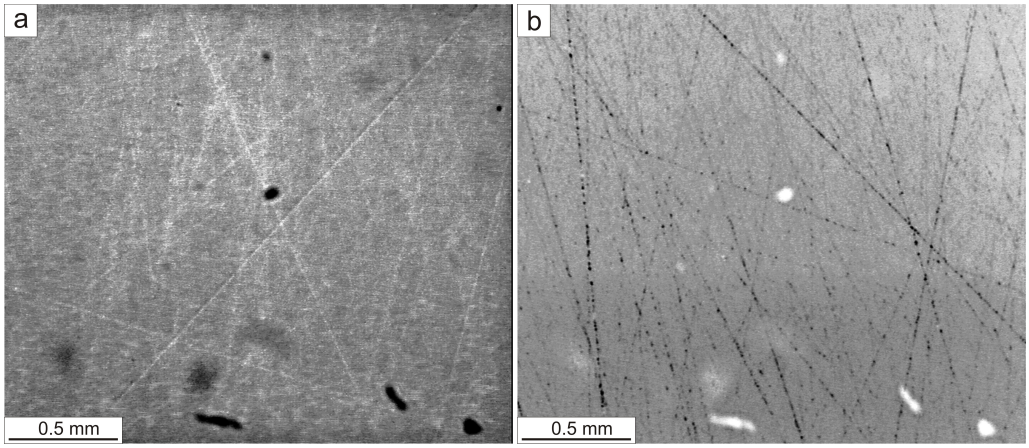

Figure 4.10: Optical microscope images of the substrate surface before growth (a) and of the sample surface after growth (b) at a magnification of 100×. The scratches on the substrate, probably caused by mechanical polishing, are clearly visible in both cases. The spots occurring mostly in the lower part of both pictures are due to impurities on the microscope lens.

surface (see Fig. 4.10) or caused by contributions to the Bragg reflection from the cracked edges of the GaN film. Yet, the value is much better than a recently reported study of M-plane GaN on (100) LGO, reporting a FWHM of 4121 arcsec for the $(10\bar{1}0)$ GaN reflection [222].

A plan view TEM sample of the M-plane GaN film was prepared by mechanical polishing and subsequent Ar-ion milling. Two cross-sectional TEM samples were fabricated by focused ion beam (FIB), one cut parallel to the C-plane and one parallel to the A-plane as is illustrated schematically in Fig. 4.13. Fig. 4.14 shows a typical FIB cut sample in an SEM. The thin part indicated in the picture is the region for TEM investigation. The samples were analyzed using a FEI Tecnai F20 TEM operated with an electron acceleration voltage of 200 kV.

The epitaxial relationship of the M-plane GaN sample can be deduced from Figure 4.15 (a) and (b), where the diffraction patterns taken from the GaN film and the LGO substrate, seen in Fig. 4.15 (c), are depicted. From the patterns, it is clear that $[11\bar{2}0]_{\mathrm{GaN}} \parallel [010]_{\mathrm{LGO}}$, and $(1\bar{1}00)_{\mathrm{GaN}} \parallel (100)_{\mathrm{LGO}}$. In Figure 4.15 (c), showing a bright field image of the sample cut parallel to the C-plane, a high density of threading dislocations is apparent. The bright areas in the substrate located directly at the interface of the substrate and the epitaxial layer represent holes in the TEM sample caused by the electron irradiation of the transmission electron microscope. Since LGO is very sensitive to electron bombardment, it is very difficult to obtain

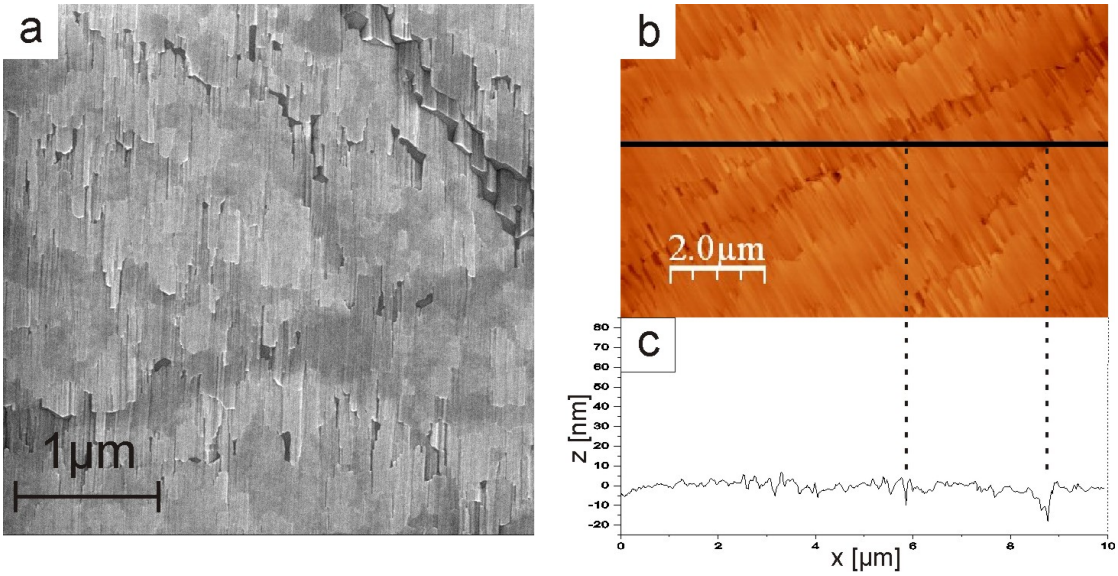

Figure 4.11: An SEM image of the sample surface is seen in (a) displaying a characteristic M-plane GaN slate-like modulation. A 6×10 μm^2 AFM scan is shown in (b), with a 10 μm long horizontal line depicting the profile given in (c). Height variations in the line profile correspond to scratches in the sample surface as indicated by the dotted lines.

good quality high-resolution images of this material. This issue was also discussed regarding RHEED measurements in the growth procedure above.

Looking at the sample cut parallel to the A-plane in Fig. 4.16 (b), a high density of partial dislocations associated with a high density of stacking faults can be seen. Figure 4.16 (b) displays the electron diffraction pattern of the GaN film seen in Figure 4.16 (a). The diffraction spots show streaks along the [0001] direction, giving strong evidence toward a high density of stacking faults in the film.

The plan view TEM sample of the GaN film allows for an estimate of the density of threading dislocations and stacking faults. A centered dark field image of one region of the plan view sample is seen in Figure 4.17. The numerous small dots represent threading dislocations that have reached the surface, while stacking faults, appearing as lines, are found running perpendicular to the [0001] direction as indicated, i.e., they lie in the C-plane. The elongated spots in the diffraction pattern inset in Figure 4.17 point toward the presence of twisted mosaic blocks in the film. The twist angle can be as high as 5°. In this sample, the threading dislocation density was found to be on the order of 1×10^{11} cm^{-2} and the stacking fault density around 2×10^{5} cm^{-1}.

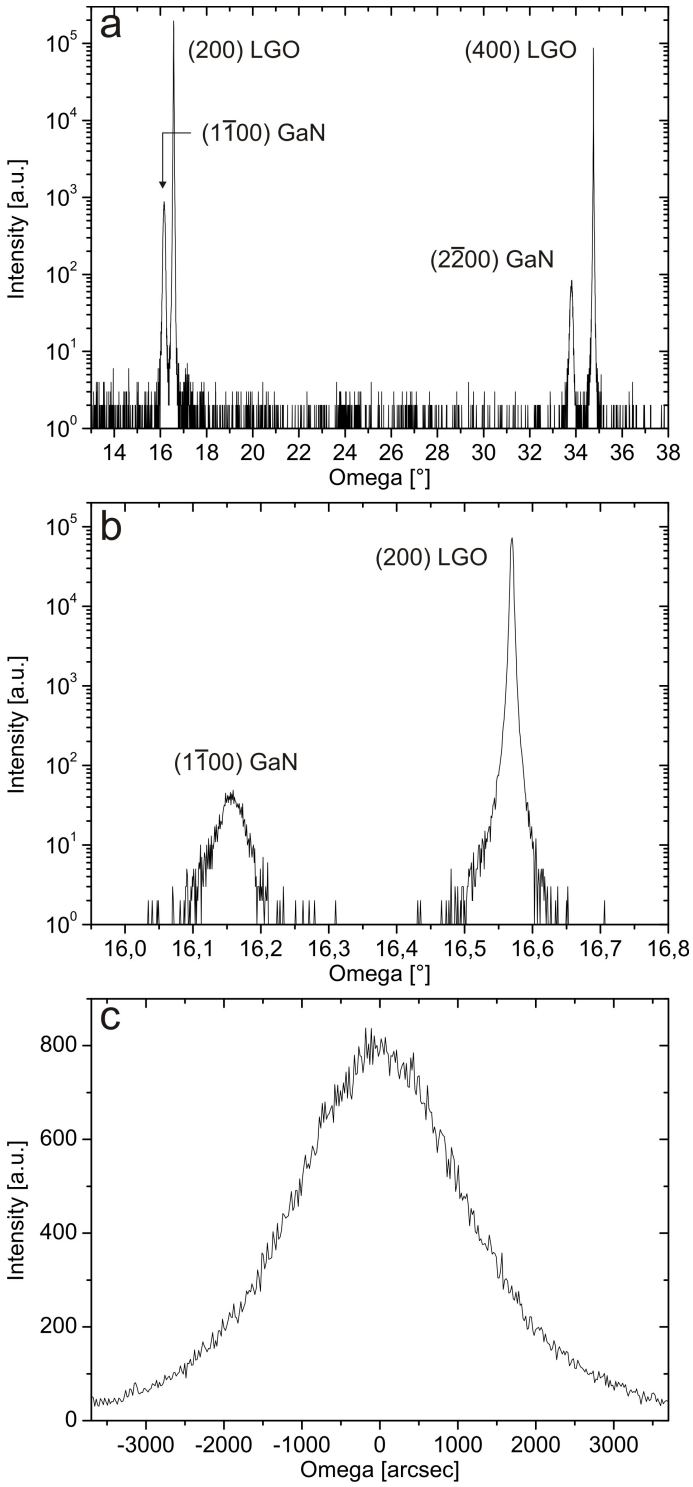

Figure 4.12: Part (a) shows an $\omega - 2\theta$ x-ray scan in double crystal configuration of a 390 nm thick GaN layer grown on LGO. Only M-plane GaN and (100) LGO related peaks are observed stating a high phase purity of the GaN M-plane. A higher resolution $\omega - 2\theta$ scan with a triple crystal analyzer in the range $\omega = 16° - 16.8°$ is seen in (b). (c) presents the rocking curve of the (1$\bar{1}$00) GaN reflection, the FWHM of which lies around 2500 arcsec.

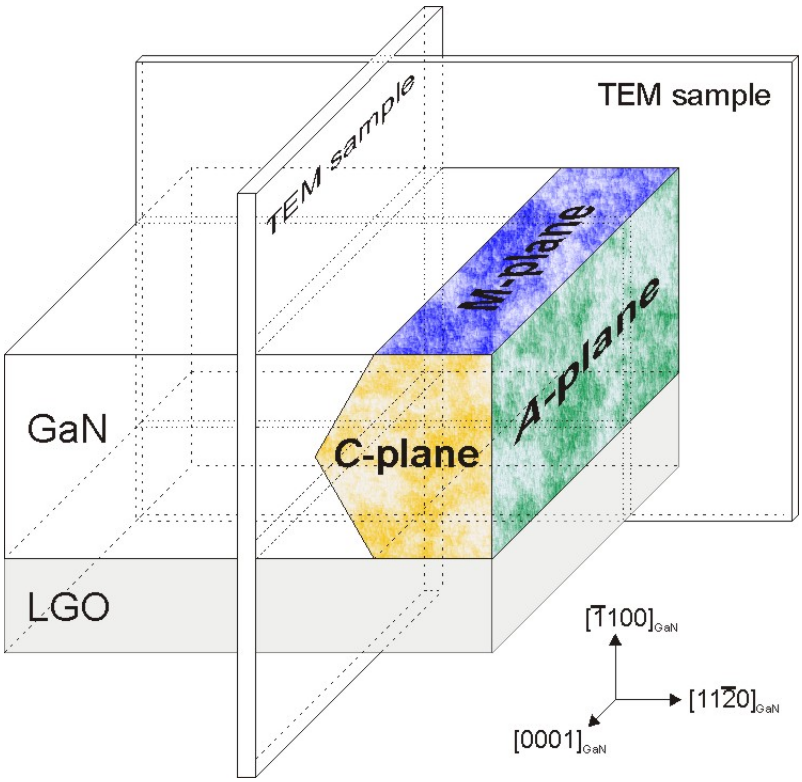

Figure 4.13: Illustration of the TEM samples prepared for analysis.

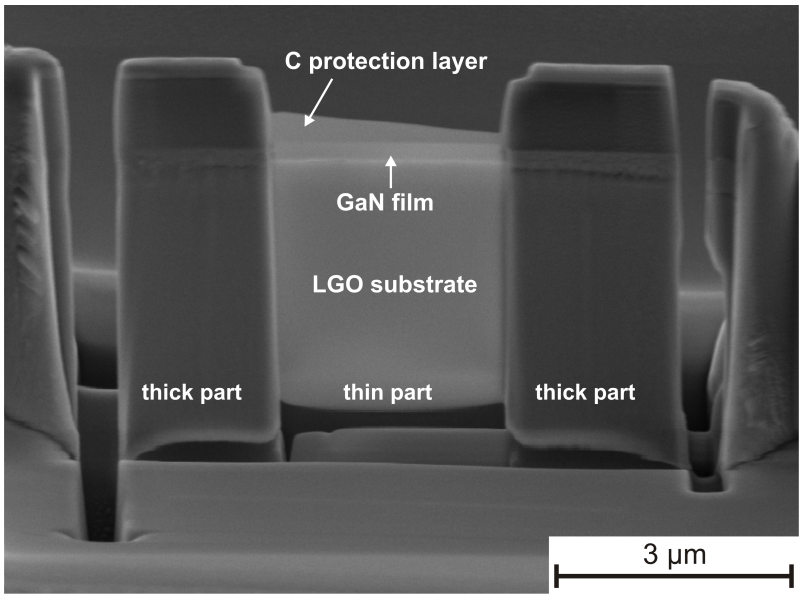

Figure 4.14: GaN TEM sample cut by a focused Ga ion beam.

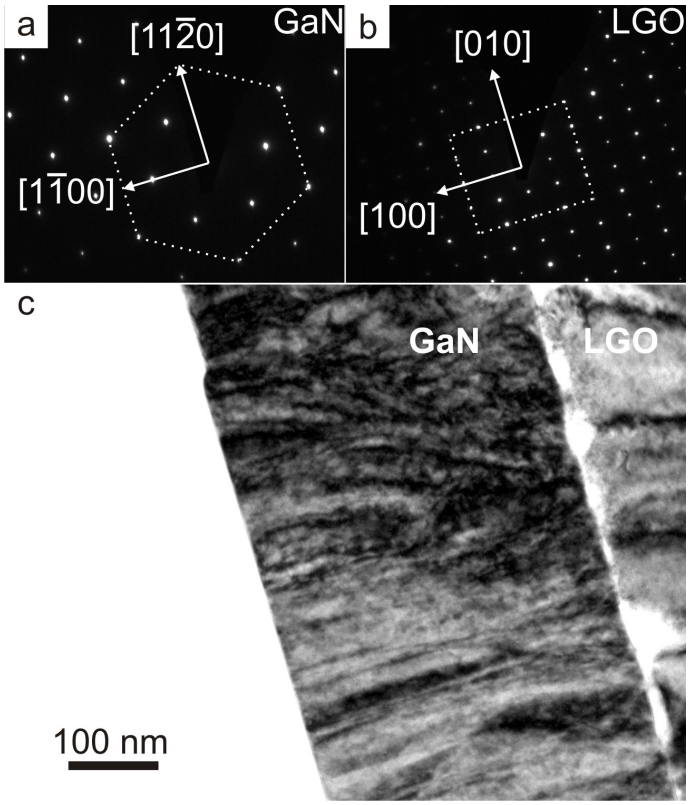

Figure 4.15: TEM data of the M-plane sample, with viewing direction [0001]. Parts (a) and (b) display the electron diffraction patterns of the GaN film and the LGO substrate seen in the bright field image in (c), respectively. The epitaxial relationship deduced earlier is confirmed. A high degree of threading dislocations is visible in in the GaN film.

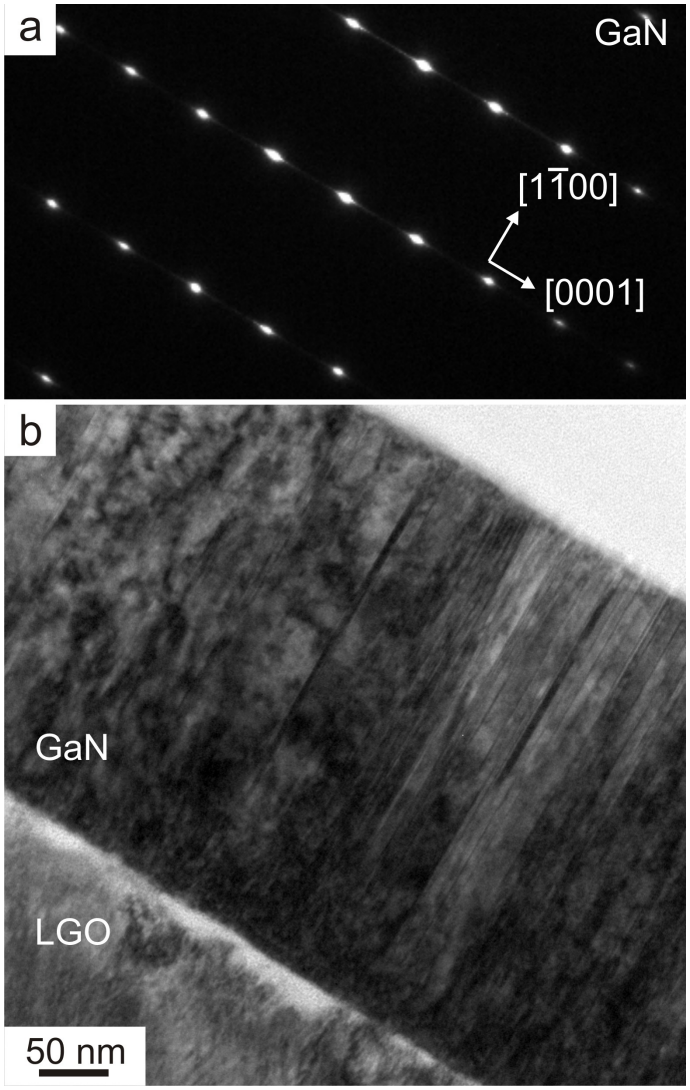

Figure 4.16: TEM data of the M-plane sample, with viewing direction [11$\bar{2}$0]. GaN diffraction pattern (a) and the corresponding bright field M-plane GaN film image (b). The data shows a high abundance of stacking faults in the sample.

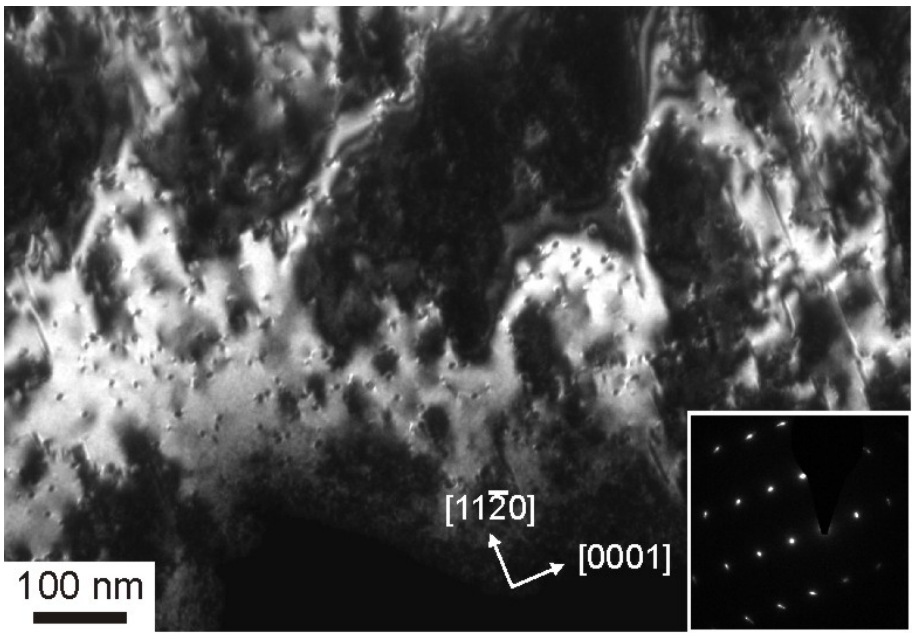

Figure 4.17: Inplane TEM sample of the M-plane GaN sample. Threading dislocations (spots) and stacking faults (lines) reaching to the surface are visible. The inset shows the GaN diffraction pattern and indicates a twist present in the crystalline film by the circularly elongated spots.

The dislocation density in this sample is higher than values reported in the literature $\sim 10^9$ cm^{-2} [158] for M-plane GaN, e.g. grown on $LiAlO_2$ by MOVPE. However, growth parameters had not been fully optimized on LGO and the film thickness here is twice as thin as in [158]. The thickness of the film is believed to have some impact on the threading dislocation density as is mentioned in [223] where the values for M-plane GaN grown on $LiAlO_2$ are given as 10^9 cm^{-2} near the substrate and 10^8 cm^{-2} near the surface. The stacking fault density in our sample is a little higher than the best value of 10^4 cm^{-1} [158] reported in literature, but is in the same order as the most frequently reported values.

4.2.4 Growth of A-plane GaN on (010) β-$LiGaO_2$

The growth procedure and conditions for A-plane GaN growth on LGO were essentially the same as for M-plane GaN. However small changes were made and for clarity, the whole procedure is described here again.

The epitaxial relationship of A-plane GaN on the (010) surface of LGO is shown in Figure 4.18 by a ball and stick model of the (010) LGO surface. The gray rectangles suggest possible nucleation sites for A-plane GaN growth. The lattice mismatch

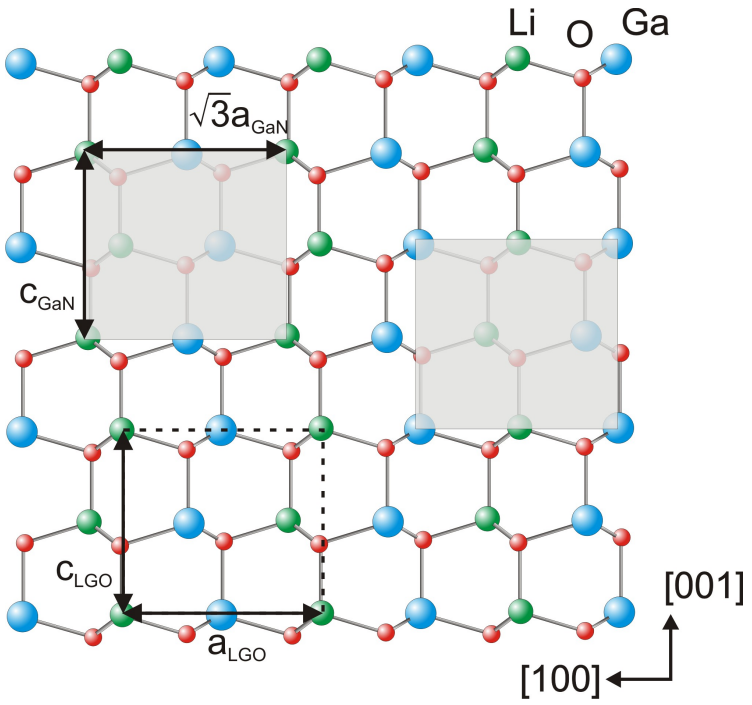

Figure 4.18: Ball and stick model of the (010) LGO surface. The dotted rectangle signals the size of the LGO unit cell, while the rectangles with continuous lines indicate possible nucleation sites for $(11\bar{2}0)$ GaN.

for the relationship $[100]_{\mathrm{LGO}} \parallel [1\bar{1}00]_{\mathrm{GaN}}$ and $[001]_{\mathrm{LGO}} \parallel [0001]_{\mathrm{GaN}}$ is 2.22% and 3.58%, respectively. Growth on the (010) plane of LGO, similarly to growth on the (100) LGO plane, benefits from the lack of a metal-non-metal polarity.

Before introduction to the MBE chamber, the LGO substrates were mounted onto a Si wafer using a thin In layer to provide for homogeneous thermal coupling. The substrates, placed into molybdenum holders, were outgased for 60 min at 130 °C prior to transfer into the growth chamber. During growth activated nitrogen N_2^* was supplied by the plasma cell, operated at a gas flow of 0.3 sccm and 450 W forward power for all samples. Growth procedures were monitored *in-situ* using RHEED.

To establish *A*-plane GaN growth the substrate temperature was optimized in the range between 650 °C and 800 °C and the Ga flux was varied from slightly Ga rich to Ga rich conditions. Several pre-growth treatments of the substrate in the growth chamber were studied. These were Ga desorption, nitridation, Ga desorption and nitridation, annealing and no treatment of the substrate.

Annealing the substrate at 800 °C for 60 min in the growth chamber directly before GaN deposition resulted in successful growth of *A*-plane GaN on LGO. Growth of

GaN commenced at slightly Ga rich conditions at a substrate temperature of 700 °C. The temperatures given correspond to the thermocouple readings. A growth rate of roughly 60 nm/h was used. Irradiation of the sample with the RHEED beam was reduced to a minimum to prevent possible damage to the sample, i.e. RHEED was only turned on after 30 min of GaN growth and in order to take RHEED pictures.

Shortly after taking the sample out of the growth chamber, the GaN film showed small cracks at the edges. A too high temperature in the area of contact between the substrate and the Mo holder probably is the reason for these features. However, approximately more than 98% of the film remained stable and did not lift-off or show cracks.

Characterization of GaN grown on (010) $LiGaO_2$ Samples from initial growth runs showed peeling off of the epitaxial film from the substrate as was also seen for the case of GaN grown on (100) LGO. Following several different substrate pretreatment approaches to prevent this, we found that annealing of the substrate lead to the desirable result. While RHEED patterns of the untreated substrate were dim and hinted to a contaminated surface, substrate cleaning by Ga desorption, nitridation or both together showed no observable effect. When a high Ga flux was used, RHEED observations showed an increasingly polycrystalline type diffraction pattern as soon as the Ga shutter was opened, indicated by ring like elongated horizontal spots.

A possible reason for the peeling off of the epi layer may have been the enhanced misfit of the anisotropic thermal expansion coefficients between LGO and GaN at high temperatures similar as discussed in section 4.2.3. Moreover, damage of the substrate's surface may have been caused by impinging highly energetic electrons from RHEED measurements. The polycrystalline RHEED patterns may result from bending of the partly peeling off film, thereby giving the impression of polycrystallinity.

In the following only the sample that was grown at optimized conditions will be discussed. Characterization of the sample was done ex-situ by XRD, SEM, AFM and TEM.

In Fig 4.19 (a)-(e) RHEED measurements of five azimuths are depicted. The top pictures show diffraction patterns of the substrate shortly before growth while the bottom pictures display electron diffraction patterns after 3 h growth of GaN for the same angles, respectively. The five azimuths of both, the LGO and GaN crystal, could reliably be identified in two ways thereby providing a valuable method of consistency check. First, the relative separation in angle was compared to the theoretical angle separation. The second method involved comparing the quotient of streak separation of the five azimuths to one another with the corresponding calculated values. The post growth pictures show streaky images of *A*-plane GaN hinting

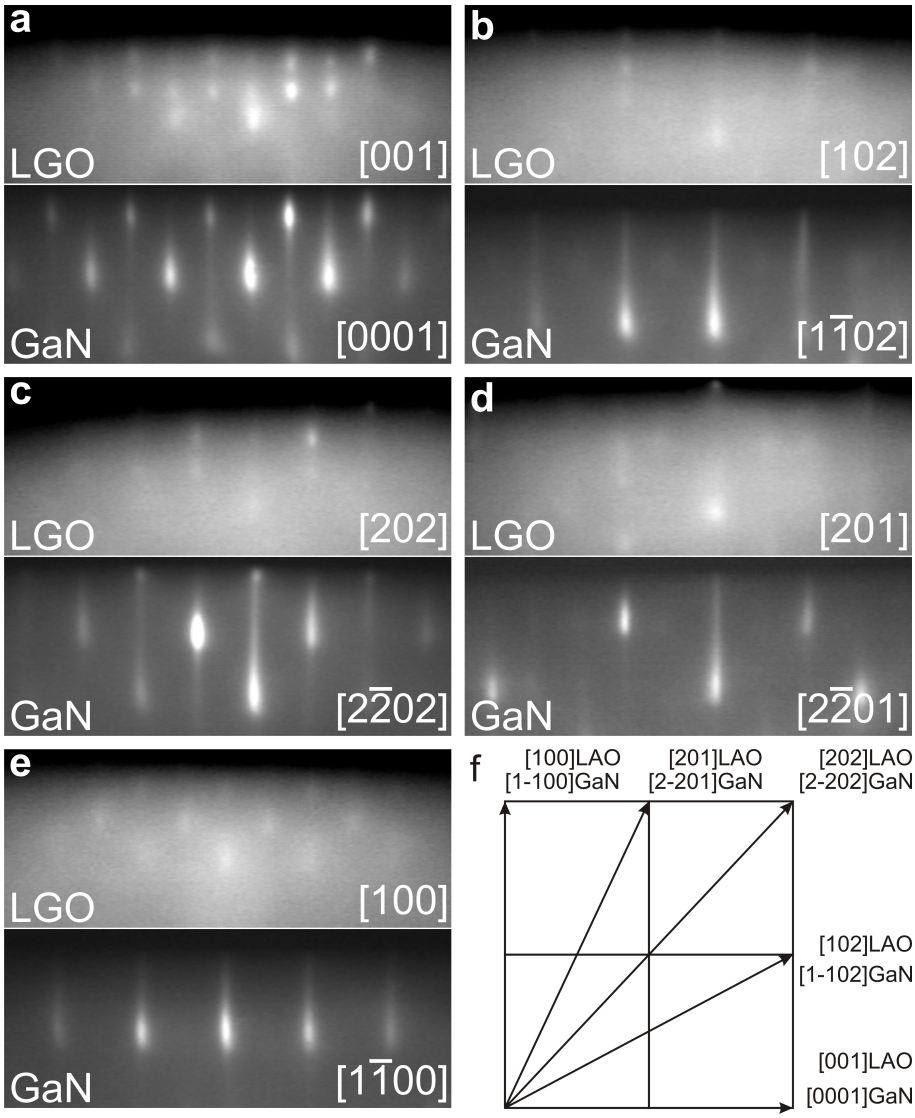

Figure 4.19: RHEED images of five azimuths of (010) LGO and (11$\bar{2}$0) GaN. Each pair of pictures (a)-(e) was taken at the same angles, the top one before and the bottom one after growth respectively. The close lattice match between the substrate and the film is evident. Streaky patterns indicate a smooth and flat surface. (f) shows a schematic drawing of the [11$\bar{2}$0] GaN surface indicating the directions of the observed azimuths, similar to how it was done for *M*-plane GaN by Waltereit *et. al* [139]. Calculation and measurement of angles and spacings allows the assignment of directions to the pictures.

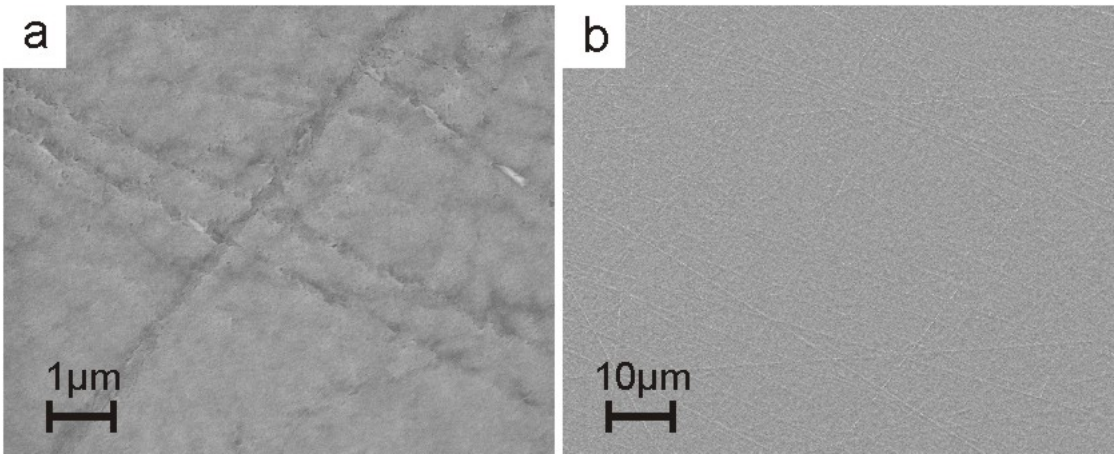

Figure 4.20: (a) SEM picture of the GaN surface using a 10k magnification. Deep scratches originating from the substrate are observable and intercept the continuity of the GaN film. (b) 1k magnification of the GaN film. A large number of scratches in the film are apparent.

towards a flat and smooth film. The correspondence of streak separation of the LGO and GaN for the same angle displays the close lattice match between the substrate and its epitaxial layer. Fig. 4.19 (f) shows how the directions of the observed RHEED patterns correspond to azimuths of both the (010) LGO and $(11\bar{2}0)$ GaN surface.

The thickness of the GaN epitaxial layer was measured in SEM to be 170 nm. In Fig. 4.20, part (a) and (b) show SEM pictures of the GaN sample surface using magnifications of 10k and 1k, respectively. Scratches in the GaN film, presumably caused by mechanical polishing of the substrate are clearly visible in both images. These surface irregularities are also observed in AFM images shown in Fig. 4.21. The depth profile of the horizontal line indicated in the AFM scan is graphed below. While the peak to valley roughness can be as high as 75 nm in parts with 'deep' scratches, an rms value of 10 nm is obtained on an area of 8×8 μm^2 when excluding the deepest scratches from analysis. Throughout the performance of microscopy no indication of C-plane or M-plane GaN, i.e. their typical crystal shape, could be observed in the film. It is expected that the surface roughness will improve when polishing procedures and growth conditions are optimized, thereby also increasing the GaN film quality.

The crystal orientation of the epitaxial GaN film was examined by x-ray diffraction. Fig. 4.22 (a) shows an $\omega - 2\theta$ scan in the wide range of $\omega = 12° - 78°$, performed without analyzer. All the apparent main peaks could be attributed to LGO planes. Two regions of the spectrum, that show additional information when zooming into them are displayed in Fig. 4.22 (b) and (c). Here, reflections of A-plane GaN planes

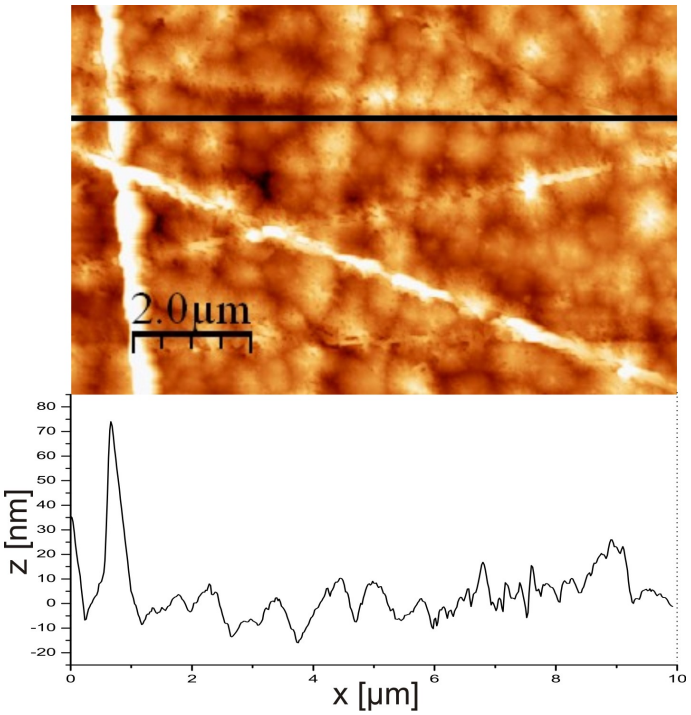

Figure 4.21: An about 7×10 μm^2 AFM image of the sample surface with a depth profile along the horizontal black line. The rms roughness of a 8×8 μm^2 areas as excluding the deepest scratches is 10 nm.

can be seen. Note that apart from diffraction peaks attributed to A-plane GaN and LGO no other peaks were observable. This means, a high degree of phase purity was found in the GaN film. The $(11\bar{2}0)$ GaN peak is convoluted with the (040) LGO reflection and does therefore not allow for an exact determination of the peak position of the GaN signal. The $(22\bar{4}0)$ GaN reflection has a broader shape and lower intensity giving a slightly larger error when determining its peak position. However, a strain state of the GaN epitaxial film could be estimated from the relative shift of the $(22\bar{4}0)$ GaN peak with respect to the (080) LGO peak. Disregarding twist or tilt inside the GaN crystal, the GaN film was relaxed to about 50% compared to the maximal possible transverse deformation caused by the lattice misfit between (010) LGO and $(11\bar{2}0)$ GaN.

Two cross-sectional TEM samples were fabricated from the A-plane GaN sample. Mechanical polishing and Ar-ion milling were used in the preparation of the sample with the C-plane as the sample surface, while FIB cutting was used to produce the sample with the M-plane as the TEM sample surface (see Fig. 4.23 for illustration). The samples were analyzed using a JEOL 3010 TEM as well as a FEI Tecnai F20 TEM, each operated with an electron acceleration voltage of 200 kV.

The A-plane GaN sample cut perpendicular to the [0001] direction, shown in Figure 4.24, displays a high density of threading dislocations. The images in Fig. 4.24 (a) and (b) are bright field images taken in the two beam condition with the $\vec{g}$ vector parallel to the $[11\bar{2}0]$ and the $[1\bar{1}00]$ direction, respectively. The inset in Fig. 4.24 (a) displays the diffraction pattern of the GaN layer showing evidence of the growth of A-plane GaN. Dislocations that have a burgers vector parallel to $[11\bar{2}0]$ can be observed in Fig. 4.24 (a); these are mixed and edge threading dislocations. In Figure 4.24 (b) both pure screw and edge dislocations are out of contrast since they have burgers vectors parallel to [0001] and $[11\bar{2}0]$, respectively [5], and can therefore not be seen. Owing to the much lower density of visible dislocations in Figure 4.24 (b), we can state that most dislocations are of either edge or screw type and a minority belongs to the mixed type. In Fig. 4.24 inversion domain boundaries appear in both pictures as straight lines as indicated. These have an inclination of 60° with respect to the interface, i.e. they lie on the other two $\{11\bar{2}0\}$ planes of GaN.

Comparing in-zone bright field images of the M- and A-plane films, the threading dislocation density of the two films is on the same order of magnitude, i.e., around 1×10^{11} cm^{-2}.

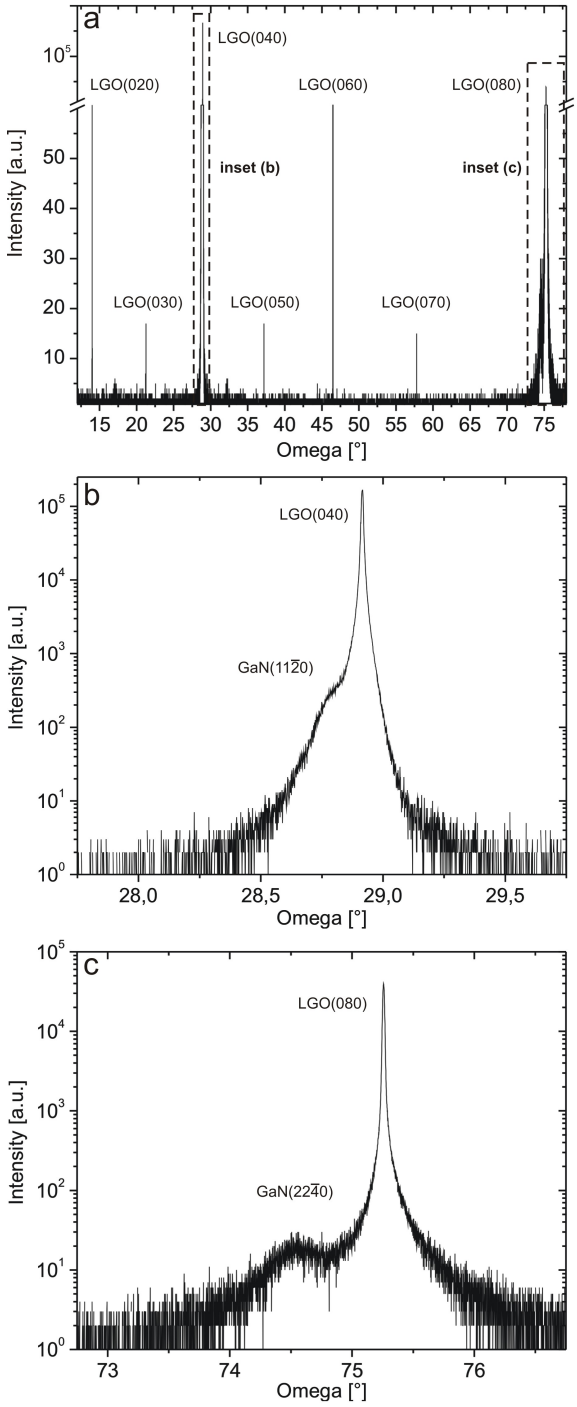

Figure 4.22: (a) $\omega - 2\theta$ wide range x-ray scan without analyzer of a 170 nm thick GaN layer grown on (010) LGO. Diffraction peaks of several LGO as well as *A*-plane GaN planes can be seen. There is no indication of diffraction peaks of any other oriented crystal planes. (b) zoom into the region $\omega = 27.75° - 29.75°$ where the clearly visible right shoulder of the (040) LGO peak can be attributed to (11$\bar{2}$0) GaN. (c) zoom into $\omega = 72.75° - 76.75°$. Here, the diffraction peaks of *A*-plane GaN and LGO lie further apart allowing for a simple strain state analysis.

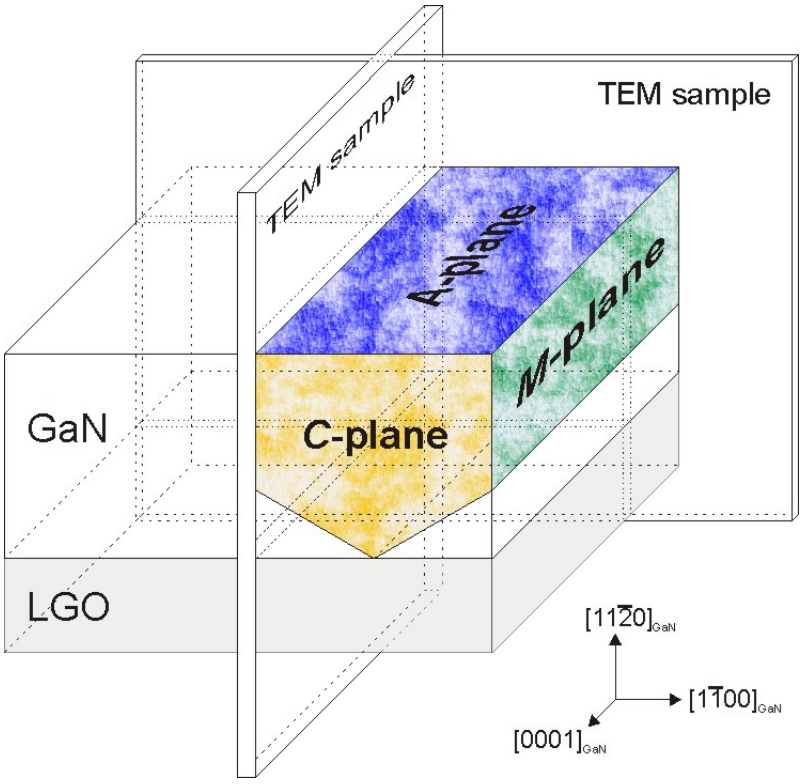

Figure 4.23: Illustration of the TEM samples prepared for analysis.

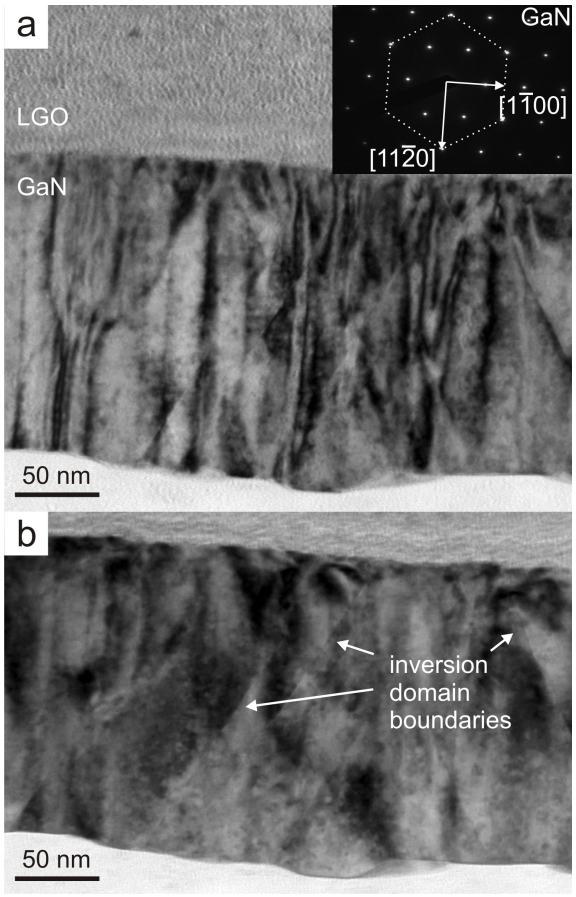

Figure 4.24: Bright field images of the *A*-plane GaN sample taken in the two beam condition with the $\vec{g} = (11\bar{2}0)$ (a) and $\vec{g} = (1\bar{1}00)$ (b). The viewing direction for these images is [0001]. Threading dislocations and the presence of inversion domain boundaries, bordering stacking faults, are visible.

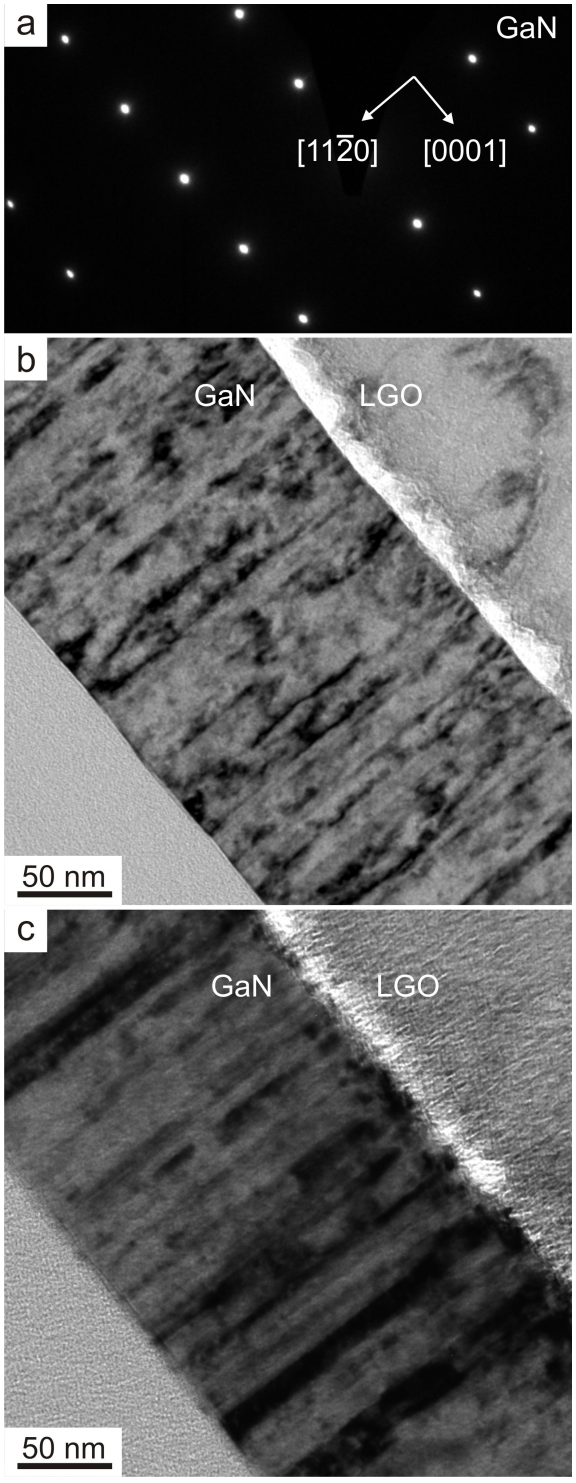

Figure 4.25: TEM data of the A-plane sample, with viewing direction $[1\bar{1}00]$. (a) Diffraction pattern of the GaN film of the A-plane GaN sample. (b) and (c) show bright field images of the same sample taken in the two beam conditions with $\vec{g} = (0002)$ and $\vec{g} = (11\bar{2}0)$, respectively. Threading dislocations and stacking faults can be seen, however, much fewer stacking faults are present than in the M-plane GaN film.

Fig. 4.25 (b) and (c) show bright field images of the A-plane GaN sample cut perpendicular to the $[1\bar{1}00]$ direction taken in the two beam condition with $\vec{g} = (0002)$ and $\vec{g} = (11\bar{2}0)$, respectively. Damage to the substrate by the electron beam is again seen. Threading dislocations as well as stacking faults are visible. Slightly more dislocations appear in the image with $\vec{g} = (0002)$ indicating that there are more pure screw threading dislocations than edge dislocations. In comparison to the M-plane GaN sample, much fewer stacking faults are present in the A-plane film. This observation is also confirmed by the missing streaks in the diffraction pattern, shown in Fig. 4.25 (a). This means that the stacking fault density is lower than $\sim 10^5$ cm^{-1}, and therefore lower than values reported previously for A-plane GaN e.g. grown on R-plane sapphire by MOCVD, 3.83×10^5 cm^{-1} [160] or by PAMBE, $\sim 2 \times 10^5$ cm^{-1} [224].

4.2.5 Summary and conclusion of GaN grown on β-$LiGaO_2$

It has been shown for the first time that M-plane and A-plane GaN can be grown epitaxially on (100) $LiGaO_2$ and (010) $LiGaO_2$, respectively, using plasma-assisted MBE. Thermal annealing of the substrate before growth proved to be a procedure well suited to clean its surface and seems to be necessary for obtaining stable GaN films. This is a comfortable solution of cleaning a substrate's surface, due to the lack of elaborate cleaning or pretreatment steps prior to epitaxial growth. The growth conditions, like pre-growth annealing and growth temperature were also used in a recently published study, which also shows growth of M-plane GaN on LGO [222]. Streaky RHEED patterns after growth in addition to the SEM and AFM data show very smooth M- and A-plane GaN, despite the presence of polishing related surface scratches on the substrates. The XRD results indicate a high degree of phase purity for both film orientations and showed that the strain was relaxed to 80% for the M-plane and to 50% for the M-plane GaN film as compared to the maximal possible strain that could have been induced due to the lattice mismatch between film and substrate. A high phase purity of the grown material is a very desirable property of the film and sometimes poses great difficulty to achieve. However, as the results shown above prove, growth of GaN on LGO states the easiness of obtaining high phase purity of GaN, which is closely related to the close lattice match of the substrate with GaN.

The analysis of the M- and A-plane GaN films by transmission electron microscopy show that the epitaxial relationship of the film with the substrate is in agreement with the results obtained from RHEED and XRD. Threading dislocations and stacking faults are seen to be the main defects in the films. For the case of the M-plane GaN sample, a threading dislocation density of 1×10^{11} cm^{-2} and stacking fault density of about 2×10^5 cm^{-1} were found. The A-plane sample shows a threading

dislocation density on the same order; however, a much lower stacking fault density as compared to the M-plane sample. Although the threading dislocation density is very high and the stacking fault densities are in an equivalent range as for other substrates used for heteroepitaxy it can be expected to obtain smoother surfaces and a higher crystal quality of the GaN films when mechanical polishing of the substrate as well as growth conditions have been thoroughly optimized. Once the technological issue of polishing for a smooth substrate surface has been solved it would be very interesting to optimize the growth procedure for the fabrication of non-polar GaN on LGO.

5 Cu incorporation in GaN

Cu-doped group III nitrides, as discussed in sec. 2.3.3, have earned great interest due to the experimental evidence of ferromagnetism observed in GaN [117] and AlN [225] at room temperature, hence serving as a prospective candidate for a spin-aligning material in spintronics. The usage of Cu as a dopant, which is a non-magnetic element, excludes the possibility of magnetic clusters built by the dopant. Therefore the occurrence of ferromagnetism in GaN:Cu does not origin from either Cu or GaN, but is a result of the interaction between the host material and the dopant.

Theoretical work studying ferromagnetic Cu-doped GaN has foremost assumed Cu atoms on substitutional Ga sites, e.g. [17, 114, 115, 226]. For instance, Wu et al. [17] explain that incorporation scenarios other than Cu substituting Ga sites are not taken into account because they are energetically unfavorable. However, since most growth processes of doped GaN do not take place in a thermodynamic equilibrium environment, the occupation of unfavorable energetic states may not be excluded. Seong et al. [18] stating ferromagnetism in Cu-doped GaN nanowires show by anomalous x-ray scattering that Cu atoms do indeed substitute onto Ga sites, but do not comment on nitrogen or interstitial site occupation. It is still unclear to what extent Ga sites are occupied and whether N or interstitial sites also play a role in Cu incorporation. Sun et al. [119] for example, see that the total magnetization of their Cu implanted samples increases with higher doses but the magnetic moment per Cu atom decreases. This is speculated to stem from an increased incorporation of Cu atoms on interstitial sites. However, experimental evidence of interstitial Cu being responsible for a diminishing of the magnetic properties and substitutional positions enhancing them can only be obtained if the positioning of Cu in the GaN matrix is known. To get insight into the influences of the placement of Cu to the systems magnetic properties, the fundamental question of where and how Cu is incorporated in GaN must be answered.

For this purpose X-ray Absorption Near Edge Structure (XANES) and X-ray Linear Dichroism (XLD) measurements of a series of Cu-doped GaN samples with different doping concentrations were investigated at the Ga and Cu K-edge. This means that electrons from the 1s orbital of Ga and Cu, respectively, were excited by x-rays from a synchrotron beam line. At the lowest energies, i.e. at the absorption edge, the inner electrons are mainly excited into unoccupied states of the 4p orbitals.

While in XANES the edge position and shape is sensitive to the formal valence state, ligand type, and coordination environment, which can be used to identify phases [227], XLD provides a convenient tool to probe the local structural and electronic properties of the Cu atoms in the nitride host, since it is proportional to the anisotropic unoccupied density of charge [228]. The XLD spectrum is therefore highly sensitive to the local symmetry and gives a unique signature in the case of wurtzite structure and no signal amplitude for cubic crystal symmetry [228]. By comparing the measured data to simulations performed by use of the FDMNES code [21], the incorporation fraction of Cu atoms in the nitride host as Ga or N substitutes or on interstitial sites can be deduced.

In this chapter the experimental procedure of the sample preparation, measurements at the synchrotron in Grenoble and details to the simulations (sec. 5.1) will be described. Thereafter, the experimental findings and their interpretation will be presented in section 5.2 by a first surface analysis of the samples (sec. 5.2.1) followed by the presentation of the XANES and XLD data which are then interpreted with help of the calculated spectra in sec. 5.2.2. Finally, section 5.3 summarizes the findings of this study.

5.1 Experimental procedure

The investigated samples were grown by plasma-assisted molecular beam epitaxy by Philipp Ganz using the system described in section 3.3.2. A series of six GaN:Cu samples with varying nominal Cu concentration from 0% to 2.69%, in the following labeled A(0%), B(0.50%), C(1.35%), D(1.77%), E(2.22%) and F(2.69%), was produced. The term "nominal concentration" used here refers to the flux ratio of Cu atoms to the total metal atom flux of Cu and Ga. Assuming sticking- and incorporation-coefficients to be the same for Cu and Ga and equal to unity, these numbers would represent an estimate of the actual doping concentration of Cu. However, these assumptions are not justified and hence, the nominal concentration can only be seen as a measure of the relative flux provided during growth. As will be described later, a significant part of the provided Cu atoms form metal compounds in the samples, i.e. not all of the provided Cu is available as doping material in the GaN film. In this series of samples, sample C with 1.35% nominal Cu doping takes in a special position due to the measured ferromagnetic behavior. The data is not shown here, but its magnetic behavior as well as the growth procedure applied is very similar to the case reported earlier [20].

To obtain better thermal coupling during growth, *C*-plane oriented sapphire substrates were mounted onto silicon using indium as an adhesive. Each substrate was first outgased in a baking chamber at 130 °C for 60 min before introducing it into

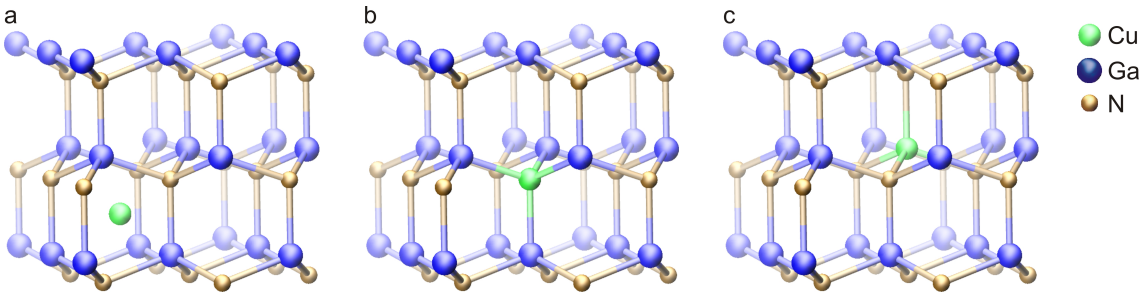

Figure 5.1: Schematic representation of part of a GaN 4×4×4 supercell. (a), (b) and (c) show how the Cu atoms are placed in the GaN matrix on interstitial, N and Ga sites, respectively.

the growth chamber. It was then heated to 890 °C for 30 min for a final outgasing step before nitridation commenced for 180 min at 200 °C. A thin AlN buffer layer (thickness $\approx 22 \pm 4$ nm as measured by Scanning Electron Microscopy (SEM)) was introduced prior to the growth of the epitaxial Cu-doped GaN layer. A growth rate of roughly 70 nm/h was used, resulting in GaN film thicknesses in the range of 130-150 nm. After unloading the sample from the molecular beam epitaxy (MBE) system, it was cut into parts, one of which was etched and one left unetched. The etching of the samples was performed to remove metal compounds from the samples and included 65% HNO_3 treatment for 5 min and rinsing with deionized water. To obtain an understanding of the effect of etching on the samples, their surfaces were investigated by SEM.

For all samples the XANES and the XLD spectra were measured at the K-edges of Ga and Cu, i.e. around 10367 eV and 8979 eV, respectively. These measurements were performed with hard x-rays from the ID12 beamline at the European Synchrotron Radiation Facility (ESRF) detecting the total fluorescence yield. The experimental chamber contains eight silicon photodiodes arranged in a semi sphere around the sample that are equipped with 10 μm thick Ni filters. A quarter wave plate was used to flip the linear polarization of the synchrotron light from vertical to horizontal when performing the XLD measurements, also described in detail in [229]. The angle of incidence was between 14° and 17° with respect to the sample surface. For the analysis of the XANES and XLD spectra we have to keep in mind that the illuminated sample area is much larger than the size of a surface compound and also much larger than the mean distance between the compounds. The x-ray signals collected are therefore an average of the sample and do not probe parts of the sample locally. In addition, the hard x-rays of the synchrotron are assumed to penetrate the samples completely, leading to a probing of the whole volume of the samples instead of only the surface layers.

XANES and XLD spectra were simulated using the FDMNES code [21] applying the multiple scattering formalism within the muffin-tin approximation. To obtain a doping concentration of Cu in GaN which is comparable with the Cu concentration in the experimental samples, a wurtzite supercell of $4\times4\times4$, i.e. a total of 256 atoms, with a calculation radius of 10 Å was used. GaN lattice constants of $a = 3.188$ Å and $c = 5.185$ Å were used [124]. For the x-ray absorption spectra eight different doping concentrations were calculated, the lowest possible ranging from 0.78% (with 1 Cu atom in the supercell) up to 6.25%. The variation of doping concentration in the supercell, however has almost no influence on the calculated spectra. Due to this fact, for reasons of clarity, only the 1.56% doped spectra are plotted in the analysis to follow. Configurations of Cu in the GaN crystal substituting Ga atoms, N atoms or as interstitials in the largest void of the GaN matrix (see Fig. 5.1) were performed. The two Cu atoms are separated by the largest possible distance to avoid possible clustering effects.

5.2 Results and conclusion

During growth of the Cu-doped GaN samples Cu is not only incorporated in the film but also forms cubic [230], non-magnetic γ-Cu_9Ga_4 structures according to X-Ray Diffraction (XRD) [117] and Transmission Electron Microscopy (TEM) analysis [231]. Because of the different placement possibilities of the Cu atoms in the sample (in the GaN film or in the γ-Cu_9Ga_4 structures) a clear distinction of the origin of the Cu signal present in the XANES and XLD spectra must be clarified. For this purpose measurements on as grown samples as well as on samples where the surface compounds had been removed by wet chemical etching were compared.

In a first step, an estimate of the Cu incorporation in the GaN film and the γ-Cu_9Ga_4 compounds is done by means of SEM surface analysis. This gives a better understanding for the following analysis because the intensity of the absorption signal is proportional to the amount of atoms present in a specific chemical configuration. Since XLD probes the anisotropy of the valence charge, Cu atoms in GaN give a wurtzite type signature, if e.g. substituting Ga sites, but should give no signal contribution when bound in γ-Cu_9Ga_4 compounds, as a result of the compounds' cubic symmetry [232]. In a second step the x-ray absorption spectra are examined. From the surface sensitive SEM analysis the majority of Cu, which is incorporated in the sample, is expected to be found in the γ-Cu_9Ga_4 compounds. This observation is still valid after etching, where most of the γ-Cu_9Ga_4 could be removed, however leaving behind between 12% and 35% of the compounds, depending on the sample. Due to the hence expected big influence of γ-Cu_9Ga_4 compounds on the absorption spectra we first turn to look at the XLD spectra, where only a non-cubic coordination of Cu gives a non-zero signal, to make sure Cu is really incorporated

in the GaN film. We shall see in the following that we do indeed observe a non-zero XLD signal at the Cu K-edge, proving Cu occupation in the GaN crystal. To gain confidence to the answer of the actual Cu placement in GaN, we thereafter analyze the XANES spectra, which are not dominated by the Cu signal incorporated in GaN but are definitely influenced by it. XANES and XLD simulations of Cu-doped GaN, performed for Cu placement on Ga, N and interstitial sites, and of γ-Cu_9Ga_4 compounds are compared to the experimental data to extract numbers for the fractions of differently occupied sites in GaN by Cu.

5.2.1 γ-Cu_9Ga_4 surface compounds

A first estimate for the amount of Cu present in the surface compounds (Cu_9Ga_4) with respect to the film can be deduced estimating the Cu_9Ga_4 island coverage using SEM images (Fig. 5.2) and an average height estimate of 220 nm from TEM pictures of the samples [231]. An important assumption included in the following evaluation, namely that all the precipitates visible on the sample surfaces are only composed of γ-Cu_9Ga_4, is justified by the fact that they are all formed during growth, i.e. at a temperature of 790 °C (by thermocouple reading). This can be assumed because some of the compounds have been overgrown by a thin GaN film and is supported by TEM data [231]. Further, a mean Cu to Ga ratio with 32.78% Ga in these compounds is assumed in accordance with the phase diagram given in [233, 234].

A decrease in surface compounds on the samples could be achieved by etching. This is clearly seen for sample F in SEM images taken of the as grown (Fig. 5.2 (a)) and the etched (Fig. 5.2 (b)) sample. The left part of the pictures, where black circles surround the structures, is an example of how the estimated surface coverage of Cu_9Ga_4 was taken into account in the calculations (in this case the area covered by Cu_9Ga_4 was 8.22% of the total sample area). The sample after etching showed an 88% decrease of the compounds. Table 5.1 gives an overview of all the Cu-doped samples with their nominal Cu concentration and in each case the values of the volume percentage of Cu_9Ga_4 in the sample before and after etching along with the relative and absolute decrease of the amount of compounds. The last two columns give the calculated ratio of Cu atoms bound in the compounds with respect to the total metal atom content of the sample (excluding the amount of Cu in the film, as it is known only for sample C). The fact that the amount and size of the Cu_9Ga_4 compounds on the sample surface increases with increasing nominal Cu concentration is clearly reflected in the numbers of Table 5.1.

Note that the calculated ratio of Cu, forming compounds, to the total metal content is already higher than the provided Cu to metal flux ratio during growth. This is a plausible outcome because the provided flux ratio of Cu and Ga is not the same ratio as is built into the sample. It is a clear indication that the sticking- and

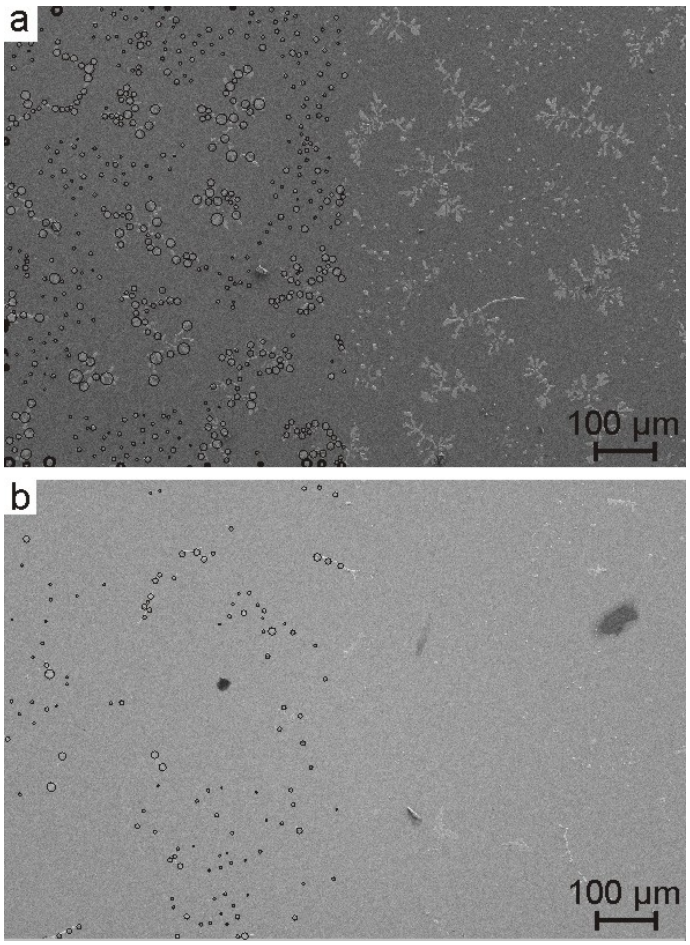

Figure 5.2: SEM image of sample F (2.69%) before etching (a) and after etching (b). On the left sides of the pictures the surface coverage of the precipitates is estimated by approximating the structures' area with the area of multiple small circles. For this sample, an 88% decrease in the surface coverage of the surface structures is calculated from the pre-etched to the post-etched condition of the sample.

Table 5.1: Listing of the Cu-doped GaN samples with the estimated γ-Cu_9Ga_4 coverage by SEM measurements.

sample	**nominal conc. [%]**	$\mathbf{V}_{Cu_9Ga_4}/\mathbf{V}_{sample}$ [%]		$\mathbf{V}_{Cu_9Ga_4}$ **decrease [%]**	$\mathbf{V}_{Cu_9Ga_4}$ **decrease [mm^3]**	**# Cu at. in Cu_9Ga_4/ # metal at. [%]**	
		unetched	etched			unetched	etched
B	0.50	1.46	n.a.			3.47	
C	1.35	3.19	0.81	79.74	3.47×10^{-4}	7.26	1.95
D	1.77	5.72	3.02	65.43	4.13×10^{-4}	12.27	6.89
E	2.22	6.39	2.15	74.84	6.48×10^{-4}	13.51	5.01
F	2.69	11.44	1.56	88.03	15.88×10^{-4}	21.78	3.68

incorporation-coefficients of Cu and Ga on GaN are different. While the sticking coefficient for Cu can be assumed to be near unity, because of its low vapor pressure at the growth temperature used in this study [235, 236], it is higher for Ga [237]. It is therefore impossible to deduce a reliable number for the Cu concentration in the GaN film by this kind of analysis. However, using results obtained by wavelength dispersive x-ray spectroscopy (WDXS) on a 1.38% nominally Cu-doped sample, where 0.26% of the metal atoms in the GaN film were Cu atoms [231], we can deduce a 'real' doping of 0.24% Cu for sample C assuming the same Cu incorporation rate for both these samples. This means, considering the presence of Cu_9Ga_4 compounds, that approximately 3.1% of the Cu atoms in the sample are incorporated into the GaN film, whereas the remaining roughly 96.9% are found in the compounds. The situation appears reversed when calculating the percentage of Ga in the film and in the compounds, where the estimated numbers are 96.5% and 3.5%, respectively.

As a first outcome of these estimates we can state that the majority of Cu that is present in the samples is incorporated in the compound of γ-Cu_9Ga_4. By etching it was possible to remove most of the compounds, but not to 100%. The XANES spectra are therefore expected to be dominated by signals originating from the compounds. XLD however, is insensitive to cubic coordination of bound atoms and shall therefore be free of a signal originating from the compounds. In the following the analysis of XLD at the Ga K-edge, followed by the Cu K-edge will be shown. Thereafter, in section 5.2.3, the XANES spectra at both edges will be discussed.

5.2.2 X-ray linear dichroism of Cu-doped GaN

XLD at the Ga K-edge In XLD spectra recorded for the etched and unetched samples at the Ga (Fig. 5.3 (a), (b)) and Cu K-edge (Fig. 5.3 (c), (d)) we can clearly see an increase of the XLD signal for the etched samples compared to the unetched ones. Regarding the Ga edge the increase of signal amounts to an average of about

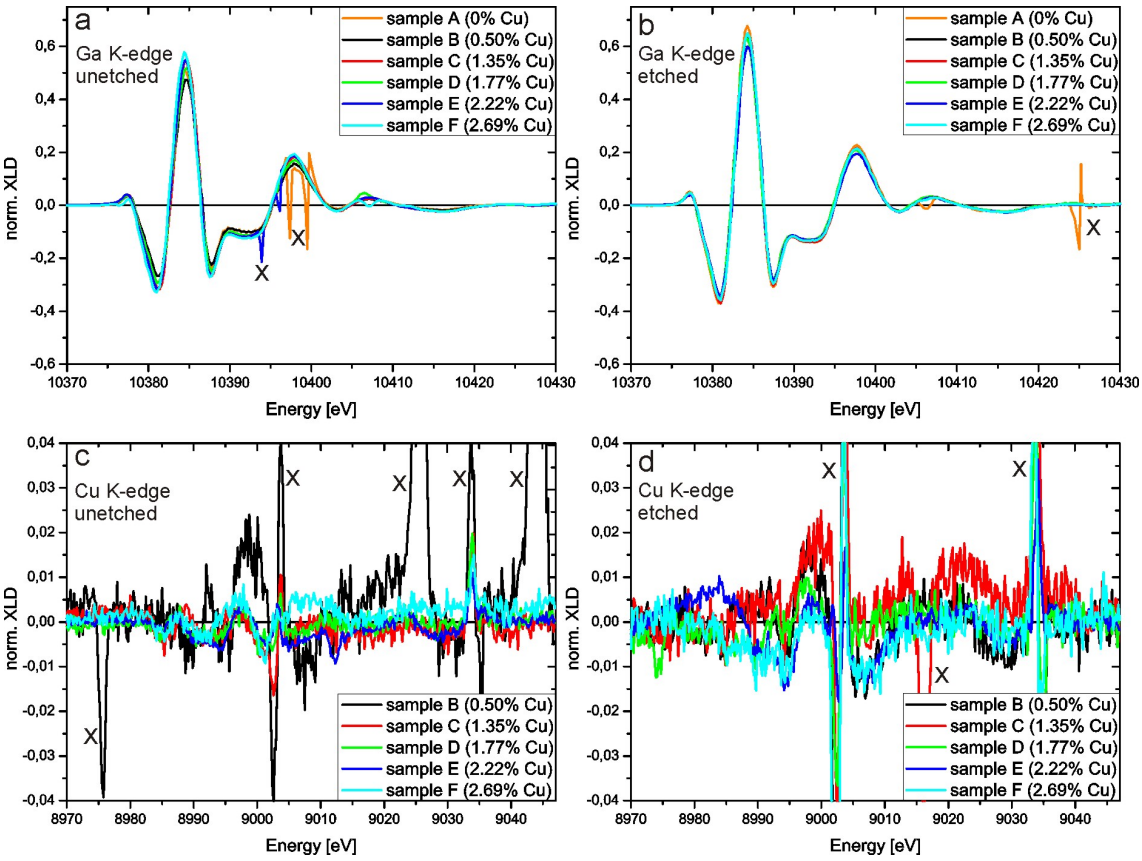

Figure 5.3: The measured XLD spectra depicted here were normalized to the background at the lowest and the highest energies of the spectrum. (a) and (b) are the XLD spectra of the Ga K-edge prior to and after etching of the samples, respectively. (c) and (d) show the XLD spectra of the Cu K-edge before and after etching of the samples, respectively. Bragg peaks are marked by "×".

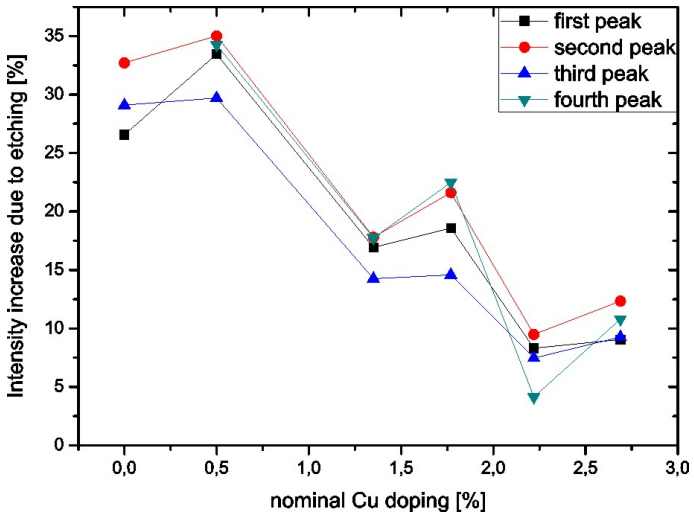

Figure 5.4: The intensity increase of the XLD peaks at the Ga K-edge between etched and unetched samples is shown as a function of the nominal doping concentration. The increase is due to the removal of Cu_9Ga_4 compounds (see text for discussion).

7% to 33%, depending on the sample. This behavior of the XLD signals' intensity increase due to etching for the different samples and peaks can be seen in Fig. 5.4. The intensity variation between etched and unetched samples can be explained by the fact that after etching cubic surface compounds (Cu_9Ga_4) have been removed and a higher percentage of the signal collected origins from the wurtzite film, hence giving more intense peaks in the XLD spectrum. The non-uniformity in the increase of the intensity can be ascribed to the different amount of compounds removed from the different samples, as was also seen in the SEM analysis above (see the absolute $V_{Cu_9Ga_4}$ decrease column in Table 5.1). The tendency of higher nominally doped samples giving less increase of the XLD signal is presumably due to the short etching time applied. This means that because more Cu supply during growth leads to more compounds, a longer etching time is needed to completely remove the compounds. However, for all samples the etching time was constant leading only to a partial removal of the compounds and in conclusion to a higher percentage of remaining Cu_9Ga_4 on the samples having been exposed to higher Cu fluxes.

The sharp Bragg peaks in the graphs of Fig. 5.3 are marked by "×" and occur because some crystal lattice planes in the samples satisfied the Bragg condition with respect to the position of some of the detectors and yield no information which is of interest here. Apart from the slight variation in intensity, an examination of differences in the Ga K-edge XLD signal in dependence of the Cu doping cannot be observed. However, comparing the experimental XLD data of the Ga K-edge to simulations (Fig. 5.5 (b)), we can state that only a very small percentage of Cu atoms

is located on N substitutional sites. This conclusion is drawn from the qualitatively greatly differing curve progression of the simulated data for 2 N atoms having been replaced by 2 Cu atoms in a $4 \times 4 \times 4$ supercell calculation. A clear analysis of a quantitative measure of Cu atoms occupying Ga, N or interstitial sites is not possible at this stage, due to the inaccuracy in modeling these spectra. The effect of the inaccuracy can be shown in Fig. 5.5 (a) where the experimental and simulated data of pure GaN are depicted. Although a fairly good qualitative agreement is apparent, it shows that the fit is not good enough to discriminate between Cu on Ga or interstitial sites in Fig. 5.5 (b).

XLD at the Cu K-edge The much lower signal to noise ratio of the XLD signals of the samples recorded at the Cu K-edge compared to the Ga edge data is clearly visible in Fig. 5.3 (c) and (d). Nevertheless, the increase of the signal from the unetched to the etched samples is apparent, again resulting from a lower fraction of compounds present in the samples, thereby being responsible for less absorption of x-rays in the cubic structure (not contributing to the XLD signal). In graph (c) of Figure 5.3, sample B seems to divert significantly from the rest of the samples. This is however not considered to be of physical origin; rather the behavior is traced back to difficulties in reliably normalizing the data acquired for this sample due to the presence of two intense Bragg peaks (marked by "$\times$" in the graph) and the low statistics compared to the data of the other samples, therefore being responsible for impracticable intensity comparisons. Due to the generally low statistics of the data for all samples, resulting from limited beam time and a low incorporation amount of Cu in the GaN film, a comparison of the signals' intensities with respect to the different doping concentration is unfeasible. However, a clear statement of the presence of an XLD signal is possible, leading to the conclusion that Cu is really incorporated in the GaN film and is not merely present in the form of Cu_9Ga_4 compounds.

Although the statistics of the experimental data makes a quantitative analysis difficult, an idea of where most of the Cu atoms are placed in the GaN host lattice can be extracted when comparing the non-zero XLD experiment signal to the simulations (Fig. 5.6). We observe that the intense first negative peak in the Cu on N sites graph is missing in the experimental data. Hence a large percentage of Cu on N sites can safely be assumed to be limited to a very small amount. Similarly, the Cu on Ga and interstitial sites make a contribution to this first negative peak, but with much lower intensity, therefore not contradicting with the possibility of a significant percentage of these configurations being present but unresolved in the experimental data. Interestingly, the best matching spectra to the experimental curve is the XLD signature of Cu on interstitial sites where the shape of the maxima correspond well with the two peaks in Fig. 5.6 (d).

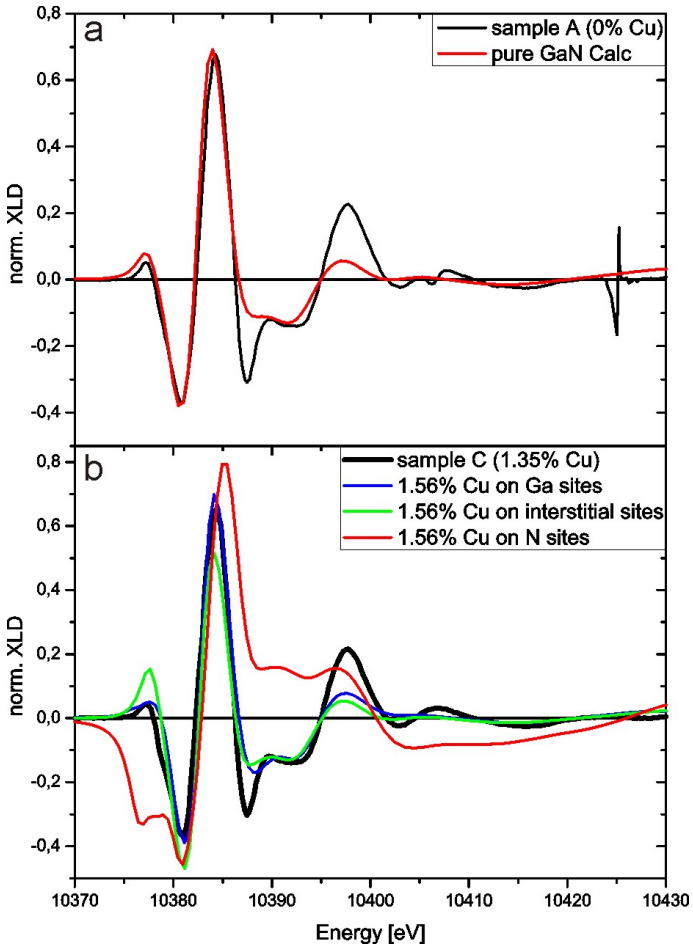

Figure 5.5: Comparison of the measured Ga K-edge XLD signal to the simulated ones. (a) shows the undoped spectra, while (b) displays the measured graph of sample C (1.35%) in comparison to calculated spectra for different Cu site possibilities. The misfit of the red curve to the experimental data indicates very little N site occupation of the Cu atoms.

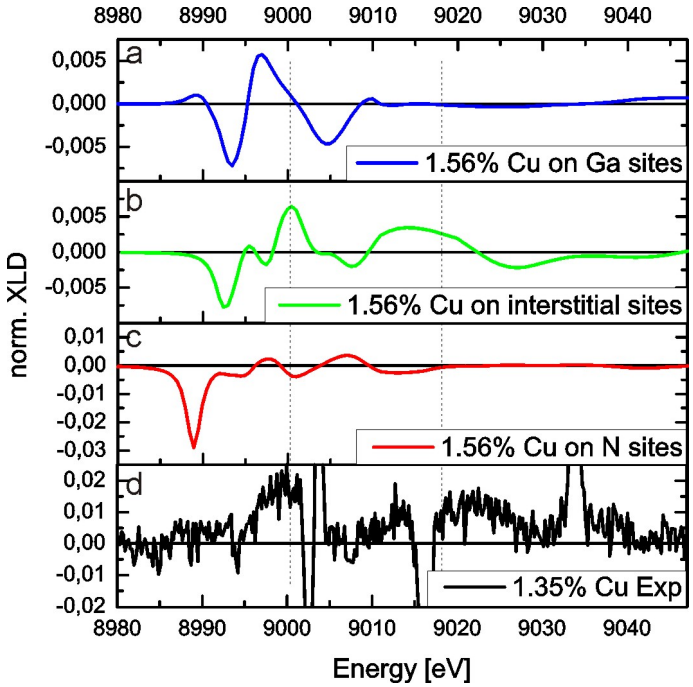

Figure 5.6: (a) to (c) depict the Cu K-edge XLD simulation results for 1.56% Cu-doped GaN on Ga, N and interstitial sites, (d) shows the experimental data of sample C (1.35%). As a guide to the eye the two main peaks present in (d) are marked by dotted lines throughout the other graphs.

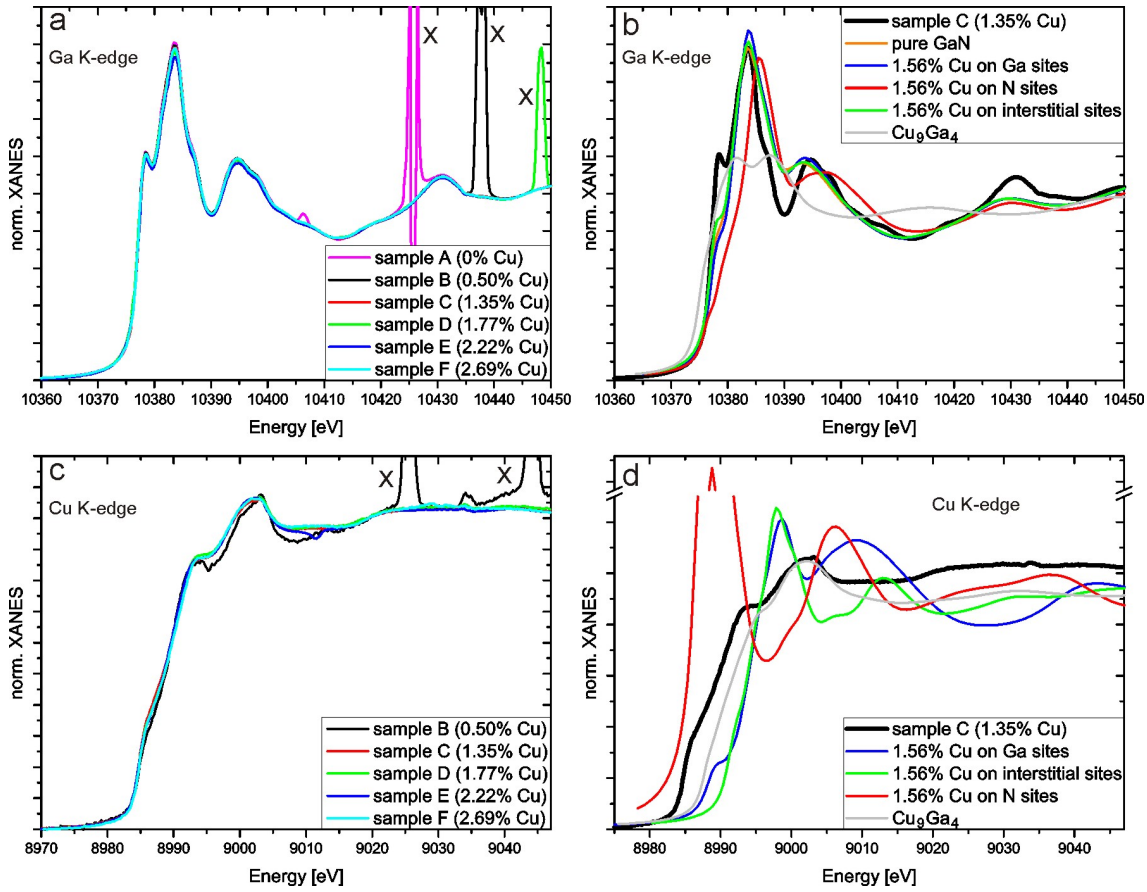

Figure 5.7: Experimental XANES spectra of the Ga (a) and Cu (c) K-edge for the differently doped samples. (b) and (d) show the experimental XANES data of sample C (1.35%) along with calculated spectra for Cu on different sites for the Ga and Cu K-edge, respectively.

5.2.3 X-ray Absorption Near Edge Structure of Cu-doped GaN

XANES at the Ga K-edge The experimental XANES data of the samples at the Ga K-edge (Fig. 5.7 (a)) show hardly any variation for the different doping concentrations. This is expected, because the amount of Cu incorporated in the lattice is small leading to even smaller differences in the incorporation amount from one sample to another which should not affect the Ga signal of the film a great deal. The large spikes in the higher energy region of samples A(0.00%), B(0.50%) and D(1.77%), marked by "×" in the graph are again Bragg peaks which are only avoidable when tilting the sample. Here, however, the peaks are well away from the region of interest in the spectrum, thereby not causing any confusion identifying the real XANES signal.

In Fig. 5.7 (b) the comparison of one of the experimental curves (sample C) with the simulated data is shown. Here, simulation results are shown for pure wurtzite GaN (0% Cu) as well as for GaN with 2 Cu atoms in a $4 \times 4 \times 4$ supercell (1.56% Cu) replacing Ga atoms, N atoms and situated as interstitials.

The comparison of the calculated data with the experimental one in Fig. 5.7 (b) displays general agreement between the two in a number of points. The main peak around 10383 eV is very well described by all simulated curves apart from the curve for Cu on N sites, which is shifted to higher energies by 2 eV. One might be tempted to explain the high energy shoulder of the main peak by a possible admixture of Cu occupation of N sites in GaN. This case is repeated for the next peak at around 10395 eV, where again the high energy shoulder in the experimental data could be explained by the substitutions of Cu on N sites. However, as these shoulder-peaks in the experimental spectrum are also present in the undoped GaN spectrum, we no further need to analyze the origin of these features with respect to Cu doping. We assume the lack of precise matching comes about because of the inaccuracy of the theory and claim that the low percentage of Cu in the GaN film does not noticeable affect the spectrum. Further, the simulations fail to describe more details of the measurement, most noticeably the low energy rising edge of the spectrum where a distinct peak in the experimental data is seen. This peak also appears in the calculations but is rather a shoulder. It is most pronounced when Cu occupies interstitial sites in the GaN lattice; its exact origin, however, cannot be concluded to be due to Cu, for the same argument as above holds, namely that it is also present in the undoped sample. Ga bound in γ-Cu_9Ga_4 compounds cannot be seen to influence the spectrum as the double peak feature in the calculated Cu_9Ga_4 spectrum is completely absent in the experimental data. The calculation of Cu_9Ga_4 was performed for one unit cell (52 atoms) and a cluster calculation radius of 10 Å.

XANES at the Cu K-edge Turning to the XANES spectra at the Cu K-edge (Fig. 5.7 (c)), as in the case for the Ga K-edge, there is no significant difference visible between the samples with different Cu concentrations. This outcome is not surprising remembering the considerations of section 5.2.1 involving the SEM images, where we stated that other than for the Ga signal, the Cu signal mainly has its origin from the Cu incorporated in the Cu_9Ga_4 compounds and not from Cu in the GaN film. The spectrum of sample B may seem to differ from the rest, but with regard to the lower statistics in the experimental data for this sample compared to the others, also apparent in the lower signal to noise ratio, the small deviation to the rest of the samples can be considered insignificant.

Fig. 5.7 (d) depicts the experimental data as well as the simulated data for 1.56% Cu-doped GaN where Cu is sitting on Ga or N substitutional sites, as interstitials or is bound in Cu_9Ga_4. It can clearly be seen that the shape of the experimental

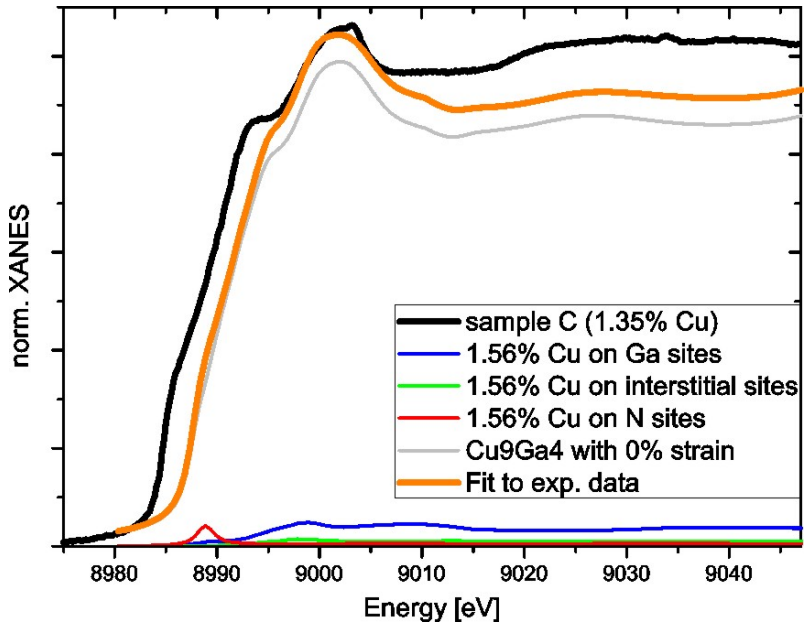

Figure 5.8: Fitting of the experimental XANES graph of sample C (1.35%) with different calculated Cu site positions.

data most accurately fits the calculated Cu_9Ga_4 graph. However, the shoulder in the rising edge of the measured data is not accounted for in the Cu_9Ga_4 curve. This aspect can be explained by a slight portion of N sites being occupied by Cu atoms. Unfortunately as can be seen by the strongly Cu_9Ga_4 dominated shape of the experimental data, signals of an admixture of the Cu component coming from the Cu atoms incorporated in the GaN film are highly suppressed, i.e. an experimental curve fit with a contribution of one or more of the GaN:Cu curves can be established but is subject to a large uncertainty.

Although an accurate fit is not possible for the entire spectrum, a tendency of Cu site occupation can be extracted when deconvoluting the XANES Cu K-edge spectrum (Fig. 5.8) by considering the four possible signal origins (Cu on Ga, N, interstitial sites or in Cu_9Ga_4). A good overall fit of the experimental data was achieved for a placement of Cu atoms at 4.0% Ga , 0.6% N and 1.1% interstitial sites; the remaining 94.3% of the signal is attributed to Cu_9Ga_4. This means that for Cu in the film 70% is on Ga, 20% on interstitial and 10% on N sites. Although these numbers are values for the best fit when deconvoluting the experimental spectrum the error bars are rather large, i.e. similar fits can be obtained with a different occupation of Cu in GaN. To find a range where this is possible, the data was fit with the maximum tolerable Cu fraction in each position of Cu on Ga, N and interstitial sites. The result is that Cu can occupy between 0 - 6.2% Ga, 0 - 0.8% N and 0 - 6.8% interstitial sites

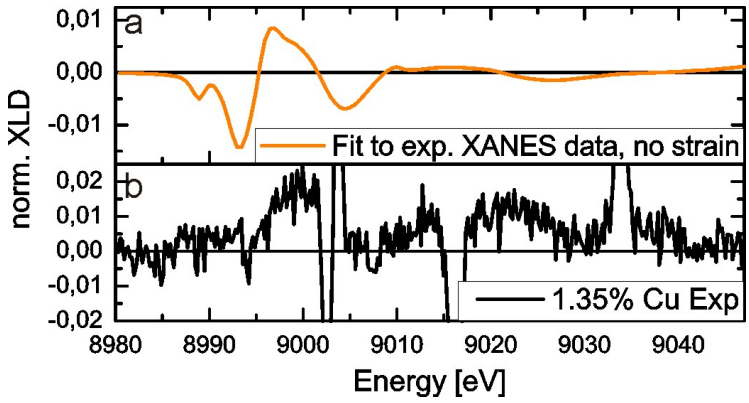

Figure 5.9: (a) shows the simulated XLD data of GaN:Cu with a mixture of the possible sites (Ga, N, interstitial) that Cu can occupy, according to the same fractions of contributions as described for the XANES spectra in Fig. 5.8. (b) displays the experimental XLD curve of sample C.

in GaN within the sensitivity of our measurement and is to 93.2 - 100% present in Cu_9Ga_4 compounds.

Going back to the simulation of XLD spectra at the Cu edge and plugging in the values of Cu occupation on the different GaN sites extracted from XANES we expect to see a good fit with the experimental data if the XANES fit was reasonable. The simulation, where the composition of the signal is the same as the one determined by the XANES data, and the experimental data are shown in Fig. 5.9 (a) and (b), respectively. It can be seen that the calculation describes the measured XLD data well within the sensitivity of the measurement. Further, the order of magnitude of the signal's intensity is well described in this case where the majority of the signal is assumed to be absorbed by the Cu_9Ga_4 compounds. The fact that the fit results of the XANES spectra correspond well to the XLD spectra is an important check for consistency and makes the data, in spite of the low signal to noise ratio, reliable.

The results from this analysis roughly correspond to the results from the SEM considerations above, i.e. from XANES we conclude that 5.7% of the Cu in the sample is in the film whereas from a combined SEM and WDXS analysis it was an estimated fraction of 3.1%. Due to the numerous assumptions leading to these numbers the discrepancy is not surprising. Nevertheless, important information can be gained: Cu is incorporated in the film; Cu is not only incorporated on Ga sites; Cu occupies N sites to a measurable extent. This is a finding that has not been previously reported and may lead to new theoretical considerations of different defects, other than only Cu substitutions on Ga sites.

5.2.4 Considering strain in γ-Cu_9Ga_4 compounds

TEM investigations have revealed epitaxial growth of Cu_9Ga_4 compounds on GaN [231] which indicates the possibility of Cu_9Ga_4 being strained and thereby deviating from its cubic structure. This means that strained Cu_9Ga_4 could also be responsible for the XLD signal that has been observed. Therefore XANES and XLD spectra of strained Cu_9Ga_4 is also investigated. Different magnitudes of biaxial compressive strain have been considered ranging from 0.5% to 20%.

A change in the Cu_9Ga_4 structure is expected to influence the XANES spectrum at the Cu edge. Indeed, the shape of the graph and the main peak position changes with varying strain. Best agreement to the measured data is given in the range of 13 - 15% strain, which is a significant amount of strain and should be experimentally observable by e.g. XRD. However, XRD as well as in TEM measurements, where such a large strain of the compounds should be visible, show no indication of strain in the compounds within the measurement sensitivity.

A further indication that a contribution of strained Cu_9Ga_4 to the spectra is highly improbable is the increase of the XLD signal for the etched samples compared to the unetched ones, that has been discussed above and is depicted in Fig. 5.4. If strained Cu_9Ga_4 were responsible for a large part of the XLD signal, a decrease (rather than an increase) of XLD signal intensity after etching, due to partial removal of the Cu_9Ga_4 compounds, would be expected.

In addition to these arguments, XLD spectra of simulations were performed for up to 20% strained Cu_9Ga_4 to get an estimate of the influence on the XLD spectra of strained Cu_9Ga_4. The results are shown in Fig. 5.10 (a) and (c) together with the experimental data of sample C (b) for comparison. None of the calculated spectra is in good agreement with the experimental curve and hence the possibility of strained Cu_9Ga_4, also from this view point, is very small.

All these observations show that the presence of strain in Cu_9Ga_4, due to epitaxial growth on GaN, is negligible for the analysis of the presented data. However, in order to estimate the sensitivity of the fit presented in Fig. 5.8 on the shape of the simulated Cu_9Ga_4 spectrum, the experimental XANES spectrum at the Cu edge was fitted. Fig. 5.11 shows this fit considering 14% biaxial compressive strained Cu_9Ga_4. The change in Cu occupation distribution, with the best fit value given in brackets, is as follows: 0 - 10.6% (3.3%) for Cu on Ga, 0 - 0.5% (0.5%) for Cu on N, 0 - 7.7% (2.2%) for Cu on interstitial sites and 89.4 - 100% (93.9%) for Cu in metal compounds. Regarding Cu in the film only, this means that 54.5% is on Ga, 36.4% on interstitial and 9.1% on N sites. Introducing strain to the compound, the difference of Ga or interstitial site occupation plays a less important role for the shape of the graph.

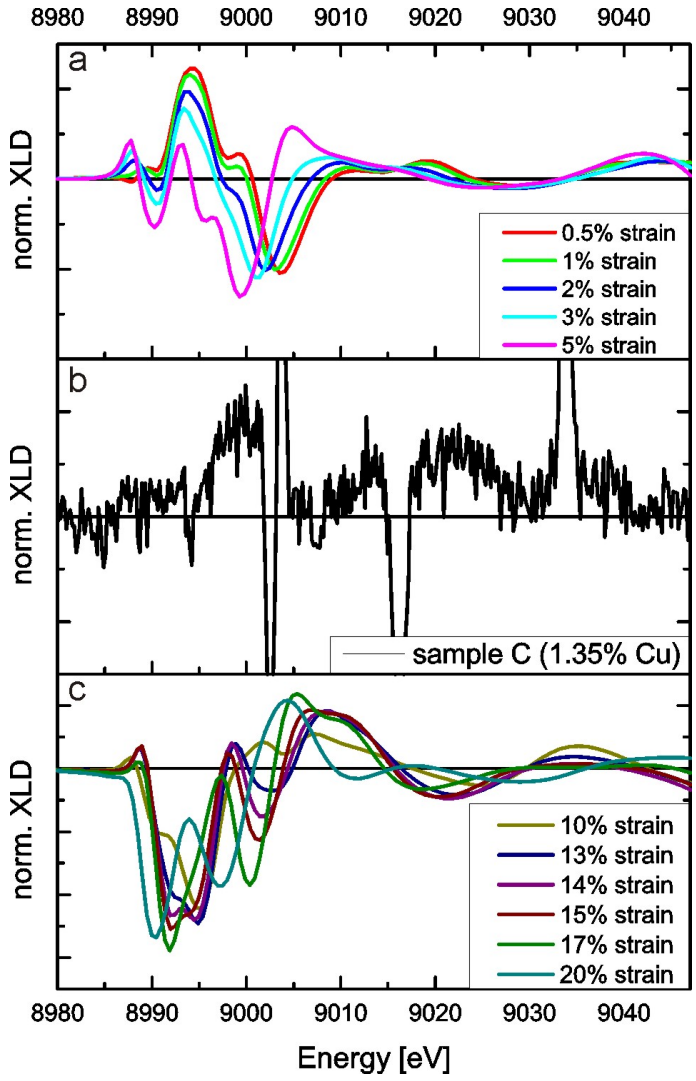

Figure 5.10: Comparison of the XLD signals of strained Cu_9Ga_4 (a) and (c) and the experimental curve (b) of sample C (1.35%) at the Cu K-edge. None of the calculated spectra correspond well with the experimental one, indicating the absence of strain in Cu_9Ga_4.

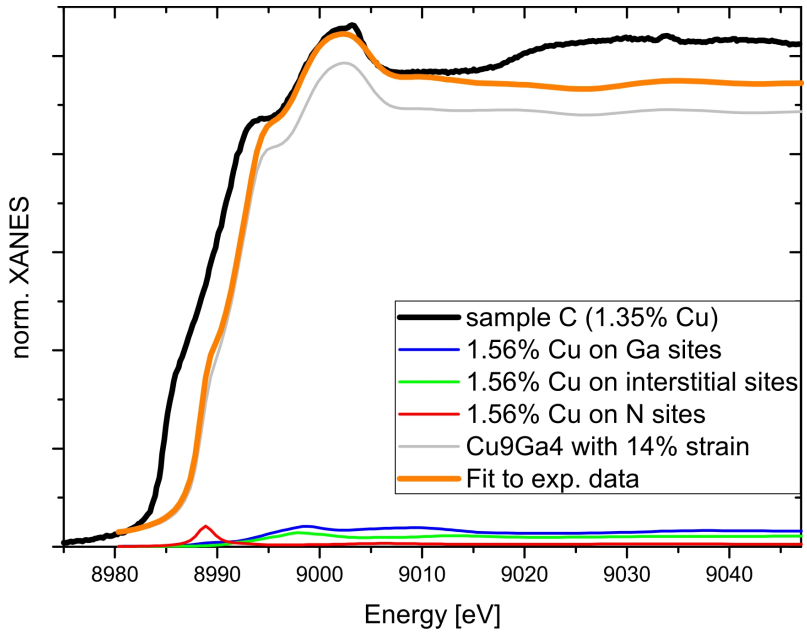

Figure 5.11: Fitting of the experimental XANES graph of sample C (1.35%) with different Cu site positions, where the Cu_9Ga_4 compounds are subject to 15% biaxial compressive strain.

Comparing the fitting results of the strained and unstrained scenario (Fig. 5.8 and 5.11), we find that in both cases mostly Ga positions are occupied by Cu, followed by interstitials and about 10% are present in N-like coordination. The values for Ga and interstitial site occupation are subject to a rather large error; however, because of the greatly differing shape of the spectrum for Cu atoms on N sites, this value is consistent in both scenarios.

5.3 Summary of the Cu incorporation study in GaN

A series of etched and unetched Cu-doped GaN samples with different doping concentrations have been investigated by XANES and XLD measurements to evaluate where Cu atoms are incorporated in the GaN matrix. The experimental data shows no apparent dependence on the nominal Cu concentration in the samples. The observed XLD signal at the Cu K-edge proves the incorporation of Cu in GaN and indicates that interstitial positions in GaN are occupied by Cu. The XANES spectra at the Cu K-edge are dominated by the signal coming from γ-Cu_9Ga_4 compounds. With the knowledge that the XANES spectra must also be affected by Cu present in GaN, a fit of the experimental XANES data was performed, taking into account a possible placement of Cu in the GaN crystal on Ga, N and interstitial sites. The

findings show that a large majority of the Cu atoms (∼70%) take Ga substitutional sites, about 20% can be found on interstitial and 10% on N sites. XLD simulations of GaN, with a Cu site occupation scenario as extracted with the help of the XANES spectra, compared to the experimental data confirm the results in a consistent way.

A contribution of strained Cu_9Ga_4 to the XLD signal is ruled out by a number of observations. The increase of XLD signal intensity after etching and the mismatch of simulated XLD spectra for strained Cu_9Ga_4 with the experimental data indicate the absence of strain in Cu_9Ga_4. This is also consistent with earlier XRD and TEM results, which found no indication of large strain in the compounds.

Although the findings here clearly point into a direction, one has to be cautious when attempting to generalize the results. We should keep in mind that the results apply for PAMBE grown samples in Ga rich conditions with certain provided Cu to Ga flux ratios under specific growth parameters. Because of the different techniques and methods available for the synthesis of Cu-doped GaN the present work states one step in studying this material. Investigations of different sample growth conditions (N rich condition) and sample treatments (post-growth annealing) are currently underway to get insight into the influence of these on the characteristics of GaN:Cu samples.

Nevertheless, the finding that a large fraction of Cu atoms in GaN occupies Ga sites supports the validity of theoretical studies based on this assumption. However, it has also been shown that a significant portion of dopants is situated on interstitial and nitrogen sites, giving rise to the question if and how these Cu atoms influence the magnetic behavior of GaN. To answer this question and to gain a more thorough understanding of the materials properties, future theoretical studies are encouraged to also consider Cu atoms on positions other than Ga sites, which are shown to be occupied in this work.

6 Summary

Within the framework of this thesis, a new MBE system dedicated to the growth of nitride semiconductors was built and brought to operation for room temperature spintronics applications such as spin LEDs. For such devices efficient recombination of charge carriers, high spin polarization, i.e. effective spin-alignment, as well as high spin-injection efficiencies are desirable. Therefore, incorporation of Cu in Cu-doped GaN, a room temperature ferromagnetic DMS, was studied and growth of non-polar GaN, leading to stronger emission efficiencies due to the absence of polarization charges along the growth direction, thereby avoiding the Quantum Confined Stark Effect, was investigated.

$LiAlO_2$ substrates were used to find appropriate growth conditions and parameters for non-polar GaN growth on the newly installed system. However, $LiGaO_2$ substrates were the main focus of this thesis, due to the promising impact of close lattice match of two different $LiGaO_2$ surface orientations to non-polar *M*- and *A*-plane GaN, respectively. Non-polar GaN growth on $LiGaO_2$ by MBE had not been investigated prior to this study.

Good quality GaN growth on $LiAlO_2$ substrates was accompanied by the presence of Ga droplets on the sample surface, which however, could easily be removed. *M*-plane GaN could be grown with very high purity and good crystal quality, comparable to the best reported results in literature. Furthermore, polar *C*-plane GaN could be achieved by alteration of the growth parameters, but growth of this GaN crystal direction was seen to be less suitable for growth on $LiAlO_2$. Nevertheless, 97.5% *C*-plane phase purity could be achieved with a crystal quality better than reported in literature for MBE grown *C*-plane GaN.

Growth of non-polar *M*- and *A*-plane GaN was studied on the well lattice matched substrate $LiGaO_2$. Depending on the selected $LiGaO_2$ substrate surface orientation, i.e. (100) or (010), *M*- or *A*-plane could be grown, respectively. Very high phase pure and flat non-polar GaN was grown. Dislocation densities were shown to be on the same order as comparable reported values. Stacking faults were found in high densities in the *M*-plane sample but were considerably less in the *A*-plane sample showing an improvement compared to reports in literature about stacking faults in *A*-plane GaN grown on *R*-plane sapphire.

The use of $LiAlO_2$ as a substrate for non-polar GaN benefits from the persistent investigations on this substrate over the past decade, meaning that manufacturing and surface polishing issues have been subject to a longer development and are more refined than for $LiGaO_2$, used for the first time to grow non-polar GaN in the context of this thesis. $LiGaO_2$ presents a very promising candidate for high phase purity and a flat and smooth morphology of the grown non-polar GaN planes. No Ga droplets were observed on the GaN surface; still good crystal quality was evident. However, the presence of scratches on the substrate surfaces indicated that polishing issues of $LiGaO_2$ are not completely solved yet.

Nevertheless, comparing non-polar GaN growth on $LiAlO_2$ and $LiGaO_2$, the latter seems to be a more convenient substrate for non-polar GaN growth, due to the high achievable phase purity which comes naturally, due to the selective lattice match of the different surfaces to GaN. However, progress on the matter of substrate polishing has to be made first, before the investigation of GaN growth on this substrate can yield higher crystal quality.

A prospective candidate for a room temperature spin-aligning material in spintronics applications Cu-doped GaN grown by MBE, was investigated with respect to the placement of Cu atoms in GaN by x-ray absorption. Simulations using the FDMNES program were performed in conjunction with the analysis of the experimental XANES and XLD data. The combination of experiment and calculations gives insight into the Cu incorporation in GaN. It was found that the majority (around 70%) of Cu in the GaN film is situated on Ga substitutional sites, roughly 20% is present on interstitial and 10% on N sites.

These results show that Cu is incorporated on Ga sites as assumed by theoretical studies and gives validity to those investigations. However, not only is Cu positioned on substitutional cation sites but also to some part on other sites in the crystal. Therefore, theoretical studies examining the magnetic behavior of GaN:Cu should also consider the Cu occupation of interstitial and nitrogen sites, which might yield insight into unraveling the mechanism of ferromagnetism in this material. In this sense, the findings presented here provide additional information which may serve to aid the understanding of the material of Cu-doped GaN.

In conclusion, for future work it would be very interesting to combine the benefits of non-polar GaN with the promising properties of Cu-doped GaN for efficient spintronics devices. Non-polar InGaN quantum dots imbedded in non-polar GaN, grown on (100) or (010) $LiGaO_2$ could serve as the active material in a spin LED, whereas a high degree of spin polarization and an efficient spin injection at room temperature could be realized by ferromagnetic Cu-doped GaN.

Bibliography

1. Awschalom, D. D. & Flatte, M. E. Challenges for semiconductor spintronics. English. *Nature Physics* **3,** 153–159. ISSN: 1745-2473 (2007).
2. Binasch, G., Grünberg, P., Saurenbach, F. & Zinn, W. Enhanced magnetoresistance in layered magnetic structures with antiferromagnetic interlayer exchange. *Physical Review B* **39,** 4828–4830 (1989).
3. Wolf, S. *et al.* Spintronics: A spin-based electronics vision for the future. English. *Science* **294,** 1488–1495. ISSN: 0036-8075 (2001).
4. Pearton, S. *et al.* Spintronics device concepts. *Circuits, Devices and Systems, IEE Proceedings* - **152,** 312 –322. ISSN: 1350-2409 (2005).
5. Morkoç, H. *Handbook of Nitride Semiconductors and Devices* (New York: Wiley-VCH, 2008).
6. Zorpette, G. *Let There Be Light* ¡http://spectrum.ieee.org/semiconductors/optoelectronics/let-there-be-light/1¿ (2002).
7. *GaN* ¡http://www.ostendo.com/gan/applications.php#leds¿ (2011).
8. Szweda, R. GaN and SiC detectors for radiation and medicine. *III-Vs Review* **18,** 40 –41. ISSN: 0961-1290 (2005).
9. *Panasonic develops a Gallium Nitride (GaN) terahertz detector with high sensitivity* ¡http://www.physorg.com/news196524107.html¿ (2010).
10. *Application of GaN* ¡http://www.nitronex.com/gan_applications.html¿.
11. Shealy, J. R. *et al.* An AlGaN/GaN high-electron-mobility transistor with an AlN sub-buffer layer. *Journal of Physics: Condensed Matter* **14,** 3499 (2002).
12. Manfra, M. J. *et al.* High mobility AlGaN/GaN heterostructures grown by plasma-assisted molecular beam epitaxy on semi-insulating GaN templates prepared by hydride vapor phase epitaxy. *Journal of Applied Physics* **92,** 338–345 (2002).
13. Waltereit, P. *et al.* Nitride semiconductors free of electrostatic fields for efficient white light-emitting diodes. *Nature* **406,** 865–868 (Aug. 2000).
14. Jansen, R. The spin-valve transistor: a review and outlook. *Journal of Physics D: Applied Physics* **36,** R289 (2003).

15. Schmidt, G., Ferrand, D., Molenkamp, L. W., Filip, A. T. & van Wees, B. J. Fundamental obstacle for electrical spin injection from a ferromagnetic metal into a diffusive semiconductor. *Physical Review B* **62,** R4790–R4793 (2000).

16. Dietl, T., Ohno, H., Matsukura, F., Cibert, J. & Ferrand, D. Zener model description of ferromagnetism in zinc-blende magnetic semiconductors. English. *Science* **287,** 1019–1022. ISSN: 0036-8075 (2000).

17. Wu, R. Q. *et al.* Cu-doped GaN: A dilute magnetic semiconductor from first-principles study. *Applied Physics Letters* **89,** 062505 (Aug. 2006).

18. Seong, H. K. *et al.* Room-temperature ferromagnetism in Cu doped GaN nanomores. *Nano Letters* **7,** 3366–3371 (Nov. 2007).

19. Yang, X. L. *et al.* Structural, optical, and magnetic properties of Cu-implanted GaN films. *Journal of Applied Physics* **105,** 053910 (Mar. 2009).

20. Ganz, P. R., Sürgers, C., Fischer, G. & Schaadt, D. M. Cu-doped GaN grown by molecular beam epitaxy. *Journal of Physics: Conference Series* **200,** 062006 (2010).

21. Joly, Y. X-ray absorption near-edge structure calculations beyond the muffin-tin approximation. *Physical Review B* **63,** 125120 (2001).

22. Baibich, M. N. *et al.* Giant Magnetoresistance of (001)Fe/(001)Cr Magnetic Superlattices. *Physical Review Letters* **61,** 2472–2475 (1988).

23. Pauli, W. *Wissenschaftlicher Briefwechsel Mit Bohr, Einstein, Heisenberg U.A. / Scientific Correspondence with Bohr, Einstein, Heisenberg A.O.* (ed Meyenn, K. V.) 1930-1939, 94 (Springer, 1985).

24. Liu, C., Yun, F. & Morkoç, H. Ferromagnetism of ZnO and GaN: A review. English. *Journal of Materials Science - Materials in Electronics* **16,** 555–597. ISSN: 0957-4522 (2005).

25. Datta, S. & Das, B. Electronic analog of the electro-optic modulator. *Applied Physics Letters* **56,** 665–667 (1990).

26. Bychkov, Y. A. & Rashba, E. I. Oscillatory effects and the magnetic susceptibility of carriers in inversion layers. *Journal of Physics C: Solid State Physics* **17,** 6039 (1984).

27. Schmidt, G. & Molenkamp, L. W. Spin injection into semiconductors, physics and experiments. *Semiconductor Science and Technology* **17,** 310 (2002).

28. Furdyna, J. K. Diluted magnetic semiconductors: An interface of semiconductor physics and magnetism (invited). *Journal of Applied Physics* **53,** 7637–7643 (1982).

29. Ohno, Y. *et al.* Electrical spin injection in a ferromagnetic semiconductor heterostructure. English. *Nature* **402,** 790–792. ISSN: 0028-0836 (1999).

30. Fiederling, R. *et al.* Injection and detection of a spin-polarized current in a light-emitting diode. English. *Nature* **402,** 787–790. ISSN: 0028-0836 (1999).

31. Furdyna, J. K., Samarth, N., Frankel, R. B. & Spalek, J. Static magnetic susceptibility of $Zn_{1-x}Mn_xSe$. *Physical Review B* **37,** 3707–3709 (1988).

32. Furdyna, J. K., Liu, X., Sasaki, Y., Potashnik, S. J. & Schiffer, P. Ferromagnetic III-Mn-V semiconductor multilayers: Manipulation of magnetic properties by proximity effects and interface design (invited). *Journal of Applied Physics* **91,** 7490–7495 (2002).

33. Löffler, W. *et al.* Doping and optimal electron spin polarization in n-ZnMnSe for quantum-dot spin-injection light-emitting diodes. *Applied Physics Letters* **96,** 052113 (2010).

34. Löffler, W. *et al.* Parallel preparation of highly spin-polarized electrons in single InAs/GaAs quantum dots. *Applied Physics Letters* **90,** 232105 (2007).

35. Hetterich, M. *et al.* in *Advances in Solid State Physics* (ed Haug, R.) 103–114 (Springer Berlin / Heidelberg, 2009). doi:10.1007/978-3-540-85859-1_9. ¡http://dx.doi.org/10.1007/978-3-540-85859-1_9¿.

36. Asshoff, P. *et al.* Spin-polarization dynamics in electrically excited single InGaAs quantum dots. *Journal of Physics: Conference Series* **200,** 062002 (2010).

37. Dagnelund, D. *et al.* Efficiency of optical spin injection and spin loss from a diluted magnetic semiconductor ZnMnSe to CdSe nonmagnetic quantum dots. *Physical Review B* **77,** 035437 (2008).

38. Ohno, H. Making nonmagnetic semiconductors ferromagnetic. English. *Science* **281,** 951–956. ISSN: 0036-8075 (1998).

39. Bastard, G., Rigaux, C. & Mycielski, A. Giant spin splitting induced by exchange interactions in $Hg_{1-k}Mn_kTe$ mixed crystals. *Physica Status Solidi (b)* **79,** 585–593. ISSN: 1521-3951 (1977).

40. Komarov, A., Ryabchenko, S., Terletskij, O., Zherou, I. & Ivanchouk, R. Magneto-Optical Investigations and Double Optico-Magnetic Resonance of Excition Band in CdTe-Mn^{2+}. Russian. *Zhurnal Eksperimentanoi i Teoreicheskoi Fiziki* **73,** 608–618. ISSN: 0044-4510 (1977).

41. Kossut, J. & Gaj, J. A. *Introduction to the Physics of Diluted Magnetic Semiconductors* 1st ed. (eds Kossut, J. & Gaj, J. A.) doi:10.1007/978-3-642-15856-8 (Springer, 2010).

42. Furdyna, J. K. Diluted magnetic semiconductors: Issues and opportunities. *Journal of Vacuum Science & Technology A: Vacuum, Surfaces, and Films* **4,** 2002–2009 (1986).

43. Furdyna, J. K. Diluted magnetic semiconductors. *Journal of Applied Physics* **64,** R29–R64 (1988).

44. Munekata, H. *et al.* Diluted magnetic III-V semiconductors. *Physical Review Letters* **63,** 1849–1852 (1989).

45. Ohno, H. *et al.* (Ga,Mn)As: A new diluted magnetic semiconductor based on GaAs. *Applied Physics Letters* **69,** 363–365 (1996).

46. Ohno, H., Munekata, H., von Molnár, S. & Chang, L. L. New III-V diluted magnetic semiconductors (invited). *Journal of Applied Physics* **69,** 6103–6108 (1991).

47. Chambers, S. & Farrow, R. New possibilities for ferromagnetic semiconductors. English. *MRS Bulletin* **28,** 729–733. ISSN: 0883-7694 (2003).

48. Jonker, B., Erwin, S., Petrou, A. & Petukhov, A. Electrical spin injection and transport in semiconductor spintronic devices. English. *MRS Bulletin* **28,** 740–748. ISSN: 0883-7694 (2003).

49. Macdonald, A., Schiffer, P. & Samarth, N. Ferromagnetic semiconductors: moving beyond (Ga, Mn)As. English. *Nature Materials* **4,** 195–202. ISSN: 1476-1122 (2005).

50. Bonanni, A. Ferromagnetic nitride-based semiconductors doped with transition metals and rare earths. *Semiconductor Science and Technology* **22,** R41 (2007).

51. Avrutin, V., Izyumskaya, N., Oandzguandr, U., Silversmith, D. & Morkoç and, H. Ferromagnetism in ZnO- and GaN-Based Diluted Magnetic Semiconductors: Achievements and Challenges. *Proceedings of the IEEE* **98,** 1288 – 1301. ISSN: 0018-9219 (2010).

52. Sato, K. *et al.* First-principles theory of dilute magnetic semiconductors. *Reviews of Modern Physics* **82,** 1633–1690 (2010).

53. Munekata, H. III-V based diluted magnetic semi conductors: Carrier-induced magnetism. *Advanced Materials* **7,** 82–85. ISSN: 1521-4095 (1995).

54. Nov´k, J. *et al.* Dependence of Curie temperature on surface strain in InMnAs epitaxial structures. *Applied Surface Science* **256.** Progress in Applied Surface, Interface and Thin Film Science - SURFINT SREN II, 5672 –5675. ISSN: 0169-4332 (2010).

55. May, S., Blattner, A., Eam, D. & Wessels, B. Direct observation of room temperature magnetism in (In,Mn)As thin films by magnetic force microscopy. *Applied Surface Science* **252,** 3509 –3513. ISSN: 0169-4332 (2006).

56. Telek, P. *et al.* Design, preparation and properties of spin-LED structures based on InMnAs, 175 –178 (2010).

57. Olejník, K. *et al.* Enhanced annealing, high Curie temperature, and low-voltage gating in (Ga,Mn)As: A surface oxide control study. *Physical Review B* **78,** 054403 (2008).

58. Jungwirth, T. *et al.* Prospects for high temperature ferromagnetism in (Ga,Mn)As semiconductors. *Physical Review B* **72,** 165204 (2005).

59. Sonoda, S., Shimizu, S., Sasaki, T., Yamamoto, Y. & Hori, H. Molecular beam epitaxy of wurtzite (Ga,Mn)N films on sapphire (0001) showing the ferromagnetic behaviour at room temperature. *Journal of Crystal Growth* **237-239,** 1358 –1362. ISSN: 0022-0248 (2002).

60. Song, C. *et al.* Giant magnetic moment in an anomalous ferromagnetic insulator: Co-doped ZnO. *Physical Review B* **73,** 024405 (2006).

61. Krenn, H. & Granitzer, P. Magnetische Halbleiter: Spintronik. *Physik in unserer Zeit* **33,** 218–225. ISSN: 1521-3943 (2002).

62. Zener, C. Interaction between the d Shells in the Transition Metals. *Physical Review* **81,** 440–444 (1951).

63. Zener, C. Interaction between the *d*-Shells in the Transition Metals. II. Ferromagnetic Compounds of Manganese with Perovskite Structure. *Physical Review* **82,** 403–405 (1951).

64. Ruderman, M. A. & Kittel, C. Indirect Exchange Coupling of Nuclear Magnetic Moments by Conduction Electrons. *Physical Review* **96,** 99 (1954).

65. Kasuya, T. A Theory of Metallic Ferro- and Antiferromagnetism on Zener's Model. *Progress of Theoretical Physics* **16,** 45–57 (1956).

66. Yosida, K. Magnetic Properties of Cu-Mn Alloys. *Physical Review* **106,** 893–898 (1957).

67. Coey, J., Venkatesan, M. & Fitzgerald, C. Donor impurity band exchange in dilute ferromagnetic oxides. English. *Nature Materials* **4,** 173–179. ISSN: 1476-1122 (2005).

68. Litvinov, V. I. & Dugaev, V. K. Ferromagnetism in Magnetically Doped III-V Semiconductors. *Physical Review Letters* **86,** 5593–5596 (2001).

69. Dhar, S., Brandt, O., Ramsteiner, M., Sapega, V. F. & Ploog, K. H. Colossal Magnetic Moment of Gd in GaN. *Physical Review Letters* **94,** 037205 (2005).

70. Khare, N., Kappers, M., Wei, M., Blamire, M. & MacManus-Driscoll, J. Defect-Induced Ferromagnetism in Co-doped ZnO. *Advanced Materials* **18,** 1449–1452. ISSN: 1521-4095 (2006).

71. Song, C. *et al.* Evidence of structural defect enhanced room-temperature ferromagnetism in Co-doped ZnO. *Journal of Physics: Condensed Matter* **19,** 176229 (2007).

72. Lee, K. J. *et al.* Magnetic properties of GaMnN grown via molecular beam epitaxy using a single precursor. *Physica Status Solidi (b)* **241,** 2854–2857. ISSN: 1521-3951 (2004).

73. Xu, X. H. *et al.* Carrier-induced ferromagnetism in n-type ZnMnAlO and ZnCoAlO thin films at room temperature. *New Journal of Physics* **8,** 135 (2006).

74. Kittilstved, K. R. *et al.* Direct Kinetic Correlation of Carriers and Ferromagnetism in Co^{2+}:ZnO. *Physical Review Letters* **97,** 037203 (2006).

75. Behan, A. J. *et al.* Two Magnetic Regimes in Doped ZnO Corresponding to a Dilute Magnetic Semiconductor and a Dilute Magnetic Insulator. *Physical Review Letters* **100,** 047206 (2008).

76. Dev, P., Xue, Y. & Zhang, P. Defect-Induced Intrinsic Magnetism in Wide-Gap III Nitrides. *Physical Review Letters* **100,** 117204 (2008).

77. Hong, J. Local magnetic moment induced by Ga vacancy defect in GaN. *Journal of Applied Physics* **103,** 063907 (2008).

78. Dhar, S. *et al.* Ferromagnetism and colossal magnetic moment in Gd-focused ion-beam-implanted GaN. *Applied Physics Letters* **89,** 062503 (2006).

79. Hsu, H. S. *et al.* Evidence of oxygen vacancy enhanced room-temperature ferromagnetism in Co-doped ZnO. *Applied Physics Letters* **88,** 242507 (2006).

80. Sun, L. *et al.* Structural, morphological, and magnetic characteristics of Cu-implanted nonpolar GaN films. English. *Applied Surface Science* **256,** 1361–1364. ISSN: 0169-4332 (2009).

81. Maruska, H. P. & Tietjen, J. J. The preparation and properties of vapor-deposited single-crystalline GaN. *Applied Physics Letters* **15,** 327–329 (1969).

82. Jena, D. *Conference talk at the International Conference for the Physics of Semiconductors (ICPS) in Seoul, Korea* 2010.

83. Krishnamurthy, S., van Schilfgaarde, M. & Newman, N. Spin lifetimes of electrons injected into GaAs and GaN. *Applied Physics Letters* **83,** 1761–1763 (2003).

84. Brown, J. *et al.* Fast spin relaxation in InGaN/GaN multiple quantum wells. *Physica Status Solidi (b)* **243,** 1643–1646 (2006).

85. Kuroda, T. *et al.* Subpicosecond exciton spin relaxation in GaN. *Applied Physics Letters* **85,** 3116–3118 (2004).

86. Tackeuchi, A. *et al.* No spin polarization of carriers in InGaN. *Physica E: Low-dimensional Systems and Nanostructures* **7,** 1011 –1014. ISSN: 1386-9477 (2000).

87. Julier, M. *et al.* Slow Spin Relaxation Observed in InGaN/GaN Multiple Quantum Wells. *Physica Status Solidi (b)* **216,** 341–345. ISSN: 1521-3951 (1999).

88. Buyanova, I. A. *et al.* On the origin of spin loss in GaMnN/InGaN light-emitting diodes. *Applied Physics Letters* **84,** 2599–2601 (2004).

89. Chen, W. M. *et al.* Efficient spin relaxation in InGaN/GaN and InGaN/GaMnN quantum wells: An obstacle to spin detection. *Applied Physics Letters* **87,** 192107 (2005).

90. Kyrychenko, F. V. *et al.* Investigation of a GaMnN/GaN/InGaN structure for spin LED. *AIP Conference Proceedings* **772,** 1319 –1320. ISSN: 0094243X (2005).

91. Nagahara, S., Arita, M. & Arakawa, Y. Long-lived electron spins in $In_xGa_{1-x}N$ multiquantum well. *Applied Physics Letters* **86,** 242103 (2005).

92. Nagahara, S., Arita, M. & Arakawa, Y. No temperature dependence of spin relaxation in InGaN phase-separated quantum dots. *Applied Physics Letters* **88,** 083101 (2006).

93. Gotoh, H., Ando, H., Kamada, H., Chavez-Pirson, A. & Temmyo, J. Spin relaxation of excitons in zero-dimensional InGaAs quantum disks. *Applied Physics Letters* **72,** 1341–1343 (1998).

94. Grandjean, N., Massies, J. & Leroux, M. Self-limitation of AlGaN/GaN quantum well energy by built-in polarization field. *Applied Physics Letters* **74,** 2361–2363 (1999).

95. Craven, M. D., Waltereit, P., Speck, J. S. & DenBaars, S. P. Well-width dependence of photoluminescence emission from a-plane GaN/AlGaN multiple quantum wells. *Applied Physics Letters* **84,** 496–498 (2004).

96. Overberg, M. E. *et al.* Indication of ferromagnetism in molecular-beam-epitaxy-derived N-type GaMnN. *Applied Physics Letters* **79,** 1312–1314 (2001).

97. Thaler, G. T. *et al.* Magnetic properties of n-GaMnN thin films. *Applied Physics Letters* **80,** 3964–3966 (2002).

98. Dhar, S. *et al.* Origin of high-temperature ferromagnetism in (Ga,Mn)N layers grown on 4H-SiC(0001) by reactive molecular-beam epitaxy. *Applied Physics Letters* **82,** 2077–2079 (2003).

99. Sasaki, T. *et al.* Magnetic and transport characteristics on high Curie temperature ferromagnet of Mn-doped GaN. *Journal of Applied Physics* **91,** 7911–7913 (2002).

100. Bither, T. A. & Cloud, W. H. Magnetic Tetragonal delta Phase in the Mn-Ga Binary. *Journal of Applied Physics* **36,** 1501–1502 (1965).

101. Takei, W. J., Shirane, G. & Frazer, B. C. Magnetic Structure of Mn_4N. *Physical Review* **119,** 122–126 (1960).

102. Yang, H., Al-Brithen, H., Trifan, E., Ingram, D. C. & Smith, A. R. Crystalline phase and orientation control of manganese nitride grown on MgO(001) by molecular beam epitaxy. *Journal of Applied Physics* **91,** 1053–1059 (2002).

103. Ando, K. Magneto-optical studies of s,p-d exchange interactions in GaN:Mn with room-temperature ferromagnetism. *Applied Physics Letters* **82,** 100–102 (2003).

104. Baik, J. M., Jang, H. W., Kim, J. K. & Lee, J.-L. Effect of microstructural change on magnetic property of Mn-implanted p-type GaN. *Applied Physics Letters* **82,** 583–585 (2003).

105. Theodoropoulou, N. *et al.* Magnetic and structural properties of Mn-implanted GaN. *Applied Physics Letters* **78,** 3475–3477 (2001).

106. Chitta, V. A. *et al.* Room temperature ferromagnetism in cubic GaN epilayers implanted with Mn^+ ions. *Applied Physics Letters* **85,** 3777–3779 (2004).

107. Reed, M. L. *et al.* Room temperature ferromagnetic properties of (Ga, Mn)N. *Applied Physics Letters* **79,** 3473–3475 (2001).

108. Yang, X. L. *et al.* Positron annihilation in (Ga, Mn)N: A study of vacancy-type defects. *Applied Physics Letters* **94,** 151907 (2009).

109. Potzger, K. & Zhou, S. Non-DMS related ferromagnetism in transition metal doped zinc oxide. *Physica Status Solidi (b)* **246,** 1147–1167. ISSN: 1521-3951 (2009).

110. Leuenberger, F. *et al.* X-ray magnetic circular dichroism at the Gd $L_{2,3}$ absorption edges in GdN layers: The influence of lattice expansion. *Physical Review B* **73,** 214430 (2006).

111. Iwata, N., Okamoto, T. & E., T. Variation of Cuire temperature with hydrostatic pressure and anomalous compressibility on Gd. English. *Journal of the physical society of Japan* **24,** 948–&. ISSN: 0031-9015 (1968).

112. Rogalev, A., Wilhelm, F., Jaouen, N., Goulon, J. & Kappler, J.-P. X-ray magnetic circular dichroism: Historical perspective and recent highlights. *Lecture Notes in Physics* **697** (eds Beaurepaire, E, Bulou, H, Scheurer, F & Kappler, J.) 4th Mittelwihr School on Magnetism and Synchrotron Radiation, Mittelwihr, France, Oct 10-15, 2004, 71–93. ISSN: 0075-8450 (2006).

113. Ney, A. *et al.* Gd-doped GaN studied with element specificity: Very small polarization of Ga, paramagnetism of Gd and the formation of magnetic clusters. *Journal of Magnetism and Magnetic Materials* **322.** Proceedings of the Joint European Magnetic Symposia, 1162 –1166. ISSN: 0304-8853 (2010).

114. Rosa, A. L. & Ahuja, R. Weak ferromagnetism in Cu-doped GaN. *Applied Physics Letters* **91,** 232109 (Dec. 2007).

115. Lee, S. C., Choi, J. H., Lee, K. R. & Cha, P. R. Origin of Ferromagnetism and Long-range Interactions of Cu in GaN: Chemical Bonding and Electronegativity Approaches. *Journal of The Korean Physical Society* **55,** 1013–1017 (Sept. 2009).

116. Lee, J. H. *et al.* Room-temperature ferromagnetism of Cu-implanted GaN. *Applied Physics Letters* **90,** 032504 (Jan. 2007).

117. Ganz, P. R., Fischer, G., Sürgers, C. & Schaadt, D. M. Cu-doped nitrides: Promising candidates for a nitride based spin-aligner. *Journal of Crystal Growth* **323,** 355–358 (Oct. 2010).

118. Madhu, C., Sundaresan, A. & Rao, C. N. R. Room-temperature ferromagnetism in undoped GaN and CdS semiconductor nanoparticles. *Physical Review B* **77,** 201306 (2008).

119. Sun, L. L. *et al.* The impact of implantation dose on the characteristics of diluted-magnetic nonpolar GaN:Cu films. *Materials Letters* **63,** 2574–2576 (Dec. 2009).

120. Sun, L. L. *et al.* Strong room-temperature ferromagnetism in Cu-implanted nonpolar GaN films. *Journal of Applied Physics* **106,** 113921 (Dec. 2009).

121. Elsayed, M. *et al.* Cu diffusion-induced vacancy-like defects in freestanding GaN. *New Journal of Physics* **13,** 013029 (2011).

122. *Wurtzite crystal structure of with coordination polyhedra* ¡`http://upload.wikimedia.org/wikipedia/commons/8/8e/Wurtzite_polyhedra.png`¿ (2008).

123. Chèze, C. *Conference talk at the 16th European Molecular Beam Epitaxy Conference (Euro MBE) in L'Alp d'Huez, France.* 2011.

124. Leszczynski, M. *et al.* Lattice parameters of gallium nitride. *Applied Physics Letters* **69,** 73–75 (1996).

125. Roder, C., Einfeldt, S., Figge, S. & Hommel, D. Temperature dependence of the thermal expansion of GaN. *Physical Review B* **72,** 085218 (2005).

126. Monemar, B. Fundamental energy gap of GaN from photoluminescence excitation spectra. *Physical Review B* **10,** 676–681 (1974).

127. Bougrov, V., Levinshtein, M., Rumyanstev, S. & Zbrilov, A. *Properties of Advanced Semiconductor Materials* (eds Levinshtein, M. E., Rumyantsev, S. & Shur, M. S.) (Wiley & Sons, 2001).

128. Harafuji, K., Tsuchiya, T. & Kawamura, K. Molecular dynamics simulation for evaluating melting point of wurtzite-type GaN crystal. *Journal of Applied Physics* **96,** 2501–2512 (2004).

129. Kucheyev, S. O. *et al.* Nanoindentation of epitaxial GaN films. *Applied Physics Letters* **77,** 3373–3375 (2000).

130. Polian, A., Grimsditch, M. & Grzegory, I. Elastic constants of gallium nitride. *Journal of Applied Physics* **79,** 3343–3344 (1996).

131. Monemar, B. *et al.* Recombination of free and bound excitons in GaN. *Physica Status Solidi (b)* **245,** 1723–1740. ISSN: 1521-3951 (2008).

132. Bernardini, F., Fiorentini, V. & Vanderbilt, D. Spontaneous polarization and piezoelectric constants of III-V nitrides. *Physical Review B* **56,** R10024–R10027 (1997).

133. Leroux, M. *et al.* Quantum confined Stark effect due to built-in internal polarization fields in (Al,Ga)N/GaN quantum wells. *Physical Review B* **58,** R13371–R13374 (1998).

134. Bernardini, F. & Fiorentini, V. Macroscopic polarization and band offsets at nitride heterojunctions. *Physical Review B* **57,** R9427–R9430 (1998).

135. Sun, Y.-J. *Growth and Characterization of M-plane GaN and (In,Ga)N/GaN multiple quantum wells* PhD thesis (Humboldt-Universität zu Berlin, 2004).

136. Lei, T. *et al.* Epitaxial growth of zinc blende and wurtzitic gallium nitride thin films on (001) silicon. *Applied Physics Letters* **59,** 944–946 (1991).

137. Powell, R. C., Lee, N.-E., Kim, Y.-W. & Greene, J. E. Heteroepitaxial wurtzite and zinc-blende structure GaN grown by reactive-ion molecular-beam epitaxy: Growth kinetics, microstructure, and properties. *Journal of Applied Physics* **73,** 189–204 (1993).

138. Romanov, A. E., Baker, T. J., Nakamura, S., Speck, J. S. & Group, E. U. Strain-induced polarization in wurtzite III-nitride semipolar layers. *Journal of Applied Physics* **100,** 023522 (2006).

139. Waltereit, P. *et al.* Growth of M-plane GaN ($1\bar{1}00$): A way to evade electrical polarization in nitrides. *Physica Status Solidi A-Applied Research* **180,** 133–138 (July 2000).

140. Nakamura, S. & Fasol, G. *The Blue Lase Diode* (Springer, 1997).

141. Johnson, W. C., Parson, J. B. & Crew, M. C. Nitrogen Compounds of Gallium. III. *The Journal of Physical Chemistry* **36,** 2651–2654 (1932).

142. Nakamura, S., Mukai, T. & Senoh, M. Candela-class high-brightness InGaN/AlGaN double-heterostructure blue-light-emitting diodes. *Applied Physics Letters* **64,** 1687–1689 (1994).

143. Roussel, P. *Bulk GaN Market* 2009. ¡\url{http://www.i-micronews.com/upload/Rapports/yole_flyer_report_cs_BulK\%20GaN_web.pdf}¿.

144. Brandt, M. S., Johnson, N. M., Molnar, R. J., Singh, R. & Moustakas, T. D. Hydrogenation of p-type gallium nitride. *Applied Physics Letters* **64,** 2264–2266 (1994).

145. Zavada, J. M., Wilson, R. G., Abernathy, C. R. & Pearton, S. J. Hydrogenation of GaN, AlN, and InN. *Applied Physics Letters* **64,** 2724–2726 (1994).

146. Akasaki, I., Amano, H., Kito, M. & Hiramatsu, K. Photoluminescence of Mg-doped p-type GaN and electroluminescence of GaN p-n junction LED. *Journal of Luminescence* **48-49,** 666 –670. ISSN: 0022-2313 (1991).

147. Tanaka, T. *et al.* p-type conduction in Mg-doped GaN and $Al_{0.08}Ga_{0.92}N$ grown by metalorganic vapor phase epitaxy. *Applied Physics Letters* **65,** 593–594 (1994).

148. Götz, W., Johnson, N. M., Walker, J., Bour, D. P. & Street, R. A. Activation of acceptors in Mg-doped GaN grown by metalorganic chemical vapor deposition. *Applied Physics Letters* **68,** 667–669 (1996).

149. Kim, W. *et al.* Mg-doped p-type GaN grown by reactive molecular beam epitaxy. *Applied Physics Letters* **69,** 559–561 (1996).

150. Nakayama, H. *et al.* Electrical Transport Properties of p-GaN. *Japanese Journal of Applied Physics* **35,** L282–L284 (1996).

151. Eiting, C., Grudowski, P. & Dupuis, R. Growth of low resistivity p-type GaN by metal organic chemical vapour deposition. English. *Electronics Letters* **33,** 1987–1989. ISSN: 0013-5194 (1997).

152. Monemar, B., Lagerstedt, O. & Gislason, H. P. Properties of Zn-doped VPE-grown GaN. I. Luminescence data in relation to doping conditions. *Journal of Applied Physics* **51,** 625–639 (1980).

153. Polyakov, A. Y. *et al.* Electrical and optical properties of modulation-doped p-AlGaN/GaN superlattices. *Applied Physics Letters* **79,** 4372–4374 (2001).

154. Simon, J., Protasenko, V., Lian, C., Xing, H. & Jena, D. Polarization-Induced Hole Doping in WideBand-Gap Uniaxial Semiconductor Heterostructures. *Science* **327,** 60–64 (2010).

155. Nath, D. N., Gür, E., Ringel, S. A. & Rajan, S. Molecular beam epitaxy of N-polar InGaN. *Applied Physics Letters* **97,** 071903 (2010).

156. Sawaki, N. *et al.* Selective growth and impurity incorporation in semipolar GaN grown on Si substrate. *Gallium Nitride Materials and Devices V* **7602** (eds Chyi, J.-I. *et al.*) 760203 (2010).

157. Liu, L. & Edgar, J. H. Substrates for gallium nitride epitaxy. *Materials Science & Engineering R-Reports* **37,** 61–127 (Apr. 2002).

158. Neumann, W. *et al.* Structure investigations of nonpolar GaN layers. *Journal of Microscopy-Oxford* **237,** 308–313. ISSN: 0022-2720 (2010).

159. Shih, C.-H. *et al.* Microstructure of non-polar GaN on $LiGaO_2$ grown by plasma-assisted MBE. *accepted in Nanoscale Research Letters.* ¡\url{http://www.nanoscalereslett.com/imedia/1001019518468975_article.pdf}¿ (2011).

160. Craven, M. D., Lim, S. H., Wu, F., Speck, J. S. & DenBaars, S. P. Structural characterization of nonpolar $(11\bar{2}0)$ a-plane GaN thin films grown on $(1bar102)$ r-plane sapphire. *Applied Physics Letters* **81,** 469–471 (2002).

161. Haskell, B. A. *et al.* Structural and morphological characteristics of planar $(11\bar{2}0)$ a-plane gallium nitride grown by hydride vapor phase epitaxy. *Applied Physics Letters* **83,** 1554–1556 (2003).

162. Wagner, B. *et al.* Growth and characterization of pendeo-epitaxial GaN $(11\bar{2}0)$ on 4H-SiC $(11\bar{2}0)$ substrates. *Journal of Crystal Growth* **290,** 504 –512. ISSN: 0022-0248 (2006).

163. Sun, Q. *et al.* Microstructural evolution in m-plane GaN growth on m-plane SiC. *Applied Physics Letters* **92,** 051112 (2008).

164. Sun, Y. *et al.* Impact of nucleation conditions on the structural and optical properties of M-plane GaN $(1\bar{1}00)$ grown on γ-$LiAlO_2$. *Journal of Applied Physics* **92,** 5714–5719. ISSN: 0021-8979 (2002).

165. Zou, J. & Xiang, W. Nonpolar m- and a-plane GaN thin films grown on γ-$LiAlO_2$ substrates. *Journal of Crystal Growth* **311,** 3285 –3288. ISSN: 0022-0248 (2009).

166. Chen, C. Q. *et al.* GaN homoepitaxy on freestanding $(1\bar{1}00)$ oriented GaN substrates. *Applied Physics Letters* **81,** 3194–3196 (2002).

167. Wernicke, T. *et al.* Surface morphology of homoepitaxial GaN grown on non- and semipolar GaN substrates. *Physica Status Solidi (b)* **248,** 574–577. ISSN: 1521-3951 (2011).

168. Ambacher, O. Growth and applications of Group III-nitrides. *Journal of Physics D: Applied Physics* **31,** 2653 (1998).

169. Marezio, M. Crystal structure and anomalous dispersion of γ-$LiAlO_2$. *Acta Crystallographica* **19,** 396–& (1965).

170. Cockayne, B. & Lent, B. The Czochralski growth of single crystal lithium aluminate, $LiAlO_2$. *Journal of Crystal Growth* **54,** 546 –550. ISSN: 0022-0248 (1981).

171. Marezio, M. Crystal structure of $LiGaO_2$. English. *Acta Crystallographica* **18,** 481–&. ISSN: 0108-7673 (1965).

172. Rawn, C. J. & Chaudhuri, J. High temperature X-ray diffraction study of $LiGaO_2$. *Journal of Crystal Growth* **225,** 214 –220. ISSN: 0022-0248 (2001).

173. Matyi, R. J., Doolittle, W. A. & Brown, A. S. High resolution x-ray diffraction analyses of GaN/$LiGaO_2$. *Journal of Physics D-Applied Physics* **32,** A61–A64 (May 1999).

174. Ichimiya, A. & Cohen, P. I. *Reflection High-Energy Electron Diffraction* (Cambridge University Press, 2004).

175. Koblmüller, G., Fernández-Garrido, S., Calleja, E. & Speck, J. S. In situ investigation of growth modes during plasma-assisted molecular beam epitaxy of (0001) GaN. *Applied Physics Letters* **91,** 161904 (2007).

176. Waltereit, P. *et al.* Growth of M-plane GaN ($1\bar{1}00$) on γ-$LiAlO_2$ (100). *Journal of Crystal Growth* **218,** 143 –147. ISSN: 0022-0248 (2000).

177. Hellman, E. S., Liliental-Weber, Z. & Buchanan, D. N. E. Epitaxial Growth and Orientation of GaN on (100) γ-$LiAlO_2$. *M R S Internet Journal of Nitride Semiconductor Research* **2,** article 30 (1997).

178. Sun, Y. J., Brandt, O. & Ploog, K. H. Growth of M-plane GaN films on γ-$LiAlO_2$ (100) with high phase purity. *Journal of Vacuum Science and Technology B* **21,** 1350 (2003).

179. Gerlach, J. W. *et al.* High-quality m-plane GaN thin films deposited on γ-$LiAlO_2$ by ion-beam-assisted molecular-beam epitaxy. *Applied Physics Letters* **88,** 011902 (2006).

180. Jun, Z. *et al.* Growth studies of m-GaN layers on $LiAlO_2$ by MOCVD. English. *Chinese Physics* **15,** 2706–2709. ISSN: 1009-1963 (2006).

181. Czochralski, J. Ein neues Verfahren zur Messung der Kristallisations-geschwindigkeit der Metalle. *Zeitschrift für Physikalische Chemie* **92,** 219–221 (1918).

182. Mogilatenko, A. *et al.* Mechanism of $LiAlO_2$ decomposition during the GaN growth on (100) γ-$LiAlO_2$. *Journal of Applied Physics* **102,** 023519 (2007).

183. Hsu, C. *et al.* Wet chemical etching of $LiGaO_2$ and $LiAlO_2$. English. *Electrochemical and Solid State Letters* **4,** C35–C38. ISSN: 1099-0062 (2001).

184. Hsu, C. *et al.* Photoluminescence studies of GaN epilayer-nanocrystals grown on γ-$LiAlO_2$ substrate. *Physica E: Low-dimensional Systems and Nanostructures* **40.** 13th International Conference on Modulated Semiconductor Structures, 1971 –1974. ISSN: 1386-9477 (2008).

185. Lo, I. *et al.* Line defects of M-plane GaN grown on γ-$LiAlO_2$ by plasma-assisted molecular beam epitaxy. *Applied Physics Letters* **92,** 202106 (2008).

186. Lo, I., Hsieh, C.-H., Hsu, Y.-C., Pang, W.-Y. & Chou, M.-C. Self-assembled GaN hexagonal micropyramid and microdisk. *Applied Physics Letters* **94,** 062105 (2009).

187. Widmann, F., Feuillet, G., Daudin, B. & Rouvière, J. L. Low temperature sapphire nitridation: A clue to optimize GaN layers grown by molecular beam epitaxy. *Journal of Applied Physics* **85,** 1550–1555 (1999).

188. Namkoong, G. *et al.* The impact of substrate nitridation temperature and buffer design and synthesis on the polarity of GaN epitaxial films. *Journal of Crystal Growth* **252,** 159 –166. ISSN: 0022-0248 (2003).

189. Telieps, W. & Bauer, E. The (7×7) <-> (1×1) phase transition on Si(111). *Surface Science* **162,** 163 –168. ISSN: 0039-6028 (1985).

190. Cheng, A.-T., Su, Y.-K., Lai, W.-C. & Chen, Y.-Z. Metalorganic Vapor Phase Epitaxy Growth of *m*-Plane GaN Using $LiAlO_2$ Substrates. *Japanese Journal of Applied Physics* **47,** 3074–3076 (2008).

191. Hang, D., Chou, M. M., Chang, L., Dikme, Y. & Heuken, M. Growth and characterization of m-plane GaN-based layers on $LiAlO_2$ (100) grown by MOVPE. *Journal of Crystal Growth* **311.** The Proceedings of the 4th International Asian Conference on Crystal Growth and Crystal Technology, 452 –455. ISSN: 0022-0248 (2009).

192. Chou, M. M. *et al.* Growth behavior of nonpolar GaN on the nearly lattice-matched (100) γ-$LiAlO_2$ substrate by chemical vapor deposition. *Journal of Crystal Growth* **311.** The Proceedings of the 4th International Asian Conference on Crystal Growth and Crystal Technology, 448 –451. ISSN: 0022-0248 (2009).

193. Reed, M., Kryliouk, O., Mastro, M. & Anderson, T. Growth and characterization of single-crystalline gallium nitride using (100) $LiAlO_2$ substrates. *Journal of Crystal Growth* **274,** 14 –20. ISSN: 0022-0248 (2005).

194. Mogilatenko, A. *et al.* English. in *Physica Status Solidi (c) - Current topics in solid state physics, vol 5, no 12 2008* (ed Stutzmann, M) **5** (2008), 3712–3715.

195. Richter, E. *et al.* Freestanding two inch c-plane GaN layers grown on (100) γ-lithium aluminium oxide by hydride vapour phase epitaxy. *physica status solidi (c)* **3,** 1439–1443. ISSN: 1610-1642 (2006).

196. Richter, E. *et al.* Optimization of HVPE growth of freestanding c-plane GaN layers using (100) γ-$LiAlO_2$ substrates. *physica status solidi (c)* **4,** 2277–2280. ISSN: 1610-1642 (2007).

197. Losurdo, M. *et al.* The surface modification and reactivity of $LiGaO_2$ substrates during GaN epitaxy. *Journal of Crystal Growth* **264,** 139–149 (Mar. 2004).

198. Balakrishnan, K, Okumura, H & Yoshida, S. Study on the initial stages of heteroepitaxial growth of hexagonal GaN on sapphire by plasma assisted MBE. English. *Journal of Crystal Growth* **190,** 244–249. ISSN: 0022-0248 (1998).

199. Ishii, T., Tazoh, Y. & Miyazawa, S. Single-crystal growth of $LiGaO_2$ for a substrate of GaN thin films. *Journal of Crystal Growth* **186,** 409–419 (Mar. 1998).

200. Johnson, M. A. L. *et al.* Growth of GaN, InGaN, and AlGaN films and quantum well structures by molecular beam epitaxy. *Journal of Crystal Growth* **175-176,** 72 –78. ISSN: 0022-0248 (1997).

201. Kung, P. *et al.* Metalorganic chemical vapor deposition of monocrystalline GaN thin films on β-$LiGaO_2$ substrates. *Applied Physics Letters* **69,** 2116–2118 (1996).

202. Kryliouk, O. *et al.* MOCVD growth of GaN films on lattice-matched oxide substrates. *Materials Research Society Symposium Proceedings* **449** (eds Ponce, F., Moustakas, T., Akasaki, I & Monemar, B.) Symposium on III-V Nitrides, Boston, Dec 02-06, 1996, 123–128. ISSN: 0272-9172 (1997).

203. Nicholls, J. *et al.* Growth and optical properties of GaN grown by MBE on novel lattice-matched oxide substrates. *Materials Research Society Symposium Proceedings* **395** (eds Ponce, F., Dupuis, R., Nakamura, S & Edmond, J.) 1st International Symposium on Gallium Nitride and Related Materials, Boston, Nov 27-Dec 01, 1995, 535–539. ISSN: 0272-9172 (1996).

204. Tazoh, Y., Ishii, T. & Miyazawa, S. GaN Thin Film Growth on $LiGaO_2$ Substrate with a Multi-Domain Structure. *Japanese Journal of Applied Physics* **36,** L746–L749 (1997).

205. Andrianov, A. *et al.* Photoluminescence from GaN films grown by MBE on $LiGaO_2$ substrate. English. *Semiconductor Science and Technology* **12,** 59–63. ISSN: 0268-1242 (1997).

206. Doolittle, W. A. *et al.* MBE growth of high quality GaN on $LiGaO_2$. *Journal of Electronic Materials* **27,** L58–L60 (Aug. 1998).

207. Okada, M. *et al.* ECR-MBE growth of GaN on $LiGaO_2$. *Journal of Crystal Growth* **189-190,** 213 –217. ISSN: 0022-0248 (1998).

208. Seo, S. W. *et al.* GaN metal-semiconductor-metal photodetectors grown on lithium gallate substrates by molecular-beam epitaxy. *Applied Physics Letters* **79,** 1372–1374 (2001).

209. Duan, S. K., Teng, X. G., Han, P. D. & Lu, D. C. Growth and characterization of GaN on $LiGaO_2$. *Journal of Crystal Growth* **195,** 304–308 (Dec. 1998).

210. Pohl, U., Knorr, K. & Blsing, J. Metalorganic Vapor Phase Epitaxy of GaN on $LiGaO_2$ Substrates Using Tertiarybutylhydrazine. *Physica Status Solidi (a)* **184,** 117–120. ISSN: 1521-396X (2001).

211. Kang, S. *et al.* Characterization of AlGaN/GaN structures on various substrates grown by radio frequency-plasma assisted molecular beam epitaxy. English. *Journal of Electronic Materials* **30,** 156–161. ISSN: 0361-5235 (2001).

212. Takahashi, H., Fujioka, H., Ohta, J., Oshima, M. & Kimura, M. Structural properties of GaN grown on $LiGaO_2$ by PLD. *Journal of Crystal Growth* **259,** 36 –39. ISSN: 0022-0248 (2003).

213. Sakurada, K., Kobayashi, A., Kawaguchi, Y., Ohta, J. & Fujioka, H. Low temperature epitaxial growth of GaN films on $LiGaO_2$ substrates. *Applied Physics Letters* **90,** 211913 (2007).

214. Kisailus, D. & Lange, F. F. Growth of epitaxial GaN on $LiGaO_2$ substrates via a reaction with ammonia. *Journal of Materials Research* **16,** 2077–2081 (July 2001).

215. Nanamatsu, S., Doi, K. & Takahashi, M. Piezoelectric, Elastic and Dielectric Properties of $LiGaO_2$. *Japanese Journal of Applied Physics* **11,** 816–822 (1972).

216. Neumann, H., Pirl, E. & Kuhn, G. Thermal-Expansion of $LiGaO_2$. English. *Journal of Materals Science Letters* **6,** 495–496. ISSN: 0261-8028 (1987).

217. Ishii, T., Tazoh, Y. & Miyazawa, S. $LiGaO_2$ single crystal as a lattice-matched substrate for hexagonal GaN thin films. *Journal of Crystal Growth* **189-190,** 208 –212. ISSN: 0022-0248 (1998).

218. Doolittle, W. A. *et al.* Growth of GaN on lithium gallate substrates for development of a GaN thin compliant substrate. *Papers from the 16th north american conference on molecular-beam epitaxy* **16,** 1300–1304 (1998).

219. Chou, M. *private communication* 2010.

220. Armitage, R., Horita, M., Suda, J. & Kimoto, T. m-plane GaN layers grown by rf-plasma assisted molecular beam epitaxy with varying Ga/N flux ratios on m-plane 4H-SiC substrates. *Journal of Applied Physics* **101,** 033534 (2007).

221. Schaadt, D., Brandt, O., Trampert, A., Schönherr, H.-P. & Ploog, K. Epitaxial growth of 6H-AlN on M-plane SiC by plasma-assisted molecular beam epitaxy. *Journal of Crystal Growth* **300.** First International Symposium on Growth of Nitrides - ISGN-1, 127 –129. ISSN: 0022-0248 (2007).

222. Shih, C.-H., Lo, I., Pang, W.-Y., Wang, Y.-C. & Chou, M. M. Characterization of M-plane GaN film grown on β-$LiGaO_2$ (100) by plasma-assisted molecular beam epitaxy. *Thin Solid Films* **519,** 3569 –3572. ISSN: 0040-6090 (2011).

223. Liliental-Weber, Z., Jasinski, J. & Zakharov, D. GaN grown in polar and non-polar directions. *Opto-Electron. Rev.* **12,** 339–346 (2004).

224. Rajpalke, M. K. *et al.* Structural and optical properties of nonpolar $(11\bar{2}0)$ a-plane GaN grown on $(1\bar{1}02)$ r-plane sapphire substrate by plasma-assisted molecular beam epitaxy. *Scripta Materialia* **In Press, Corrected Proof,** –. ISSN: 1359-6462 (2011).

225. Ran, F.-Y., Subramanian, M., Tanemura, M., Hayashi, Y. & Hihara, T. Ferromagnetism in Cu-doped AlN films. *Applied Physics Letters* **95,** 112111 (2009).

226. Kang, B. S., Heo, C. M., Lyu, K. K. & Yu, S. C. First-principles Study on Magnetism of Cu in GaN. *Journal of Magnetics* **14,** 114–116 (Sept. 2009).

227. Newville, M. *Fundamentals of XAFS* tech. rep. (Consortium for Advanced Radiation Sources, University of Chicago, Chicago, IL, 2004).

228. Wilhelm, F. *et al.* Hard X-ray Linear Dichroism Using a Quarter Wave Plate for Structural Characterization of Diluted Magnetic Semiconductors. *AIP Conference Proceedings* **879,** 1675–1678 (2007).

229. Sarigiannidou, E. *et al.* Intrinsic ferromagnetism in wurtzite (Ga,Mn)N semiconductor. *Physical Review B* **74,** 041306 (2006).

230. Stokhuyzen, R., Brandon, J. K., Chieh, P. C. & Pearson, W. B. Copper-gallium, γCu_9Ga_4. *Acta Crystallographica Section B* **30,** 2910–2911 (1974).

231. Chang, L., Huang, T. H., Ganz, P. R. & M., S. D. *Formation mechanism of islands on Cu-alloyed GaN grown by plasma assisted molecular beam epitaxy* submitted to Journal of the Electrochemical Society. 2011.

232. Stöhr, J. & Siegmann, H. *Magnetism: From Fundamentals to Nanoscale Dynamics* (Springer Berlin, 2006).

233. *The Landholt-Börnstein Database* ¡`http://www.springermaterials.com/docs/pdf/10086090_1074.html`¿.

234. Li, J.-B. *et al.* A thermodynamic assessment of the copper-gallium system. *Calphad* **32,** 447 –453. ISSN: 0364-5916 (2008).

235. Hersh, H. N. The Vapor Pressure of Copper. *Journal of the American Chemical Society* **75,** 1529–1531 (1953).

236. Hersh, H. N. The Vapor Pressure of Copper - Correction. *Journal of the American Chemical Society* **75,** 6361–6361 (1953).

237. Cochran, C. N. & Foster, L. M. Vapor Pressure of Gallium, Stability of Gallium Suboxide Vapor, and Equilibria of Some Reactions Producing Gallium Suboxide Vapor. *Journal of The Electrochemical Society* **109,** 144–148 (1962).

Acknowledgements

I wish to express my thanks and appreciation to those who helped me throughout the years in carrying out the research work in preparing this thesis. I am very grateful especially to:

Prof. Dr. Heinz Kalt, my doctoral supervisor, who accepted me as a Ph.D. student at the Institute for Applied Physics at the Karlsruhe Institute of Technology. His careful coaching throughout this period was highly beneficial to me.

Prof. Dr. Thomas Schimmel for the willingness to evaluate this thesis as co-referee.

Dr. Daniel Schaadt, for giving me the opportunity to be part of his research team and for his competent guidance throughout the whole duration of my Ph.D. thesis. He enabled my participation on several national and international topical conferences as well as visits to our fellow scientific collaborators in Taiwan. He was considerably helpful in providing me with essential information contributing to the successful completion of my work.

Heinrich Reimer for his exceptional technical dedication and assistance in building up and maintaining the MBE machine.

Philipp Ganz for fruitful discussions on the growth of nitrides and for the great teamwork on the XANES and XLD measurements of Cu-doped GaN.

Dr. Yen-Liang Chen for many discussions on the growth of nitrides, helping growing nitrides, in preparing the TEM samples by FIB, his enormous help in countless issues during my visits to Taiwan.

Yu-Chi Hsu for a grand collaboration on the growth of non-polar GaN on LAO and creating a pleasant atmosphere for my stay in Taiwan.

Marius Bürkle for the great assistance and many discussions on the x-ray absorption calculations of Cu-doped GaN.

Matthieu Helfrich and Dr. Dongzhi Hu for numerous discussions as well as for the terrific teamwork within our group.

All former and present members of Dr. Schaadt's MBE group. Especially, I would like to mention Mareike Trunk and Raimund Vöhringer.

Prof. Dr. Ikai Lo for facilitating my stay in his group and for letting me use the laboratory in Taiwan to my benefit.

Prof. Dr. Liuwen Chang for very helpful advice and discussions on the TEM experiments. Paul Vincze for AFM measurements of *A*-plane GaN grown on (010) LGO.

Teng-Hsing Huang, Dr. Yen-Liang Chen and Dr. Cheng-Hung Shih for the accurate preparation of TEM samples and for taking TEM images of the GaN samples grown on LGO.

Jacques Hawecker for patiently carrying out countless SEM investigations on nonpolar GaN samples.

The members of Prof. Dr. H. Kalt's group for their considerable helpfulness in the laboratories and the friendly way of meeting any concerns.

All Ph.D. students and members of the Department of Physics and the Department of Materials Science and Opto-electronic Engineering of the National Sun Yat-Sen University in Taiwan for their wonderful hospitality in making my stay there a pleasant one.

The Karlsruhe House of Young Scientists (KHYS) for financing the scientific exchange with the Physics Department and the Department of Materials Science and Opto-electronic Engineering of the Sun Yat-Sen University in Kaohsiung, Taiwan.

To Dr. Fabrice Wilhelm and Dr. Andre Rogalev for their kind support at the European Synchrotron Radiation Facility (ESRF) in Grenoble.

My family for taking weight off my shoulders whenever needed and supporting me lovingly throughout all stages of my life leading to the completion of this thesis.